GRAIN BOUNDARY PROCESSES, ANELASTICITY, AND TEST OF THE EFFECTIVE STRESS LAW FOR SEMIBRITTLE DEFORMATION OF SYNTHETIC SALT-ROCKS

A Dissertation

by

JIHUI DING

Submitted to the Office of Graduate and Professional Studies of
Texas A&M University
in partial fulfillment of the requirements for the degree of

DOCTOR OF PHILOSOPHY

Chair of Committee,	Frederick M. Chester
Co-Chair of Committee,	Judith S. Chester
Committee Members,	Andreas Kronenberg
	Marcelo Sánchez
Head of Department,	Michael Pope

May 2019

Major Subject: Geology

ABSTRACT

In many natural and engineered systems, rock deforms by semibrittle flow that involves the coupled interaction of brittle and intracrystalline plastic micromechanisms. Synthetic salt-rock samples were prepared and deformed in the laboratory to investigate elastic and inelastic behavior, and to test the effective stress law during deformation in the semibrittle regime. The synthetic salt-rocks were fabricated by uniaxial consolidation of granular salt to produce two end-member types, an annealed, recrystallized, low-porosity, dry salt-rock, and a hardened, granular, porous, wet salt-rock. Triaxial cyclic deformation and stress-relaxation at a confining pressure of 1 MPa, room temperature, and strain rates of 3×10^{-5} to 10^{-9} s^{-1} show that deformation occurs by intragranular cracking, grain boundary sliding and opening, and dislocation glide. Grain boundary opening develops preferentially in the loading direction, and increases in aperture and linkage with increasing inelastic deformation. Grain boundary sliding is predominantly a frictional process at high strain rates, but occurs by diffusion at low strain rates in wet samples. Activation of grain boundary sliding during semibrittle flow changes the elastic behavior by reducing the elastic modulus, increasing hysteresis, and increasing anelasticity at low differential loads, particularly in wet samples. The effective stress relationship was explored through isostatic consolidation and triaxial compression tests using argon and silicone oil as pore fluids, by varying pore fluid pressure while holding differential pressure constant. In all experiments, behavior was independent of the absolute value of pore fluid pressure, i.e., the effective stress coefficient, α, is one or

nearly one. Analysis of grain contact area for both sliding boundaries and boundaries in contact by intracrystalline plastic yielding indicates that α is independent of the true area of grain contact.

DEDICATION

I dedicate my dissertation to my parents, my wife Junhua, and our angels. Their love and support motivate me to live every day in a meaningful way.

ACKNOWLEDGEMENTS

I would like to thank my committee co-chairs, Dr. Frederick Chester and Dr. Judith Chester for their support and guidance during my PhD studies. I learned so many things from them that I believe will benefit me in the rest of my life. I am also very grateful to my committee members, Dr. Andreas Kronenberg and Dr. Marcelo Sánchez, for their suggestions and comments on my research work. Special thanks go to Dr. Andreas Kronenberg for his generous help on my career. Thanks also go to Dr. Ayers Walter for his help on my preliminary exam and research proposal.

I would like to thank Dr. Chloé Arson and her PhD students Cheng Zhu and Xianda Shen for many insightful discussions. I enjoyed collaboration with them and made friends with them.

I would like to thank my friends and colleagues in the Center for Tectonophysics and faculty and staff of the Department and Geology and Geophysics. They made my stay at Texas A&M University an enjoyable experience. Special thanks go to Szu-Ting Kuo, Dunyu Liu, Bin Luo, Guangjian Xu, Leiyin Jiao, Omid Saber, Ahmet Unal, Daniel Elizondo, Charles Choens, Monica Barbery, Dawid Szafranski, and Dana Gallegos for their friendship. I would like to also thank Dr. Hiroko Kitajima for her generous help in my lab work.

I am also very grateful to Chris Spiers, Peter van Krieken, Piercarlo Giacomel, and others at Utrecht University for inviting me to their HPT lab and sharing their salt

sectioning, etching, and microscopy techniques, and to Chris Spiers, Colin Peach, and Jianye Chen for discussions of salt deformation.

CONTRIBUTORS AND FUNDING SOURCES

Contributors

This work was supervised by a dissertation committee consisting of Professor Frederick Chester, Professor Judith Chester, and Professor Andreas Kronenberg of the Department of Geology and Geophysics and Professor Marcelo Sánchez of the Department of Civil Engineering.

Some of the consolidation experiments in Chapter 2 were conducted by Thu Nguyen, an undergraduate student at Texas A&M University.

The water content of synthetic salt-rock samples was measured with the assistance of Professor Andreas Kronenberg.

All other work conducted for the dissertation was completed by the student independently.

Funding Sources

Graduate study was supported by teaching assistantships from the Department of Geology and Geophysics of Texas A&M University.

This work was also made possible in part by National Science Foundation under Grant Number CMMI-1361996 (TAMU) and CMMI-1362004 (GT). Its contents are solely the responsibility of the authors and do not necessarily represent the official views of the National Science Foundation.

TABLE OF CONTENTS

Page

LIST OF FIGURES

Page

LIST OF TABLES

Page

1. INTRODUCTION

Identifying the fundamental deformation mechanisms of rock under different geologic conditions is critical to defining the partitioning of strain by brittle and crystal-plastic mechanisms, and to developing appropriate hydro-thermo-mechanical models of geologic processes, such as creep and failure of engineered caverns for waste isolation, earthquake rupture and after-slip, and diapirism and melt migration.

Often multiple micromechanisms operate simultaneously to contribute to total rock deformation, as is the case for semibrittle deformation that involves both brittle and viscous microprocesses. In this case, it is important to determine each individual micromechanism and the interaction between them at different deformation conditions. Study of salt-rock deformation can elucidate the interplay between these mechanisms easily in the laboratory as nearly all micromechanisms can be activated. Characterizing deformation processes in salt-rock not only benefits the design and optimization of salt-rock storage facilities, but also provides important insights to the deformation of other rock-forming materials.

In Sections 2, 3, and 4 of this dissertation, I present three suites of experimental studies that examine microcrack development, grain boundary processes, anelasticity, and effective stress controlling flow strength and volumetric strain in semibrittle synthetic salt-rocks.

Section 2 focuses on the consolidation behavior of granular salt to produce synthetic salt-rocks, and triaxial deformation of the synthetic salt-rock samples to

investigate microcrack network development. Consolidation of granular salt is studied through uniaxial consolidation experiments on reagent-grade and sea salt of varying grain size, at different temperatures and load paths. Microstructures are studied using reflected- and transmitted-light to characterize grain-scale structures for the different consolidation conditions. Knowledge gained from consolidation experiments is used to fabricate synthetic salt-rock samples for subsequent studies. To understand spalling mechanisms in salt caverns, cyclic triaxial compression tests are performed to reveal characteristics of grain boundary microcracking in the synthetic salt-rocks.

Section 3 focuses on the characteristics of elastic and inelastic deformation under semibrittle conditions. These tests were conducted on the consolidated salt-rock samples and on annealed consolidated-salt-rock samples, both produced from reagent-grade granular salt. Elastic properties were determined by stress cycling at increasing inelastic strain and correlated with microstructures. Stress relaxation experiments are used to define the deformation mechanisms. Mechanical and microstructural data are analyzed to interpret the interplay of elastic and inelastic deformation and associated micromechanisms.

Section 4 examines the effective stress relationships controlling flow strength and volumetric strain in synthetic salt-rocks. Triaxial compression tests with confining and pore pressure cycling are conducted to amplify the change of effective stress states for the case that effective stress coefficient deviates from one. Isostatic consolidation tests are performed at the same nominal effective pressures (i.e., effective stress coefficient equals one) but under varying pore pressures to investigate the effects of pore

pressure on effective stress. Combining with microstructural observation, the effective stress coefficient, and its dependence on true area of grain contact are discussed.

2. CONSOLIDATION OF GRANULAR SALT AND MICROCRACK NETWORK DEVELOPMENT IN SYNTHETIC SALT-ROCK DURING CYCLIC LOADING AT LOW CONFINING PRESSURE[*]

2.1. Introduction

The rheological properties of salt-rock have been an important research focus because salt-rocks are studied as an analog to other geomaterials in that various deformation mechanisms, including cracking, frictional sliding, pressure solution, crystal plasticity, and dynamic recrystallization are easily activated at laboratory conditions (Zhang et al., 2007). Salt-rock also is also considered a viable geomaterial for engineered repositories of waste and energy resources, such as radioactive waste, oil, and gas (Carter et al., 1993; Urai, Spiers, et al., 1986).

Extensive experimental work has been done on salt-rock to determine constitutive relationships and guide numerical modeling (e.g., Watanabe & Peach, 2002; Ter Heege et al., 2005; Zhu & Arson, 2015a). Both natural and synthetic salt-rocks have been used for experimental investigations; artificially prepared salt-rock is of higher purity and can be fabricated in a way that best serves parametric studies (e.g., Carter & Hansen, 1983; Schenk & Urai, 2003; Bourcier et al., 2013). Consolidation of granular

---

[*] Reprinted with permission from Ding, J., Chester, F. M., Chester, J. S., Zhu, C., & Arson, C. (2016). *Mechanical behavior and microstructure development in consolidation of nominally dry granular salt.* Paper presented at 50th U.S. Rock Mechanics/Geomechanics Symposium, Houston, TX. Copyright 2016 by American Rock Mechanics Association. And Ding, J., Chester, F. M., Chester, J. S., Shen, X., & Arson, C. (2017). *Microcrack network development in salt-rock during cyclic loading at low confining pressure.* Paper presented at 51st U.S. Rock Mechanics/Geomechanics Symposium, San Francisco, CA. Copyright 2017 by American Rock Mechanics Association.

salt is a common method used to produce synthetic salt-rock samples; however, salt is highly sensitive to moisture so it is critical to have a good control of the humidity of the environment in which salt samples are produced, stored, and processed. Maintaining a consistently dry environment during all stages of handling salt samples can be challenging.

Because of its favorable creep characteristics and ultra-low permeability for sealing, salt-rock is a viable geomaterial for hydrocarbon storage and waste disposal. In the case of storing high-pressure natural gas for balancing seasonal supply, or for pressurized gas associated with wind energy storage, salt caverns are subjected to long-term cyclic loading such that cavern stability becomes a major concern (e.g., Brouard, 2012; Minkley et al., 2015). A common stability issue is spalling at salt cavern wall, which not only alters the cavern geometry but also damages the hanging string and causes roof collapse. Salt block fall due to spalling has been reported in numerous salt caverns, for example the Kiel salt cavern of Germany (Baar, 1977) and the Big Hill cavern of USA (Munson et al., 2004). Damage development in salt-rock has been studied through field tests (e.g., Cole, 2002; Rokahr et al., 2007), laboratory experiments (e.g., Peach & Spiers, 1996) and numerical simulations (e.g., Sobolik & Lord, 2015; Zhu & Arson, 2015b). These studies have provided insights into spalling phenomenon from different perspectives. However, direct observation of fracture initiation and evolution is lacking, and there is a need for additional experimental work to elucidate the mechanisms leading to damage and cavern failure.

We developed an experimental procedure that allows preparation of nominally dry synthetic salt-rock via uniaxial consolidation and subsequent characterization of the microstructure of the salt-rock, using a well-controlled low-humidity chamber. In this section, we document the consolidation conditions used to create synthetic salt-rock samples with different porosities, and document the mechanical behavior and deformation mechanisms during consolidation. In addition, we illustrate the reproducibility in sample production. Knowledge gained from this work will be used to fabricate suitable samples for deformation experiments and guide numerical modeling of granular salt consolidation.

Additionally, to better understand the mechanisms of microcrack development in semibrittle polycrystalline aggregates, such as those in salt cavern walls, we conducted cyclic triaxial compression tests on synthetic salt-rocks at room temperature and 1 MPa confining pressure. Samples from different stages of cyclic loading were used to prepare thin sections for microstructure characterization. Direct observations of crack damage accumulation were analyzed, and the observed damage mechanisms may provide insights to mechanisms associated with spalling in salt caverns. Knowledge gained from these experiments could be useful to guide numerical modeling of damage development and help design and optimize salt-rock storage facilities.

2.2. Methods

2.2.1. Test Material

Two types of granular salt are used in uniaxial consolidation experiments, sea salt and reagent-grade salt. The sea salt was purchased from SaltWorks®; it does not

contain anti-caking or free-flowing additives or conditioners. The main benefit of using sea salt is that it comes in a variety of grain sizes, in contrast to the limited grain-size range of the reagent-grade salt. Before consolidation, the granular salt is sieved in a controlled low-humidity environment (RH < 17%) to produce more uniform grain size distributions (Table 2.1). The starting water content is determined from the mass of the salt before and after heating in an oven to 500 ℃ for 2-3 hours. Heating to this temperature promotes thermal cracking which allows the release of fluid trapped in fluid inclusions. The difference in mass before and after heating is taken as a measure of the total water content.

Table 2.1 As-received condition of granular salt used herein.

Salt Type	Purity (NaCl wt%)	Grain Size (mm)	Water Content (wt%)
Reagent-grade salt	99	0.3-0.355	0.43
Sea salt	96	1-1.2	0.38
Sea salt	96	1.7-2	0.38

The synthetic salt-rock samples used in cyclic triaxial compression tests were fabricated through uniaxial consolidation of reagent-grade granular salt at the following conditions: a temperature of 150 °C, a maximum axial stress of 75 MPa, and a displacement rate of 0.034 mm/s. Bulk porosity of the synthetic salt-rock sample produced from the above conditions is around 5.45±0.06%. The sample was kept dry throughout all stages of this study

2.2.2. Consolidation Setup

A uniaxial consolidation system was developed to achieve consolidation at temperatures up to 230 ℃ and displacement rates up to 0.047 mm/s (Figure 2.1). In this system, an alumina plate is placed between the stationary plate and bottom plate to minimize heat dissipation through the loading frame. A cylindrical die with a 19 mm (0.75 inch) diameter hole sits on the lower piston of the bottom plate, which contains a port for evacuation. To facilitate air flow during evacuation, a perforated stainless steel spacer is placed on top of lower piston. Both upper and lower pistons are equipped with o-ring seals to maintain a vacuum during consolidation. Two bevel rings are placed on the two ends of the granular salt stack to ensure that the ends of the consolidated sample are square. Resistance wire heating strips are wrapped around the cylindrical die and controlled to increase and maintain elevated temperatures. A K-type thermocouple is inserted into a small-diameter blind hole in the die to measure temperature close to the salt sample. Loading and unloading are achieved either with a hydraulic cylinder placed between the stationary plate and alumina plate while the movable plate is fixed, or with an electric motor and gear-driven ball-screw that displace the movable plate at a constant speed. Axial force and displacement are measured via a load cell and LVDT, respectively. The double-ended moveable-piston loading configuration helps to reduce stress gradients during consolidation.

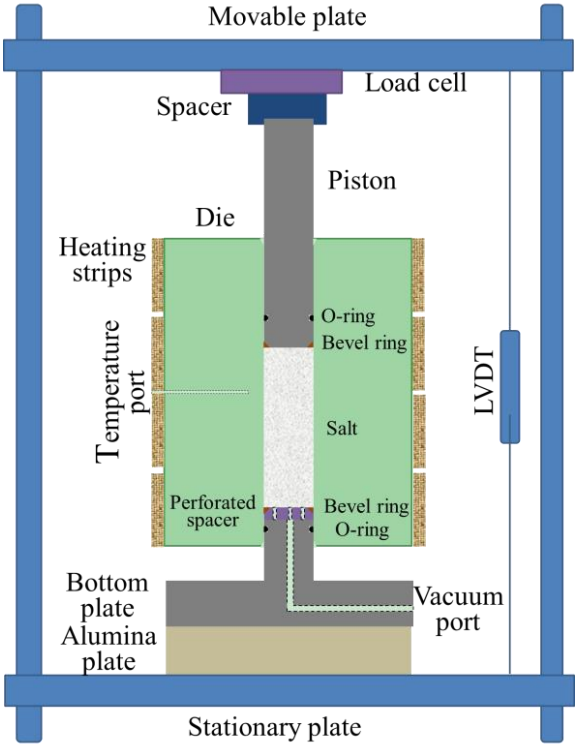

Figure 2.1 Schematic diagram of the consolidation system (Ding et al., 2016).

A controlled low-humidity environment is established by flowing dry compressed air through a glove-box (Figure 2.2). Relative humidity as low as 10% can easily be achieved and maintained. Granular salt and synthetic salt-rock samples are handled at all stages of preparation for the experiments and microscopy in this low-humidity environment to keep the samples nominally dry.

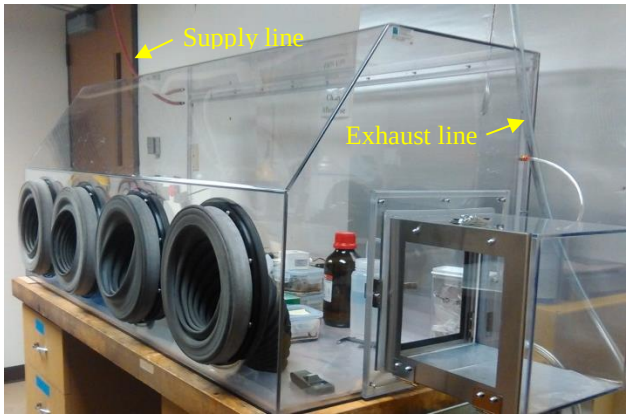

Figure 2.2 Photograph of controlled low-humidity environment achieved by flowing dry compressed air through a glove-box. Flow rate is adjustable through a regulator (not in photo) to maintain relative humidity < 17% (Ding et al., 2016).

2.2.3. Consolidation Procedures

Uniaxial consolidation experiments are conducted for a range of conditions by adjusting grain size, temperature, load path, and maximum axial stress. First, the inner wall of consolidation die, end surfaces of the pistons, and bottom plate are uniformly sprayed with graphite film to reduce friction along the inner wall of the cylinder. Then heating strips are installed and temperature is increased to the target value. Granular salt is then poured into the die followed by inserting the upper piston. Once the stack is sealed, the system is evacuated. Two distinct load paths are employed: 1) A "creep-test" load path (LP1) is simulated using the hydraulic cylinder to raise axial load to the target value in less than 2 minutes, and then maintaining the load for 10 minutes; 2) A constant rate load path (LP2) is achieved using the electric motor/ball-screw system to drive the movable plate down at a constant displacement rate of 0.034 mm/s, corresponding to a strain rate of $\sim 5\times10^{-4}$ s^{-1}. Once the target stress is achieved, the motor is immediately reversed to begin unloading. For both load paths, the vacuum is

monitored and maintained during consolidation. For LP2, granular salt is dried in-situ by maintaining an elevated temperature for 1-2 hours, during which the vacuum is re-established about every 15 minutes to remove additional water vapor released during heating. This step reduces water content in the salt by about half, yielding samples with ~0.22 wt% water for sea salt, and ~0.27 wt% water for reagent-grade salt. After unloading, the consolidation stack is cooled by two electric fans while maintaining the vacuum in the salt sample chamber. Upon reaching room temperature, the entire consolidation assembly is transferred to the controlled low-humidity environment, where the pistons are removed and the salt sample is easily released due to the different thermal expansion coefficients of salt and steel (Peach & Spiers, 1996). Consolidated salt sample dimensions and weight are measured to determine the final porosity.

2.2.4. Cyclic Triaxial Compression Experiments

The cylindrical, synthetic salt-rock samples produced through uniaxial consolidation were jacketed with heat-shrinkable polyolefin jackets and sealed with tie wires at piston or spacer grooves (Figure 2.3). Very thin (0.002”) Teflon sheets were placed at two sample ends to reduce friction with piston and spacer. This promotes more uniform deformation along the axis of the sample and therefore reduces sample barreling. Differential load is measured through an internal force gauge and is unaffected by friction between loading piston and sealing stack. Change of sample length by deformation is measured through an external DCDT. Correction of rig distortion is applied to determine axial strain of sample at constant confining pressures. Cyclic triaxial compression tests were conducted at a confining pressure of 1 MPa, a strain rate

of 3×10^{-6} s^{-1}, and at room temperature. A total of eight unloading-reloading cycles were employed, in addition to initial loading and final unloading. One unloading-reloading cycle was applied in the elastic deformation regime, while the rest load cycles were fulfilled after plastic yielding.

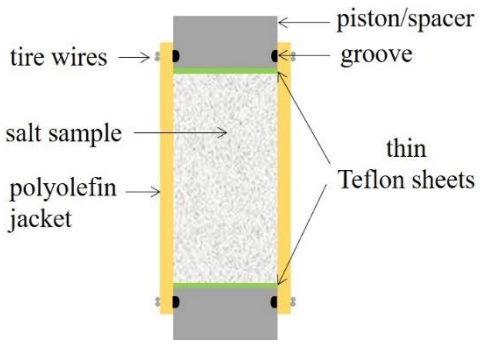

Figure 2.3 Schematic of sample instrumentation for cyclic triaxial compression tests.

2.2.5. Microstructural Characterization

For microscopic study, the starting material and key consolidated samples are epoxy-saturated, cut, and polished to make petrographic sections, and then chemically etched to allow observation of grain-scale features, including grain boundaries and dislocations. The sectioning and etching procedures follow the techniques developed by Spiers et al. (1986) with minor modifications. During this entire process, the consolidated salt samples remain in the controlled low-humidity environment. Both reflected- and transmitted-light are used to characterize grain-scale microstructures.

Using repeat experiments, synthetic salt-rock samples before, during, and at the end of cyclic loading were extracted for microstructure observation. Thin section images

were taken from the center portion of the sample using 20× magnification, and stitched together to allow observation of more than 100 grains. On the stitched image, salt grain boundaries were traced and opening-mode microcracks were interpreted based on the following two criteria:

1. There is clear separation between two salt grain boundaries;
2. The opposing sides of these two salt grain boundaries match well geometrically, which indicates they were previously in contact.

2.3. Results

2.3.1. Uniaxial Consolidation Experiments

2.3.1.1. Mechanical Behavior

The void ratio evolution as a function of axial stress during consolidation is determined from measurements of sample dimensions and weight, axial displacement, and axial force. Sea salt experiments for different grain size ranges deformed at different temperatures and the two load paths show that final void ratio is related to peak stress and a strong dependence on temperature (Figure 2.4). Starting void ratios before consolidation are generally similar, ranging from 0.76 to 0.81; the range likely reflects slight differences in initial packing. With an increase in peak stress, void ratio decreases approximately linearly with log stress, except at void ratios less than ~0.05. Temperature dependence of compaction is very apparent, as higher temperatures result in lower void ratios at the same stress level. Grain size and load path have little influence on the final void ratio.

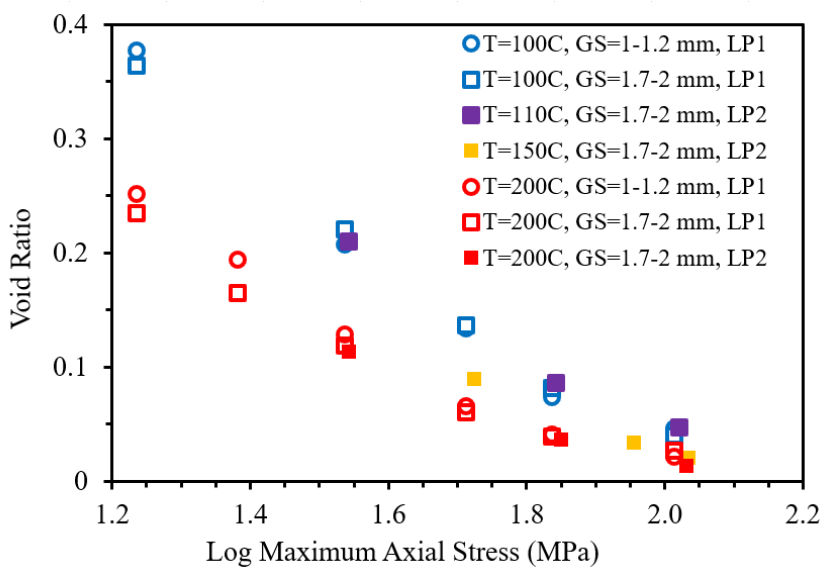

Figure 2.4 Void ratio versus the logarithm of maximum axial stress for granular sea salt consolidated at different temperatures (T), grain sizes (GS), and load paths (LP) (Ding et al., 2016).

The complete consolidation curves for sea salt deformed under LP2 at three different temperatures (Figure 2.5) are consistent with the final void ratio results shown in Figure 2.4. The data show that at intermediate stress levels, void ratio is linearly related to logarithmic stress, except at very low and very high stress levels.

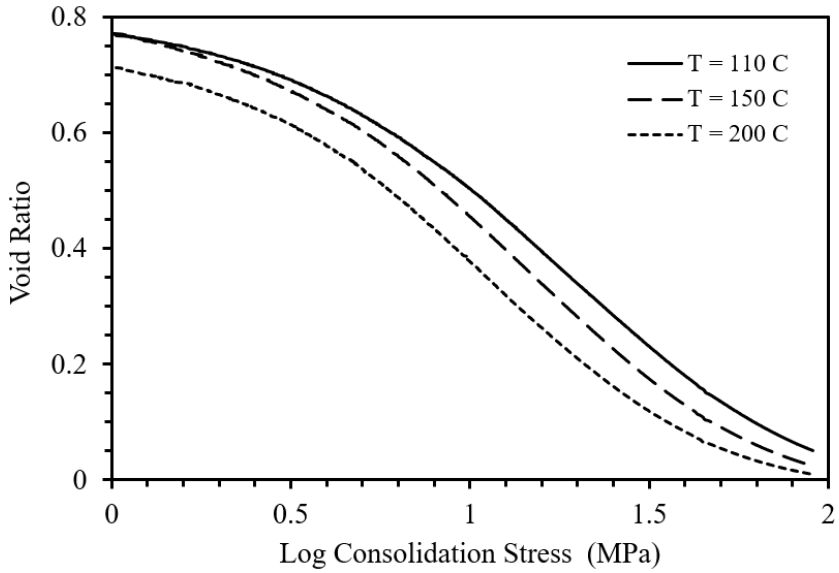

Figure 2.5 Void ratio versus the logarithm of consolidation stress for granular sea salt (grain size 1.7-2 mm) consolidated at temperatures of 110 ℃, 150 ℃ and 200 ℃ with LP2 (Ding et al., 2016).

Two synthetic salt-rock samples fabricated at the same conditions: i.e., grain size between 1.7-2 mm, a maximum axial stress of 69 MPa, a temperature of 200 ℃, and LP1 load path, were deformed in cyclic triaxial compression tests to check reproducibility of mechanical behavior. Cyclic loading is applied in both elastic and plastic deformation regimes at a confining pressure of 4 MPa, a strain rate of 1.4×10^{-4} s^{-1}, and room temperature. Comparison of the two experiments shows excellent reproducibility in mechanical response (Figure 2.6). As these two samples were consolidated at the same conditions, we interpret that the reproducibility reflects similar porosity and microstructure produced during the consolidation stage.

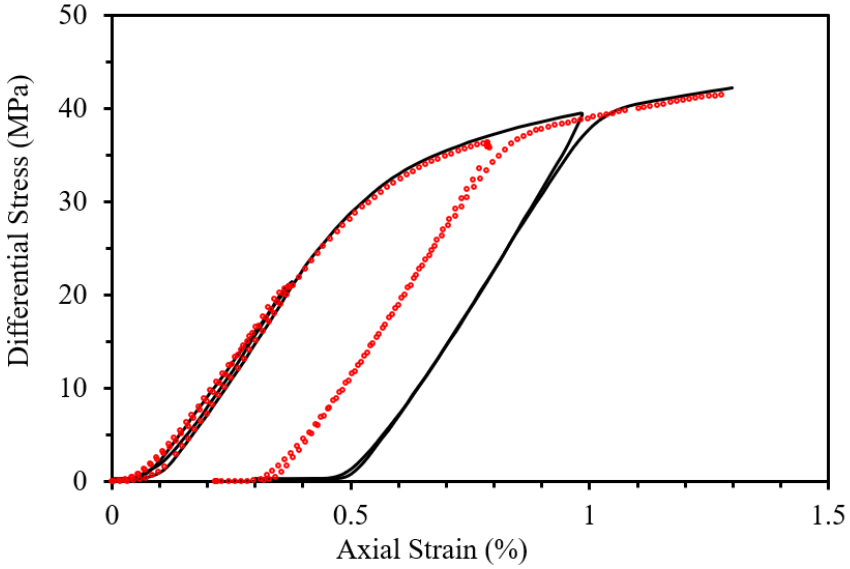

Figure 2.6 Stress-strain curves of triaxial compression tests (confining pressure 4 MPa, strain rate 1.4×10^{-4} s^{-1} , room temperature) on two synthetic salt-rock samples consolidated with LP1 to a final porosity of ~4% at the same conditions (grain size 1.7-2 mm, maximum axial stress 69 MPa, temperature 200 ℃). Cyclic loading is applied in both elastic and plastic deformation regimes (Ding et al., 2016).

2.3.1.2. Microstructural Observation

Although the sea salt used in this study is of high purity and free of additives, fluid inclusions are abundant and have different sizes (Figure 2.7a, b). It is common to observe fluid inclusions arranged in planar arrays, suggesting they are healed cleavage cracks. Most fluid inclusions are cubic in shape with a visible gas bubble, indicating the presence of brine (Van den Kerkhof & Hein, 2001). There are also tube-shaped fluid inclusions which are often larger in size. As fluid inclusions intersect with the polished surface of the petrographic section, under reflected light they appear as cubic or tube-shaped pits.

Synthetic rock salt samples consolidated using LP2 at 150 ℃ and maximum axial stresses of 53 and 90 MPa show very few intragranular cracks, indicating limited influence of brittle deformation during consolidation (Figure 2.8a, b). Etched surface structures demonstrate inhomogeneous strain accumulation as evidenced by high dislocation density near grain contacts and relatively dislocation-free areas close to pores. Fluid inclusions manifest themselves in the form of dark pits and are often the sites of high concentration of dislocations, slip lines and subgrains. Static recrystallized grains, absent in the starting material, appear in some of the most highly strained areas of the consolidated samples. These recrystallized grains, characterized by straight boundaries and dislocation-feature-free interiors, grew by grain boundary migration at expense of highly deformed grains.

At the lower maximum axial stress (53 MPa), the sample has a higher porosity and larger pores (Figure 2.8a). Grains adjacent to pores exhibit fewer or no apparent dislocations. In contrast, stressed grain contacts are characterized by dense dislocation structures. At higher stress (90 MPa), the sample is more compacted, and has a lower porosity and a greater dislocation density overall (Figure 2.8b). Both samples, however, display a heterogeneous distribution of dislocations because of the variable size and orientation of grain contacts, and variable internal grain structure (e.g., number and locations of fluid inclusions).

Although the reagent-grade salt is much smaller in grain size, the microstructures of the consolidated reagent-grade samples are similar to those noted in sea salt samples. The reagent-grade starting material is free of dislocations, but also contains fluid

inclusions (Figure 2.9a). Consolidation produces regions of high dislocation density, and recrystallized grains are also observed in some highly strained areas (Figure 2.9b).

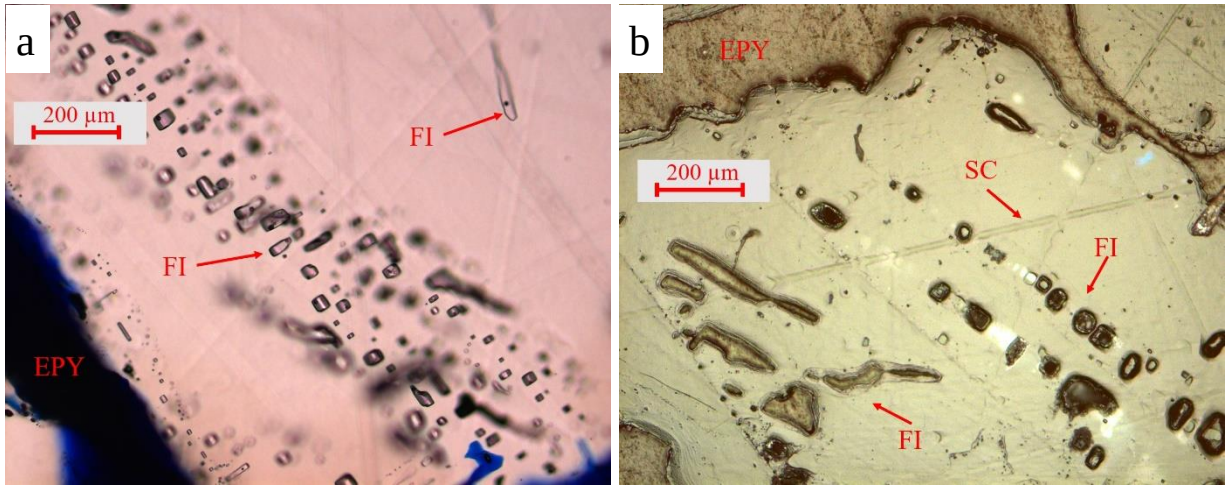

Figure 2.7 (a) Transmitted-light micrograph of sea salt starting material. Translucent areas are salt grains, blue and dark blue areas are pores filled with epoxy. FI indicates fluid inclusions intersected the polished surface. Planar arrangement of fluid inclusions is clearly visible. In the upper right, arrow points to a tube-like fluid inclusion containing a small gas bubble (black dot). (b) Reflected-light micrograph of sea salt starting material. Surface is etched. Salt grains are free of dislocation structure. Cubic and tube-like pits are the result of fluid inclusions intersecting polishing surface. SC indicates scratch resulted from polishing (Ding et al., 2016).

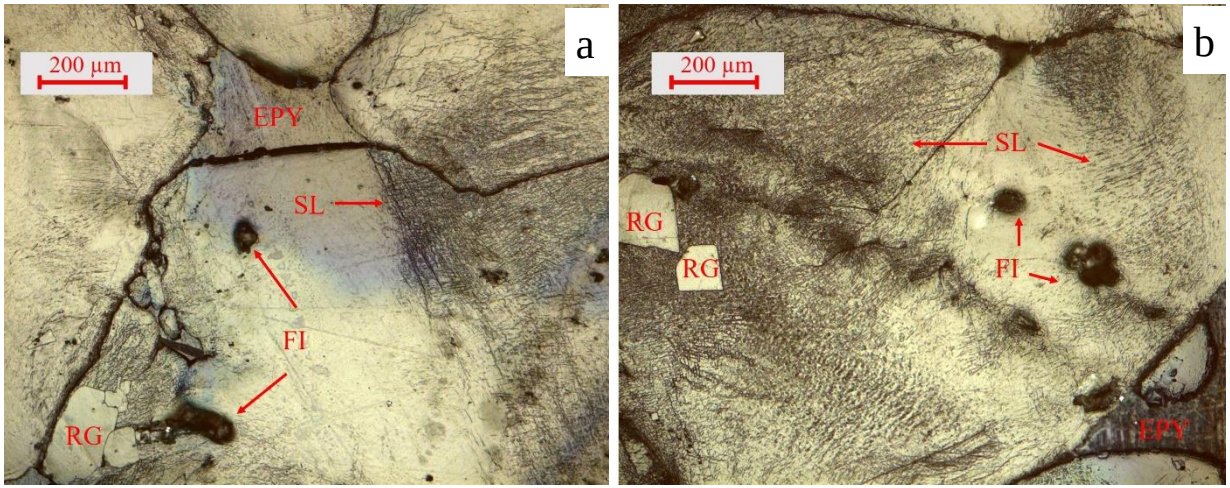

Figure 2.8 Reflected-light micrographs of (a) sea salt sample consolidated at 150 ℃ and 53 MPa maximum axial stress, (b) sea salt sample consolidated at 150 ℃ and 90 MPa maximum axial stress. Surface is etched. Slip lines developed in areas of high strain accumulation. Two recrystallized grains (RG) have straight boundaries and are free of dislocations as shown in (b). Sections are cut parallel to the axial compression direction (vertical). EPY – epoxy (pore), FI – fluid inclusions intersected the polished surface, SL – slip lines (Ding et al., 2016).

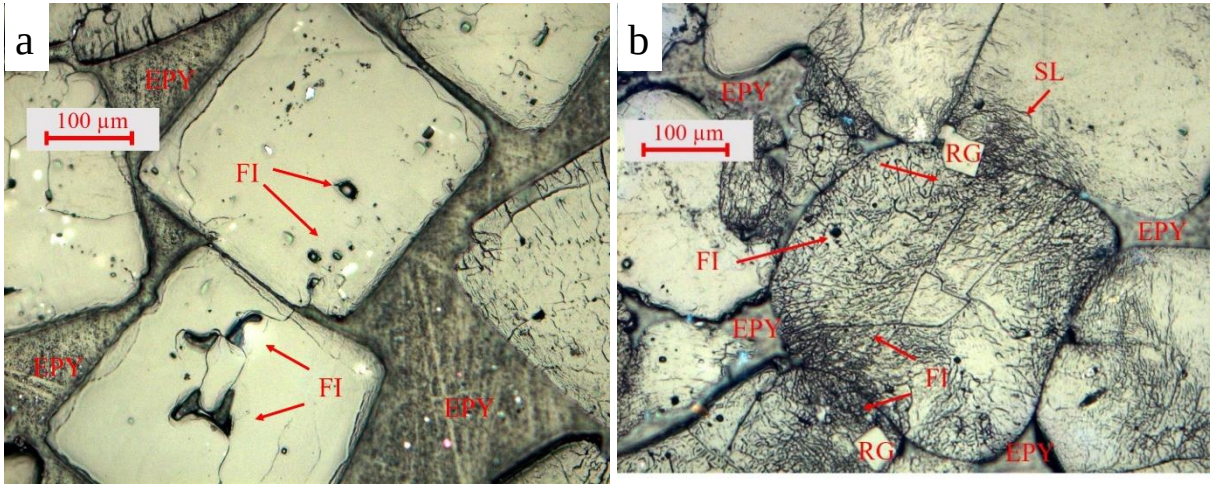

Figure 2.9 Reflected-light micrographs of (a) reagent-grade salt starting material, (b) reagent-grade salt sample consolidated at 150 ℃ and 53 MPa maximum axial stress. Salt grains in (a) are free of dislocations. Dislocation structure in (b) shows areas of high strain accumulation. Recrystallized grains (RG) develop in highly strained area. Sections are cut parallel to the axial compression direction (vertical). EPY – epoxy (pore), FI – fluid inclusions intersected the polished surface, SL – slip lines (Ding et al., 2016).

2.3.2. Cyclic Triaxial Compression Experiments

2.3.2.1. Mechanical Behavior

At room temperature and 1 MPa confining pressure, synthetic salt-rock exhibits ductile behavior (Figure 2.10). The first unloading-reloading cycle nearly fully overly the initial loading curve, which indicates dominant elastic behavior. After yielding, the sample deforms plastically with slight work hardening. Each unloading is applied to zero differential stress; subsequent reloading does not produce significant hysteresis.

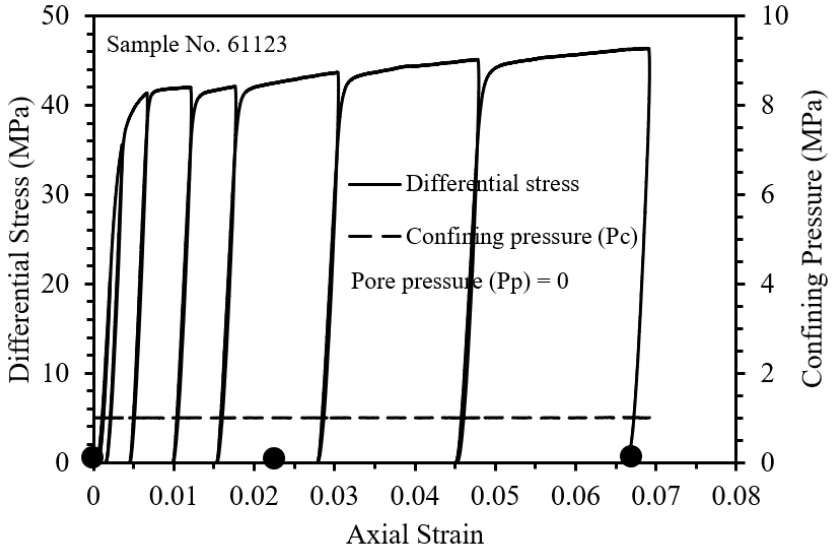

Figure 2.10 Differential stress versus axial strain of cyclic triaxial compression test at a confining pressure of 1 MPa, a strain rate of 3×10^{-6} s^{-1}, and room temperature. Solid circles show where samples are made into thin sections.

2.3.2.2. Microstructural Observation

The synthetic salt-rock produced from uniaxial consolidation at elevated temperature shows minor intragranular microcracking (Figure 2.11a). Almost all of these

intragranular microcracks are associated with fluid inclusions present in salt grains. These fluid inclusions act as stress concentrators and promote microcracking. There is no evidence for separation at grain contacts as all of them are tight, which results from crystal-plastic deformation of salt grains (e.g., Figure 2.8a, b and 2.9b). After cyclic triaxial loading to an total axial strain of 2.27%, grain boundary cracking becomes the dominant brittle deformation mechanism (Figure 2.11b). These microcracks exhibit a preferred orientation that is sub-parallel to the axial loading direction. With further cyclic loading, dilatant grain boundary microcracks increase in density as well as in separation, as documented at a total axial strain of 6.76% (Figure 2.11c). These grain boundary microcracks also display a clear tendency to link with neighboring cracks in the axial direction.

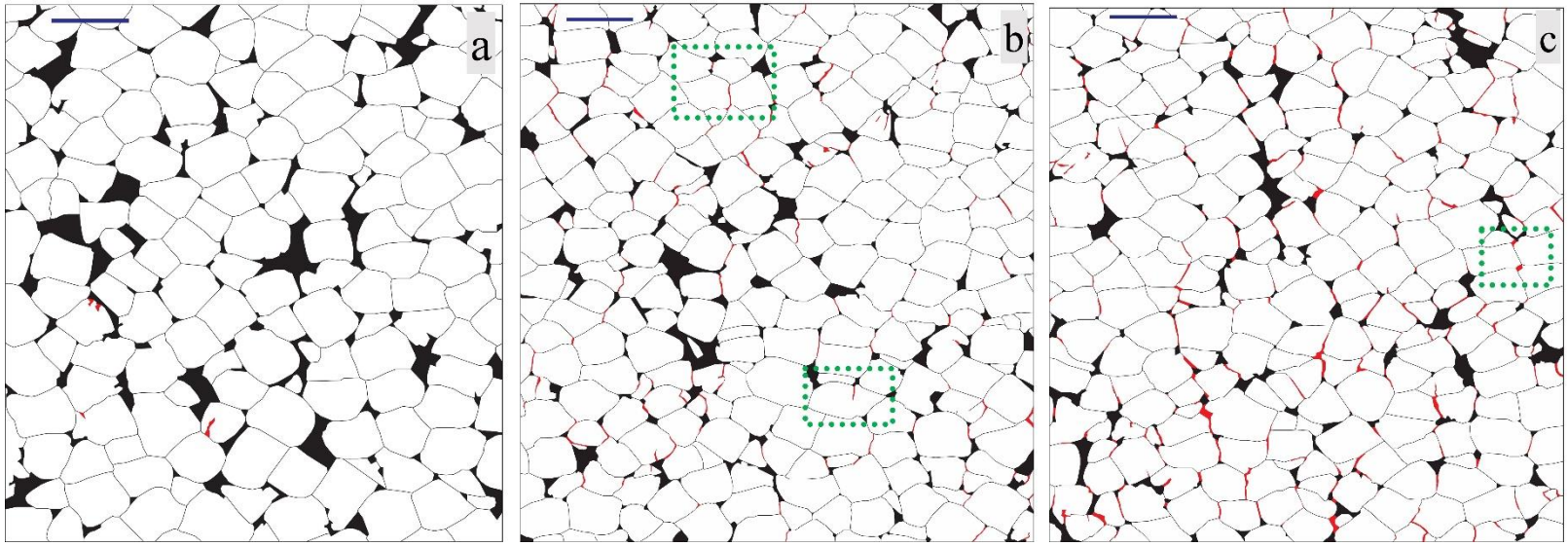

Figure 2.11 Line tracings of micrographs of salt grains (white), pores (black) and opening-mode microcracks (red) of synthetic salt-rock with (a) total axial strain = 0; (b) total axial strain = 2.27%; (c) total axial strain = 6.76%; axial stress is vertical, dark blue scale bar represents 0.5 mm; images are taken at sample center; note all grain contacts are tight when axial strain is zero; dashed squares show locations corresponding to crack geometries shown in Figure 2.12 (Ding et al., 2017).

2.4. Discussion

2.4.1. Consolidation Mechanisms

Depending on applied stress, strain rate, temperature, duration, and water content, consolidation of granular material often involves grain rotation, sliding, and crushing. For salt, crystal plasticity, dissolution-precipitation, and dynamic recrystallization are also important mechanisms (Hwang et al., 1993). Microstructural observations of salt consolidation suggest crystal plasticity dominants the deformation process, as evidenced by the high-density of dislocations and small number of recrystallized grains. There is some evidence of intragranular and grain boundary fractures in samples consolidated at 150 ℃, but overall brittle deformation is minor. As to the formation of the recrystallized grains observed in this study, we infer that they grow during the 2-3 hour period after the consolidation test, while the consolidation cell is cooled, because the recrystallized grains exhibit relatively strain-free interiors and cubic shapes.

2.4.2. Grain boundary Cracking in Cyclic Triaxial Compression Experiments

In the cyclic triaxial compression tests, grain boundary microcracking is the dominant brittle deformation mechanism and leads to pronounced dilation. The grain boundary microcracking is influenced by loading configuration and geometric relationships between neighboring grains. Brace et al. (1966) discussed three basic modes of microcracking that are all observed in the microstructure of our deformed synthetic salt-rocks. The isolated axial cracks occur mostly within salt grains that form in association with preexisting fluid inclusions (Figure 2.12a). This type of microcrack is

rare as fluid inclusions in the sample are few. At grain triple-junctions, the vertical grain contact (parallel to the load axis) may be popped open as a result of shearing along the other two boundaries (Figure 2.12b). When grain contacts are oriented inclined with respect to load axis, sliding may occur and leads to opening-mode cracks at two ends, forming wing-cracks (Figure 2.12c). The latter two cracking modes are dominant and cause damage to grain boundaries. Since salt-rock deforms plastically at the same time, crack opening is also accommodated by creeping at salt grain contacts, in addition to shearing.

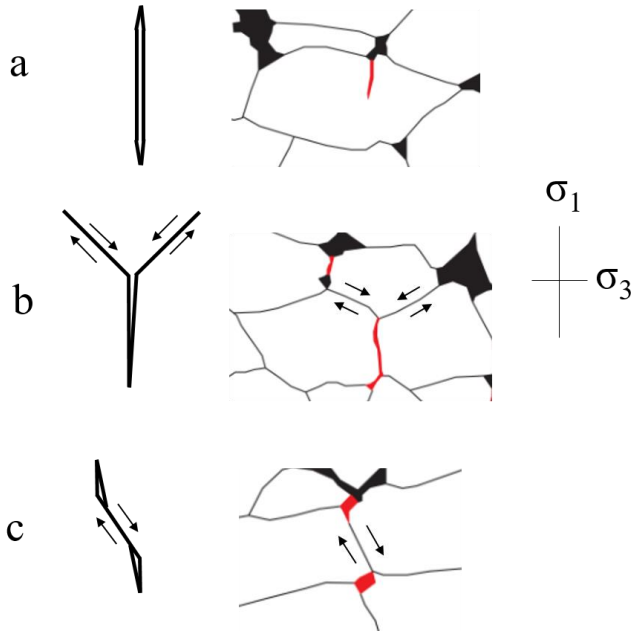

Figure 2.12 Three microcracking modes discussed by Brace et al. (1966) and corresponding examples from synthetic salt-rock microstructures; σ_1 and σ_3 are maximum and minimum principal stresses, respectively (Ding et al., 2017).

The opening-mode microcracks are fitted to ellipses using ImageJ image analysis software and the angle between the major axis and the direction perpendicular to the

load axis is plotted in rose diagrams (Figure 2.13). At different axial strains, both samples show a preferred orientation with the major axis sup-parallel to the load axis. As axial strain increases from 2.27% to 6.76%, microcrack orientation becomes more uniform with respect to the load axis.

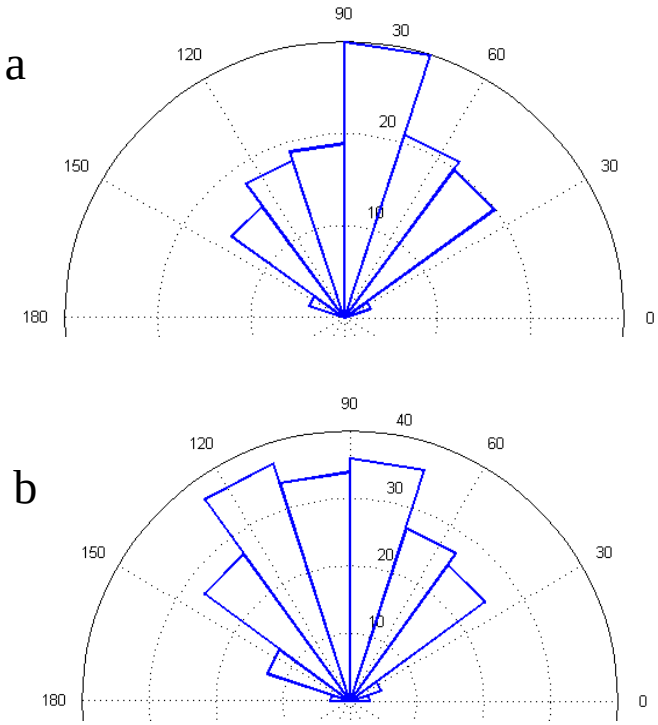

Figure 2.13 Rose diagrams of opening-mode microcrack orientation for synthetic salt-rock with (a) axial strain = 2.27%; (b) axial strain = 6.76%; the angle is between the major axis of the best fit ellipse of the microcrack and the direction perpendicular to load axis (90° is in the direction of axial stress) (Ding et al., 2017).

Opening-mode microcracks are analyzed to reveal the degree of linking with increasing deformation. Microcracks are considered linked if they connect to the same void or to a single grain contact segment oriented consistent with shear motion. It is apparent that increasing cyclic loading and deformation leads to linking between

microcracks (Figure 2.14). In the 6.76% axial strain sample, many microcracks link into long arrays in the direction of load axis, and the percentage of more than four linked microcracks is almost three times as that in the 2.27% axial strain sample. As microcracks link, the lateral (in the direction normal to the load axis) integrity of the sample is progressively decreased.

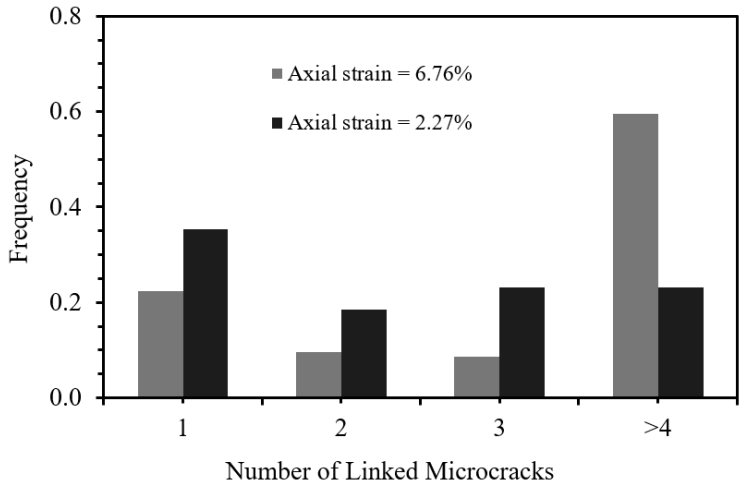

Figure 2.14 Histogram of the frequency of linked microcrack arrays versus the number of microcracks linked (Ding et al., 2017).

Microcrack linking is more severe at sample boundaries, since it is close to the free interface between the sample and the confining fluid (Figure 2.15). Nearly all inclined grain contacts are open or partially open, but the boundaries at high-angles to the load axis remain tight. Thus, linkage of microcracks in the vertical arrays essentially producing pillars that support the axial load. The observation here may be analogous to the state that precedes spalling along the free surface (if no sample jacket was present).

Further disturbance of the grain contacts by cyclic loading would cause sample to lose cohesion completely.

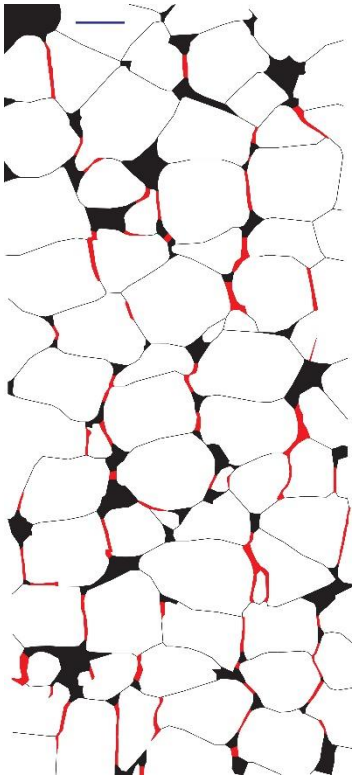

Figure 2.15 Line tracing from micrographs of salt grains (white), pores (black) and opening-mode microcracks (red) of synthetic salt-rock sample with axial strain = 6.76%; axial stress is vertical, dark blue scale bar represents 0.2 mm, images are taken close to sample boundary; the sample-fluid interface is vertical on the right side of the map (Ding et al., 2017).

2.4.3. Implications to Gas Storage Salt Cavern

In the gas storage salt caverns where wall is subject to cyclic loading, our experimental observations suggest the following mechanism for spalling. Cyclic loading at low confining pressure and temperature causes progressive microcracking at salt grain contacts. These contacts are prone to open mainly through popping by a third grain or

shearing along inclined grain boundaries. These opening-mode microcracks preferentially form parallel to the load axis. As damage accumulates, they link to form arrays. As the linked arrays increase in length and number, larger networks may form leading to complete loss of cohesion and spalling.

In this study, the synthetic samples have pores contributing greater porosity than likely occurs in natural salt-rocks. For polycrystalline aggregates that are less porous than our synthetic salt-rock samples, grain boundary shearing and opening mode microcracking would still likely occur and link to form similar arrays. In these cases, less axial strain may be necessary to achieve spalling.

2.5. Conclusions

In this section, we conducted uniaxial consolidation experiments on sieved, nominally dry granular sea salt and reagent-grade salt at different temperatures and load paths. To investigate microcrack and damage accumulation in polycrystalline aggregates, we then conducted cyclic triaxial compression tests on synthetic salt-rock samples fabricated through uniaxial consolidation. Mechanical behavior and microstructure observations demonstrate the following:

1. Consolidation in granular salt is strongly affected by temperature, whereas the grain size and load paths employed in this study show limited influence.
2. At the tested conditions, the dominant mechanism of consolidation is crystal plasticity. In some highly strained areas of the consolidated salt samples, recrystallized grains are observed and interpreted to reflect static recrystallization.

3. At room temperature and low confining pressure, grain boundary microcracking is the dominant brittle deformation mechanism in synthetic salt-rock. Grain boundary microcracks develop preferentially in the loading direction and tend to link with increasing inelastic deformation.
4. Cyclic loading leads to progressive lengthening of linked crack arrays, which maybe an import mechanism of damage development that ultimately could lead to spalling at salt cavern walls.

3. GRAIN BOUNDARY PROCESSES AND ANELASTICITY IN SEMIBRITTLE SYNTHETHIC SALT-ROCK

3.1. Introduction

Rock deforms by a variety of microprocesses, including brittle processes of fracturing and frictional sliding and viscous processes of crystal-plasticity and diffusive mass transfer (Knipe, 1989; Sibson, 1977, 1986; Tullis, 1979). Semibrittle deformation refers to the mixed mode of brittle and viscous processes both of which contribute significantly to the total deformation (Carter & Kirby, 1978; Chester, 1989; Paterson & Wong, 2005; Reber & Pec, 2018). Many research has been directed to understand this rather complex deformation regime in different rock-forming materials at a wide range of pressure, temperature, and strain rate conditions (e.g., Carter & Kirby, 1978; Kirby & Kronenberg, 1984; Chester, 1988, 1989; Hadizadeh & Tullis, 1992; Reber et al., 2015; Marti et al., 2017; Reber & Pec, 2018). Semibrittle deformation is directly relevant to many geologic processes in the crust, in particular earthquake generation. Many large earthquakes occurred in the brittle-ductile transition of the crust where semibrittle deformation prevails (Brace & Kohlstedt, 1980; Sibson, 1983). Studying the mechanical behavior of these large earthquakes requires a good understanding of the combined operation of brittle and viscous microprocesses.

Although individual microprocess (e.g., dislocation creep, pressure solution) is relatively well understood, the interplay among them is inherently complex and requires further studies. Brittle and viscous processes may interact in a variety of ways and affect

both elastic and inelastic deformation. For example, there are experimental evidences that intracrystalline plasticity affects microcracking process (Fredrich et al., 1989; Hirth & Tullis, 1994), and that grain boundary sliding may significantly lower elastic moduli of polycrystals (Ghahremani, 1980; Zener, 1941). More work is needed to elucidate how the combined operation of brittle and viscous microprocesses affects both elastic and inelastic deformation.

In this section, we report an experimental investigation aimed at understanding how elastic properties (i.e., Young's modulus and Poisson's ratio) evolve with progressive inelastic deformation and underlying micromechanisms for both elastic and inelastic deformation in the semibrittle field. We fabricated two types of synthetic salt-rocks with contrasting microstructures (i.e., porosity, dislocation density, grain size and shape) and deformed them using cyclic loading technique at room temperature and low confinement to activate semibrittle deformation. To investigate time-dependent elastic behavior (anelasticity), we applied three strain rates (3×10^{-5}, 3×10^{-6}, and 3×10^{-7} s^{-1}) in the stress cycles where elastic parameters were determined. We also employed stress relaxation technique to aid understanding of deformation mechanisms. Additionally, we characterized microstructures of key samples to provide necessary information relating elastic and inelastic deformation with micromechanisms.

3.2. Methods

3.2.1. Synthetic Salt-Rock Sample Fabrication

Reagent-grade granular salt (high purity 99 wt.%) was used to fabricate the synthetic salt-rock samples. The granular salt was sieved to separate grains 0.3-0.355

mm diameter, which were used to produce two distinct synthetic salt-rock with contrasting microstructure. The “consolidated samples” were fabricated through uniaxial consolidation of the granular salt in a hollow cylindrical steel vessel (Section 2.2.2 and 2.2.3, Ding et al., 2016). The vessel was first heated to the target temperature, and then salt was poured into the vessel, the vessel was sealed by a loading piston on each end, and evacuated. The granular salt was dried in-situ by maintaining an elevated temperature for 1.5 hours, during which the vacuum was re-established about every 15 minutes to remove additional water vapor released during heating. This step ensured consistent water content in the produced samples. The consolidation was performed by loading the granular salt from both ends at a constant displacement rate of 0.034 mm/s to reach the maximum axial-stress desired, and then the sample was quickly unloaded to zero stress. After unloading, the consolidation stack was cooled by two electric fans while maintaining the vacuum on the salt sample. Upon reaching room temperature, the entire consolidation assembly was transferred to a controlled low-humidity glove-box, where the pistons were removed and the salt sample was easily released due to the different thermal expansion coefficients of salt and steel (Peach & Spiers, 1996). The “annealed sample” was produced by uniaxial consolidation followed by annealing. For annealing, the consolidated sample was placed in a pressure vessel under elevated temperature and hydrostatic pressure for a duration of 1 week. We employed the same annealing conditions as used by Peach and Spiers (1996). Table 3.1 summarizes the fabrication conditions for the two types of synthetic salt-rock sample.

Table 3.1 Fabrication conditions for two types of synthetic salt-rock samples used in this study

	Consolidated sample	Annealed sample
Consolidation loading rate (mm/s)	0.34	0.34
Consolidation temperature (°C)	150	100
Consolidation maximum axial stress (MPa)	75	120
Annealing temperature (°C)	N/A	150
Annealing pressure (MPa)	N/A	100
Water content ppm (weight)	301±18	5.10±0.44

Halite grains absorb water vapor from atmosphere easily, and the rheologic behavior of salt-rock can be greatly influenced by the presence of trace amount of water at grain boundaries (Urai, Spiers, et al., 1986; Watanabe & Peach, 2002). To ensure consistency in water content among samples, they were stored and handled in a controlled low-humidity glove-box where relative humidity was maintained below 17% (Section 2.2.2, Ding et al., 2016). Maintaining low humidity is also crucial for making high-quality petrographic sections of salt samples, so all steps of cutting and polishing samples were also carried out using the low-humidity glove-box.

Fabricated samples are right-circular cylinders, so from measurements of dimensions and mass, the starting bulk porosity of consolidated and annealed samples was 5.45 ±0.06% and 0.54±0.08%, respectively. Consolidation produced high

dislocation density in halite grains by intracrystalline-plastic deformation, and subsequent annealing removed dislocations through recrystallization (Peach and Spiers, 1996). The consolidated samples are analogous to the pre-compacted and hardened salt aggregates that are often used to backfill salt repositories (Salzer et al., 2007), whereas the annealed samples are similar to natural salt-rocks free from recent deformation (Carter & Hansen, 1983). The contrasting microstructures of these two synthetic salt-rocks allowed detailed study of microstructural control on the mechanical behavior of salt-rock.

3.2.2. Water Content Measurement

Water content of samples was measured using a Fourier transform infrared (FTIR) spectrometer. Samples were cut into circular discs using a precision diamond saw in the low-humidity environment. No fluid was used during cutting to avoid introducing external water into the sample. In the absorbance spectrum of transmitted IR beam, the bending of water molecules and stretching of OH bonds caused peaks at wave numbers of 1650 and 3500 cm^{-1}, respectively. The peak at wave number of 1650 cm^{-1} is affected by other signals, possibly the presence of impurities. Therefore, we determined water content from the integrated area of the peak at wave number of 3500 cm^{-1}. Measurements were made on seven points evenly distributed across the circular disc.

The average water content of our two types of synthetic salt-rock samples are summarized in Table 3.2. The values in ppm ($OH/10^6$ NaCl) were determined by dividing the integrated area of the peak at wave number of 3500 cm^{-1} by a calibration factor of 1.07. This calibration factor was determined using the IR absorbance data of

liquid water from Thompson (1965) and assuming the effects of NaCl concentration of water on IR absorption is negligible. Assuming two OH bonds make up one water molecule, the water content in ppm (H_2O /10^6 NaCl) is simply half of the value in ppm (OH/10^6 NaCl). Using molar mass of water and sodium chloride, the water content in ppm (weight H_2O /10^6 NaCl) can be calculated from the value in ppm (H_2O /10^6 NaCl).

Table 3.2 Water content of the synthetic salt-rock samples prior to triaxial deformation

	Consolidated sample	Annealed sample
Integrated area[a] (cm^{-1})	467.48±28.08	7.59±0.71
Water content ppm (OH/10^6 NaCl)	1954.61±117.43	33.07±2.86
Water content ppm (H_2O/10^6 NaCl)	977.31±58.71	16.54±1.43
Water content ppm (weight H_2O/10^6 NaCl)	301.22±18.01	5.10±0.44

[a]Integrated area was measured for the peak in IR absorbance spectrum at a wave number of 3500 cm^{-1}.

3.2.3. Cyclic Triaxial Compression and Stress Relaxation Experiments

To achieve semibrittle deformation, the tests were performed at room temperature and a confining pressure of 1 MPa (Table 3.3). While maintaining a constant confining pressure and using a constant axial displacement rate, the differential stress in the direction of sample axis was varied in two types of load cycles: 1) small-load cycles in which differential stress was cycled between zero and ~6.5 MPa and the sample deformed elastically, and 2) large-load cycle in which differential stress was cycled between zero and the flow strength, and the sample was deformed permanently by a specified increment of axial shortening before the unload portion of the cycle (Figure 3.1). Except for those performed at zero axial strain, small-load cycles were

started ~15 minutes after the preceding unload from flow strength was completed to ensure a consistent amount of rest time before initiating measurements of anelasticity in all tests. This step reduced the impact of time-dependent deformation from large-load cycles on subsequent small-load cycles. A constant strain rate of 3×10^{-6} s^{-1} was used for large-load cycles, while three different strain rates of 3×10^{-5}, 3×10^{-6}, and 3×10^{-7} s^{-1} were used in small-load cycles to investigate the rate-dependence of anelastic behavior. Axial and radial strains were measured by two rosette strain gauges of 0.25-inch gauge length and 350 Ω resistance. Strain gauges were glued at opposing sides of the sample and averaged to account for sample tilting during deformation tests (Figure 3.1). Differential force was measured through an internal force gauge that is in direct contact with sample assembly and unaffected by the friction between loading piston and sealing stack. The differential force gauge and confining pressure are accurate to ±70 N, ±0.01 MPa, respectively. The triaxial deformation apparatus used in this study has been described in detail by French et al. (2015).

Table 3.3 Samples and experiments[a]

Sample No.	Sample type	Final axial strain (%)	Test performed	Notes
60209R	Granular	N/A	N/A	sectioned
70516	Consolidated	N/A	undeformed	sectioned
61003	Consolidated	2.77[b]	cyclic loading	sectioned
61123	Consolidated	7.31[b]	cyclic loading	sectioned
80204	Consolidated	8.79	stress relaxation	sectioned
80306	Consolidated	3.82	cyclic loading, hold	first-round of cyclic loading
80306	Consolidated	3.79	cyclic loading	second-round of cyclic loading
61030	Annealed	N/A	undeformed	sectioned
70304	Annealed	4.87[b]	cyclic loading	sectioned
70305-2	Annealed	3.51	cyclic loading, hold	first-round of cyclic loading
70305-2	Annealed	2.96	cyclic loading, hold, stress relaxation	second-round of cyclic loading

[a]All experiments were conducted at room temperature and a confining pressure of 1MPa.
[b]Final axial strains equivalent to strain gauge measurements were estimated based on total axial strains measured by an external DCDT and experiments with both strain gauge and DCDT strain measurements (i.e., sample 80306 and 70305-2)

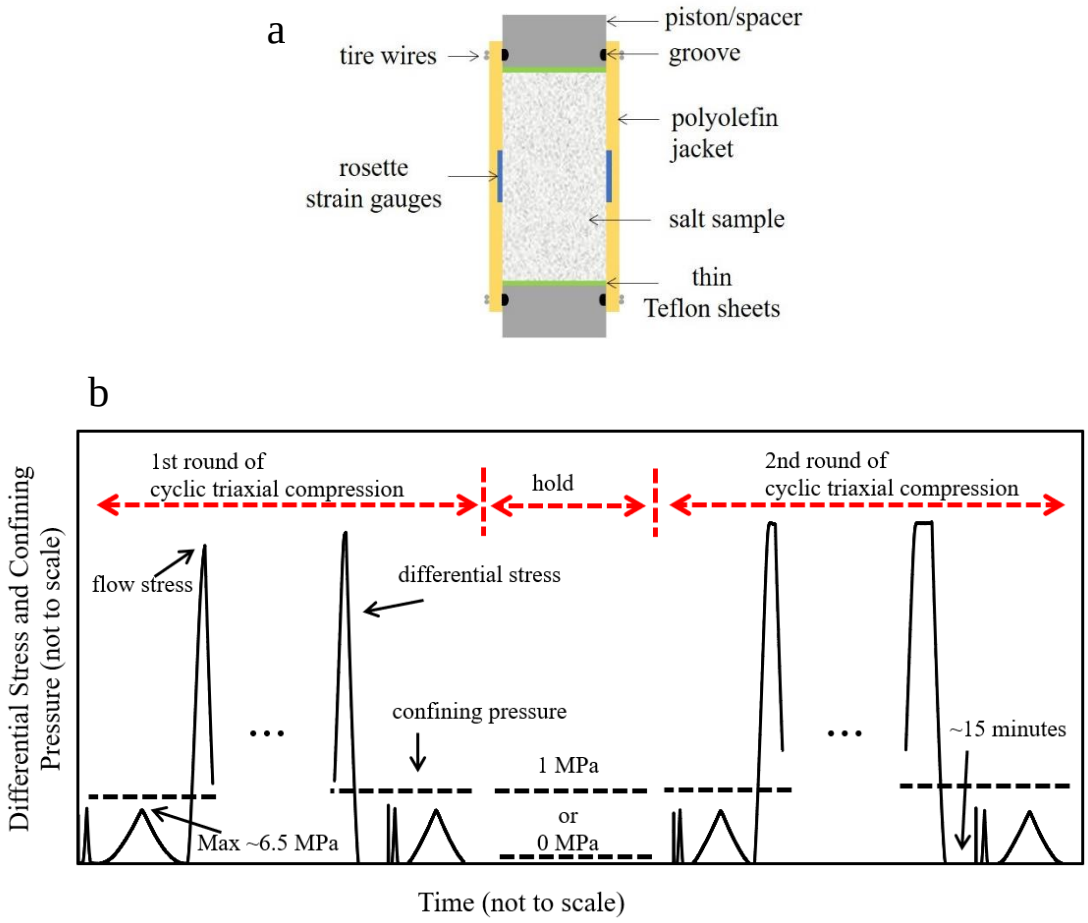

Figure 3.1 Schematic of (a) sample assembly and (b) load paths of cyclic triaxial compression test. Small- and large- load stress cycles and hold between cyclic loading tests are illustrated.

To investigate the time dependence of changes in elastic properties, "hold" was employed between two rounds of cyclic loading tests on a sample. The salt-rock sample was first deformed to approximately 4% axial strain, close to the linear limit of the strain gauges (4.5%), to record the evolution of elastic properties with axial strain. Then the sample was removed from the vessel and the strain gauges were replaced, after which samples were held at either at 0 or 1 MPa confining pressure for a period of time (1-5

days). After the hold, a second-round of cyclic loading was performed on the sample following similar stress cycles as used in the first-round (Figure 3.1).

Stress relaxation tests also were conducted to gain more information on time-dependence and deformation mechanisms (Table 3.3). The loading piston was abruptly stopped when a sample was being deformed at a constant strain rate. Differential stress on the sample decreases with time as elastic energy stored in the sample and loading rig is converted into inelastic strain. The stress relaxation technique allows determination of inelastic deformation mechanisms through the analysis of strain rate versus stress behavior (French et al., 2015; Rutter et al., 1978).

3.2.4. Microstructural Characterization

Loosely packed salt grains, the consolidated and annealed synthetic salt-rock samples, and key synthetic salt-rock samples deformed in triaxial compression, were prepared for microscopic study (Table 3.3). The sectioning and etching procedures followed those used in Section 2.2.5. Microstructures were characterized under both reflected- and transmitted- light. Observations focus on the central part of the sample, where the strain gauges were attached, for the benefit of direct correlation between microstructures and mechanical data as well as reduced sample end-effects. In addition to detailed observation on a few halite grains in a single petrographic image, tens of petrographic images were stitched together to allow observation on one to two hundred grains, which covers about 40% of the strain gauge area.

3.3. Results

3.3.1. Mechanical Behavior

3.3.1.1. Overall Stress-Strain Behavior

At room temperature and a confining pressure of 1 MPa, the mechanical behavior of consolidated samples is characterized by approximately linear elastic deformation, yielding at approximately 36 MPa, followed by inelastic deformation at relatively constant stress of ~40 MPa (Figure 3.2). The inelastic deformation is homogeneous across the samples with slight barreling in the middle, representing macroscopic ductile flow. In the beginning of the deformation experiment, the sample compacts slightly and then dilates thereafter, i.e., pore and crack volume increases. The flow strength for the two rounds of cyclic loading tests, separated by a 34.5 hour hold without confinement, are highly consistent.

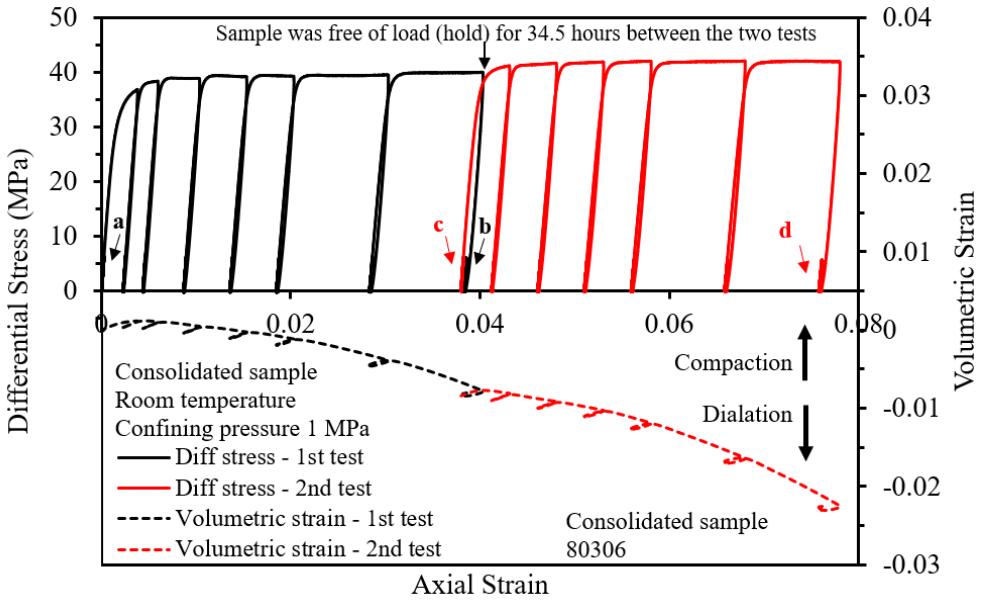

Figure 3.2 Plots of differential stress and volumetric strain versus axial strain for consolidated sample 80306. The first and last small-load cycles for each round of cyclic compression test are indicated by letters. Note small-load cycles are not readily seen due to scale and masking by large-load cycles.

At the same testing conditions of consolidated samples, the annealed samples show similar mechanical behavior, except for yielding at lower stress (~13 MPa) and work-hardening at a decreasing rate throughout the deformation test. The final strength of the annealed samples is about 80% of the flow strength of the consolidated samples. The work hardening is accompanied by progressive increase in linear elastic behavior for each load cycle (Figure 3.3). Dilatancy occurs throughout the deformation test at an increasing rate indicative of the development of pore and crack porosity. At the end of the first-round of cyclic loading, after the final unload and removal of confining pressure, the annealed sample displayed apparent axial elongation as occurs by unloading cracks. Visual inspection did not reveal any cracks, but subsequent microstructural observation confirmed the presence of unloading cracks. The sample was

held unconfined for 66 hours before the second-round cyclic loading test was initiated. The first loading cycle shows apparent reduction in slope relative to earlier load cycles, likely from the presence of unloading cracks. After imposing ~0.5% inelastic axial strain, the slopes of unload-load cycles are comparable with those of the first-round of cyclic loading test, indicating the unloading cracks were closed after one large-load cycle.

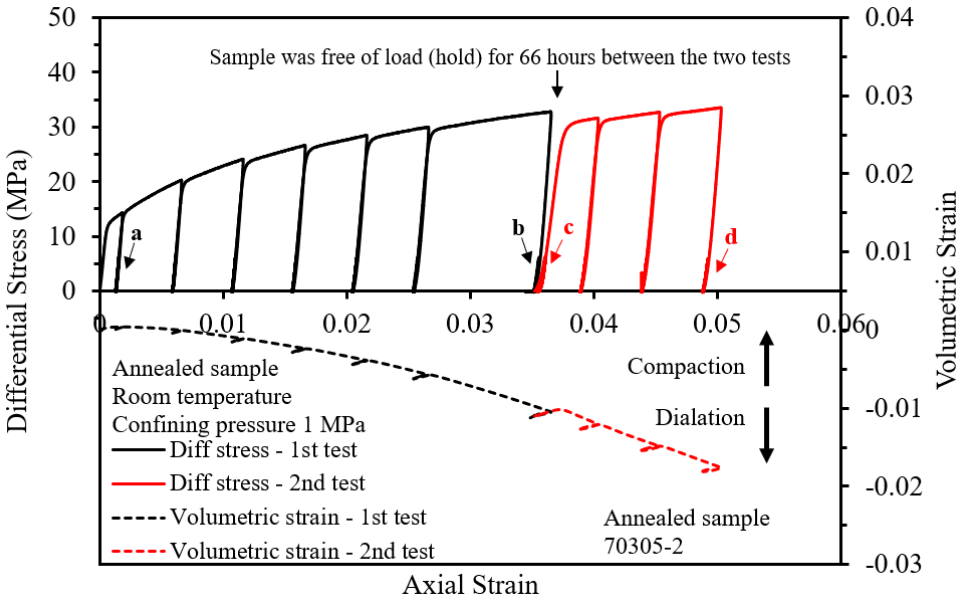

Figure 3.3 Plots of differential stress and volumetric strain versus axial strain for annealed sample 70305-2. The first and last small-load cycles for each round of cyclic compression test are indicated by letters. Note small-load cycles are not readily seen due to scale and masking by large-load cycles.

3.3.1.2. Stress-Strain Behavior during Small-Load Cycles

Small-load cycles of consolidated samples exhibit characteristic stress-strain behavior (Figure 3.4). For the first-round of cyclic loading at zero axial strain, before the first large-cycle loading, samples show nearly perfect-linear elastic deformation, and the

subsequent small-load cycles of different strain rates overlie almost exactly (Figure 3.4a). As permanent axial strain increased with the large-load cycling, the elastic response during the small-load cycles progressively developed a non-linear elastic response with hysteresis that is rate-dependent. Slower loading led to more compliant behavior and hysteresis (Figure 3.4b); however, even with hysteresis, the axial strain was nearly fully recovered during a single small load-unload cycle regardless of strain rate, whereas radial strain recovered more than initially achieved. During the ~15 minutes between complete unload of large cycles and start of small cycles, appreciable axial and radial strain was recovered providing evidence of anelasticity consistent with the rate-dependence of elastic behavior seen in the small-load cycles (Figure 3.4b, d). For the second-round cyclic loading test, after the days-long hold with no confinement, the behavior during the first small-load cycle showed that the sample had recovered to the initial state (i.e., the state prior to initiating the first-round of small load cycling) where hysteresis and rate-dependence were absent (Figure 3.4c). With continued deformation, the sample displayed the same evolution as in the first-round of cyclic loading before the hold: increasing rate-dependence and hysteresis with permanent strain (Figure 3.4d).

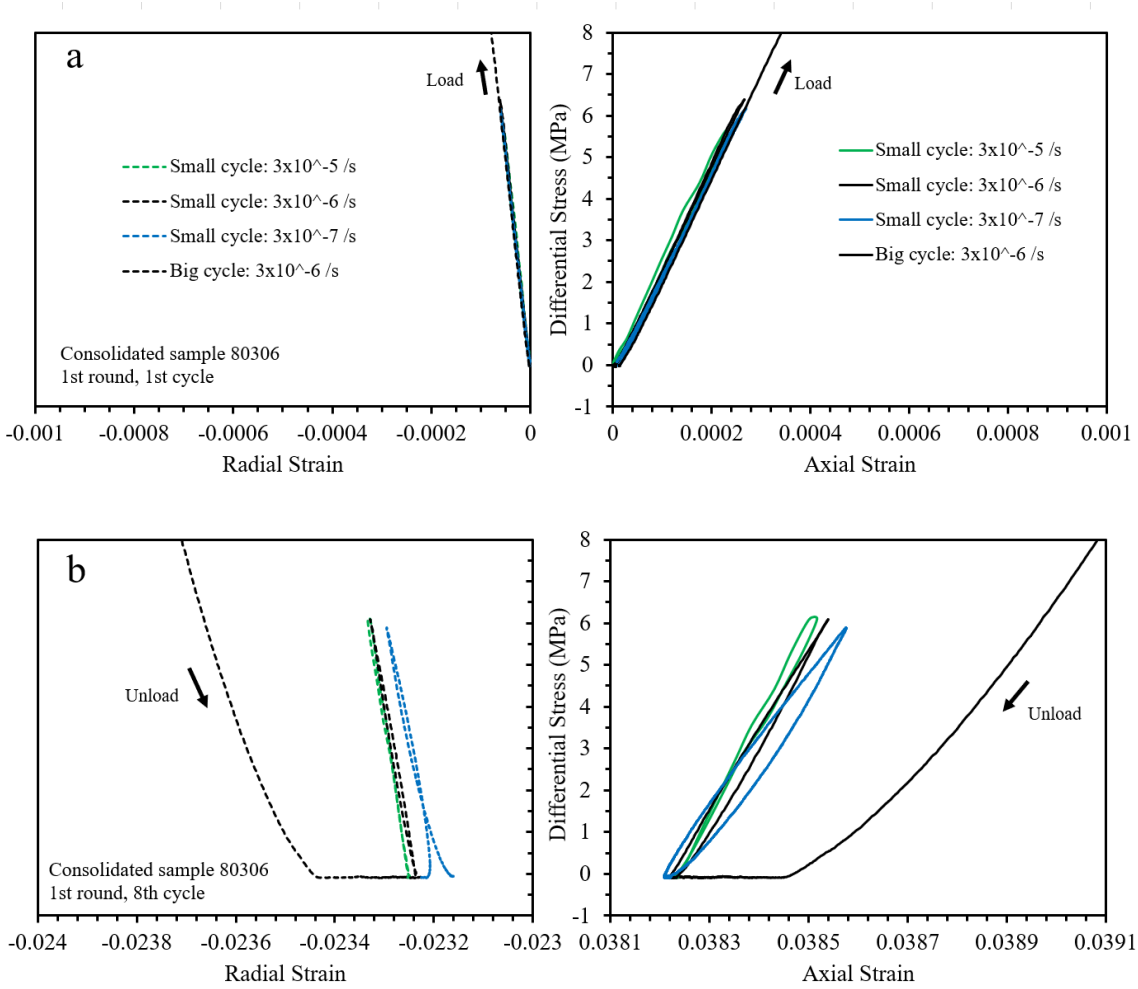

Figure 3.4 Plots of differential stress versus axial and radial strain of small-load cycles for consolidated sample 80306. The first and last small-load cycles for two rounds of cyclic compression tests are shown. Refer Figure 3.2 for locations of these small-load cycles in the overall stress-strain curve. Loading and unloading directions of large-load cycles are indicated by arrows.

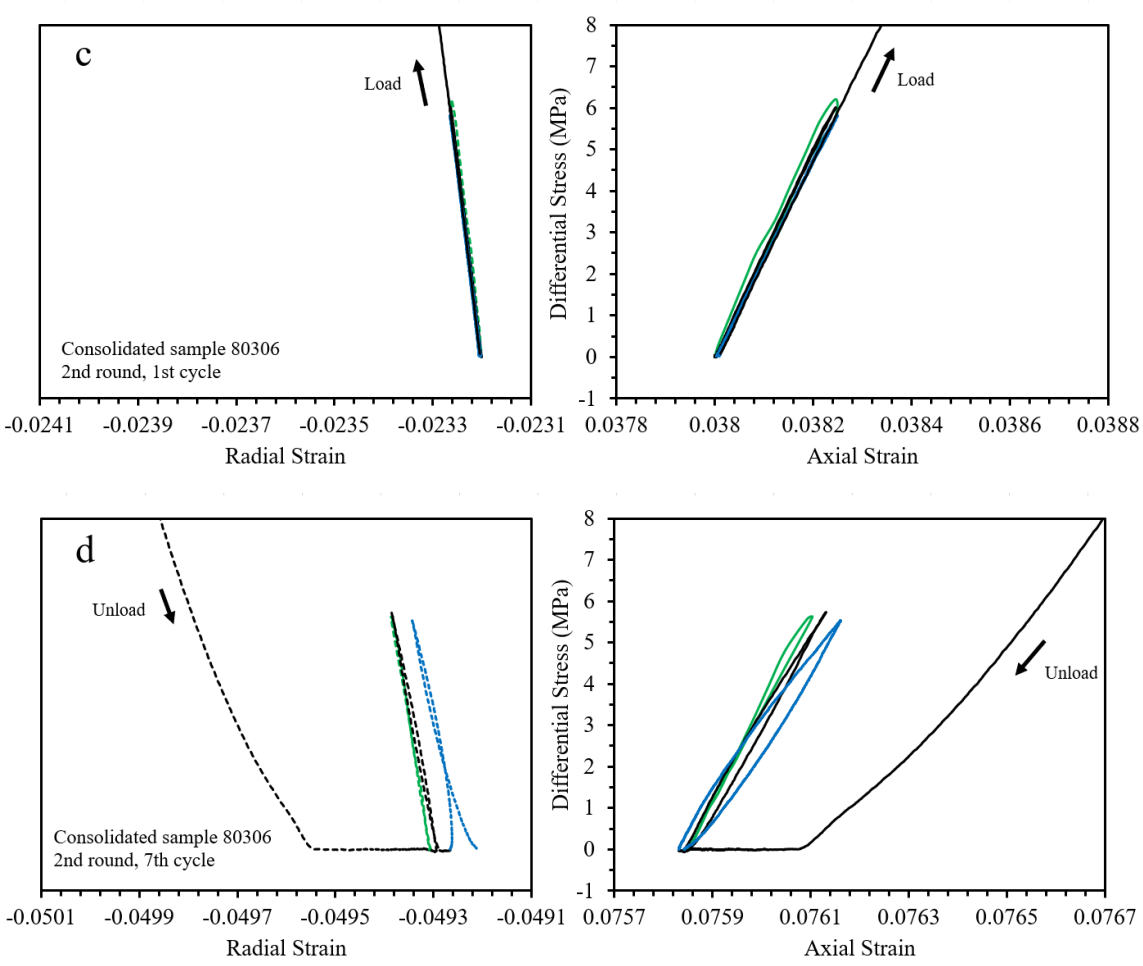

Figure 3.4 Continued.

The small-load cycles of annealed samples show quite different stress-strain behavior from those of consolidated samples (Figure 3.5). Rate-dependence and hysteresis are absent throughout the deformation tests. Closing of unloading cracks is evident in the first small-load cycles of the second-round test (Figure 3.5c). Following small-load cycles show similar stress-strain behaviors as those of the first-round test (Figure 3.5d). Very little axial and radial strain is recovered during the ~15 minutes between complete unload of large cycles and the start of small cycles (Figure 3.5b, d).

While small stress cycles using low strain rates (i.e., 3×10^{-6} and 3×10^{-7} s^{-1}) show highly consistent behavior for all experiments, large hysteresis loops are sometimes displayed for the highest strain rate (i.e., 3×10^{-5}) which is inconsistent with the behavior of adjacent stress cycles (Figure 3.5b). In these cycles the loading-unloading occurs over a very short period time for the highest strain rate (less than 20 seconds), and delays associated with reversing the motor may have affected the stress loop.

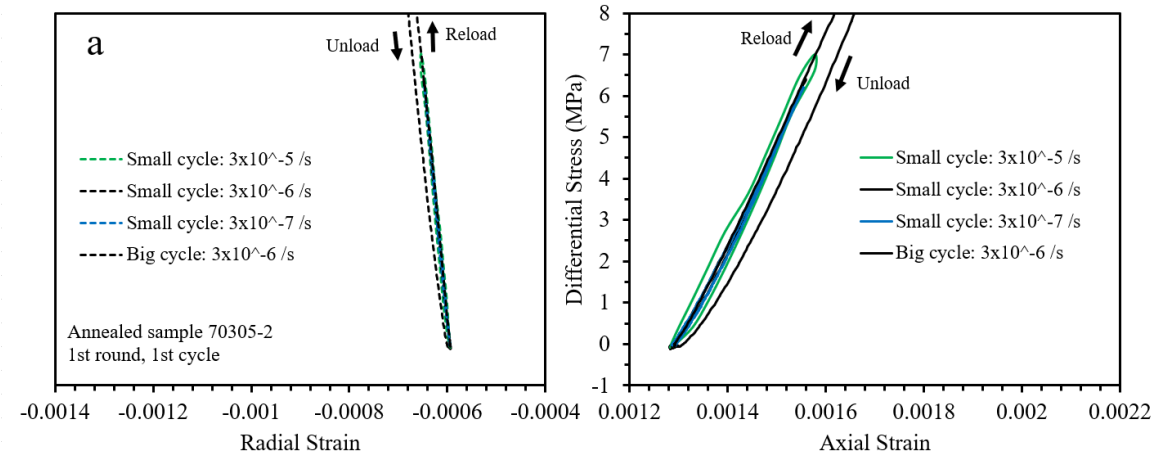

Figure 3.5 Plots of differential stress versus axial and radial strain of small-load cycles for annealed sample 70305-2. The first and last small-load cycles for two rounds of cyclic compression tests are shown. Refer Figure 3.3 for locations of these small-load cycles in the overall stress-strain curve. Loading and unloading directions of large-load cycles are indicated by arrows.

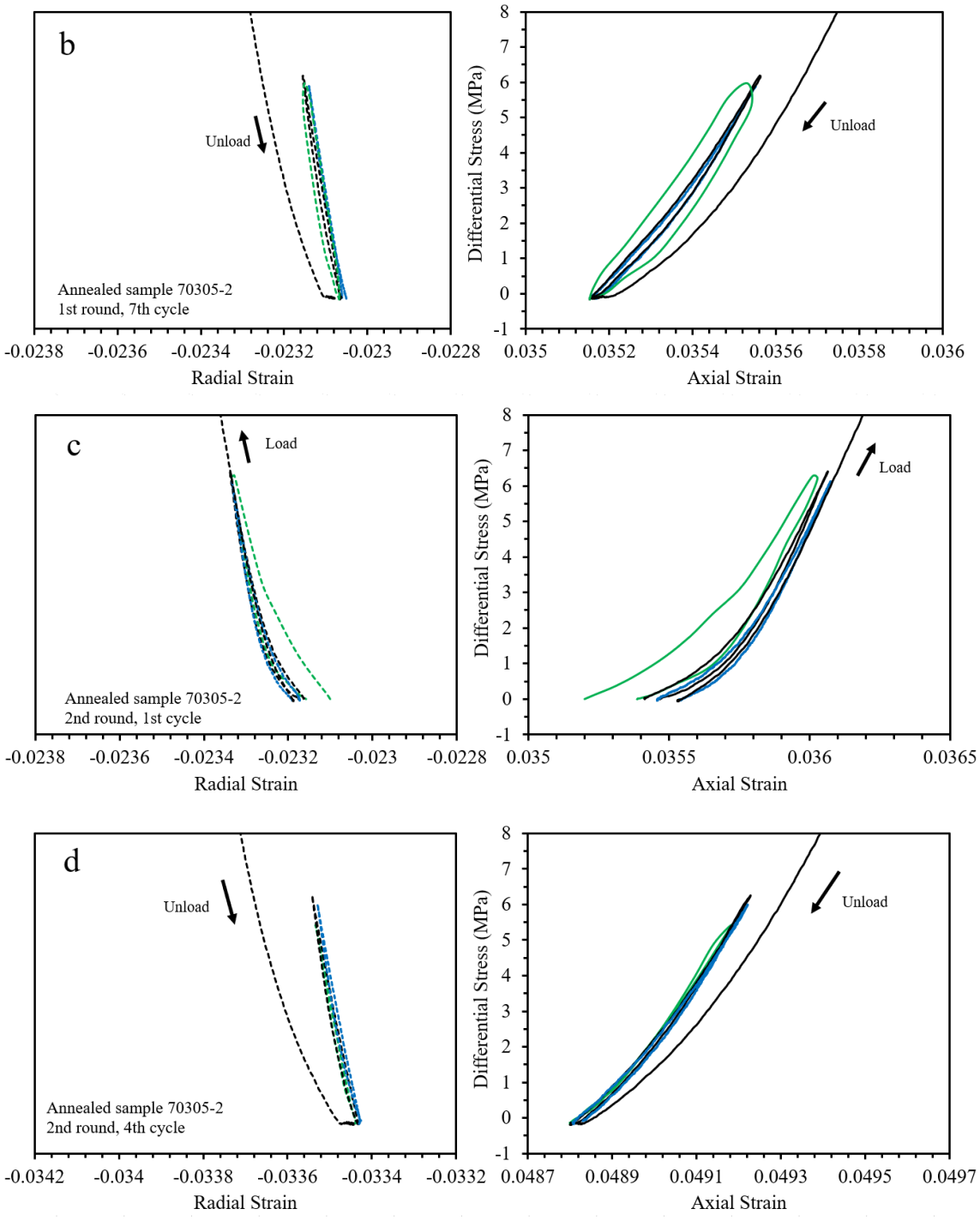

Figure 3.5 Continued.

3.3.1.3. Young's Modulus and Poisson's Ratio

Young's modulus and Poisson's ratio were calculated for the differential stress range of 2.5 and 5.5 MPa using linear fitting to the stress-strain data of either loading or unloading sections of these small-load cycles. This differential stress range covers a major part of the stress cycling of small-load cycles (between 0 and 6.5 MPa) and therefore reflects the overall slopes of load cycles. As shown in the previous section, axial strain was nearly fully recovered during small-load cycles even when there is appreciable hysteresis. Therefore, the stress-strain behavior of small-load cycles is considered entirely elastic. The evolution of Young's modulus and Poisson's ratio determined from the loading and unloading sections of the small-load cycles share the same trend with changes in the unloading sections are smaller. Same observation applies to these two elastic properties if determined from the middle differential stress range (i.e., ~ 20 MPa) of the large-load cycles. Here we report Young's moduli and Poisson's ratios determined from the loading sections of the small-load cycles as a representation.

For consolidated samples, Young's moduli of small-load cycles show clear evolution with inelastic deformation (Figure 3.6a). For the first-round of cyclic loading, Young's moduli decrease with increasing inelastic deformation. At zero axial strain, Young's moduli of different loading rates are similar. As deformation proceeded, they become progressively different for different rates. After the days-long hold, in the first set of small-load cycles of the second-round test, Young's moduli are nearly the same as original values (i.e., at zero axial strain) and are rate-insensitive. With further deformation, Young's moduli decrease quickly and develop pronounced rate-

dependence, repeating the evolution shown in the first-round test. Poisson's ratios exhibit the opposite trend: they increase with increasing inelastic deformation (Figure 3.6b). Similar to the evolution of Young's moduli, Poisson's ratios are initially rate-independent but progressively increase in rate-dependence with increasing inelastic deformation. After the hold, Poisson's ratios recover significantly and return to rate-independence, but then repeat the same evolution as seen in the pre-hold round.

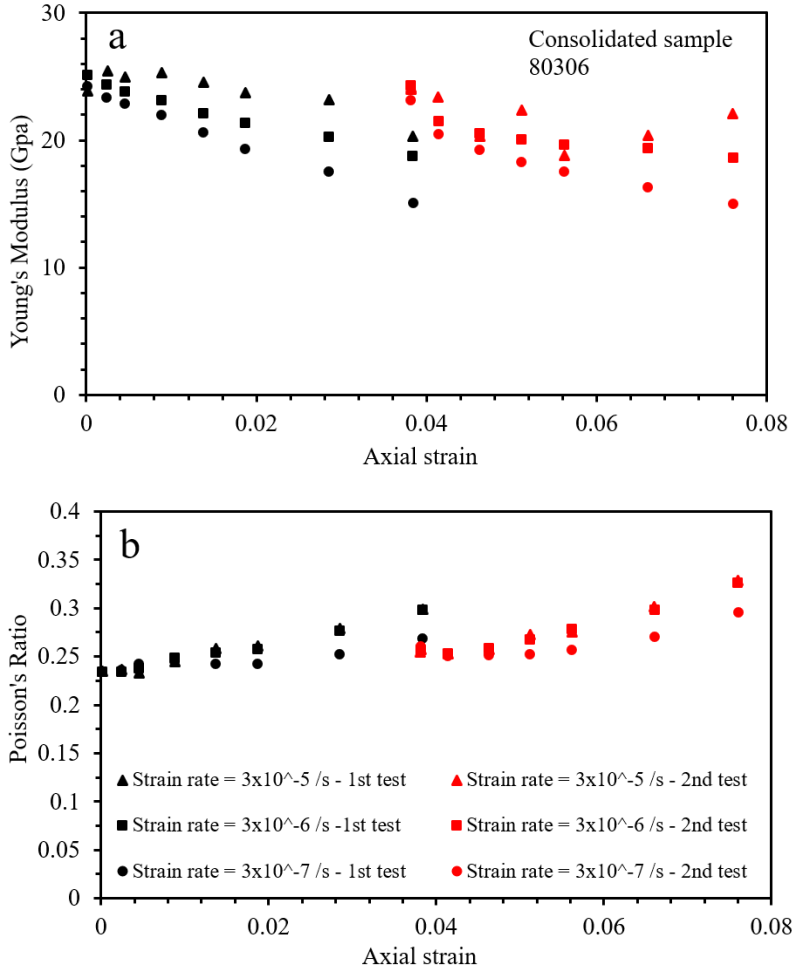

Figure 3.6 Plots of Young's modulus (a) and Poisson's ratio (b) as a function of axial strain for consolidated sample 80306. Young's moduli and Poisson's ratios were calculated for the loading segments of small-load stress cycles in the differential stress range between 2.5 and 5.5 MPa.

Young's moduli of annealed samples exhibit a different evolution with increasing inelastic deformation than that of consolidated samples (Figure 3.7a). In the first-round test, Young's moduli are similar in the first two small-load cycles, but then decrease continuously thereafter. In the second-round test, after a hold for 66 hours without confinement, the first small load cycles show abnormally low Young's moduli due to closing of the unloading cracks (Figure 3.5c). In subsequent cycles, Young's

moduli maintain similar values slightly lower than those of the last cycles of the first-round test, without any sign of recovery to the original values (i.e., at zero axial strain). Unlike the consolidated sample, Young's moduli of annealed samples are rate-independent regardless of the imposed inelastic strain. Poisson's ratios of annealed samples increase with increasing inelastic strain (Figure 3.7b). Neither strain rate nor a long hold affects the evolution of Poisson's ratio.

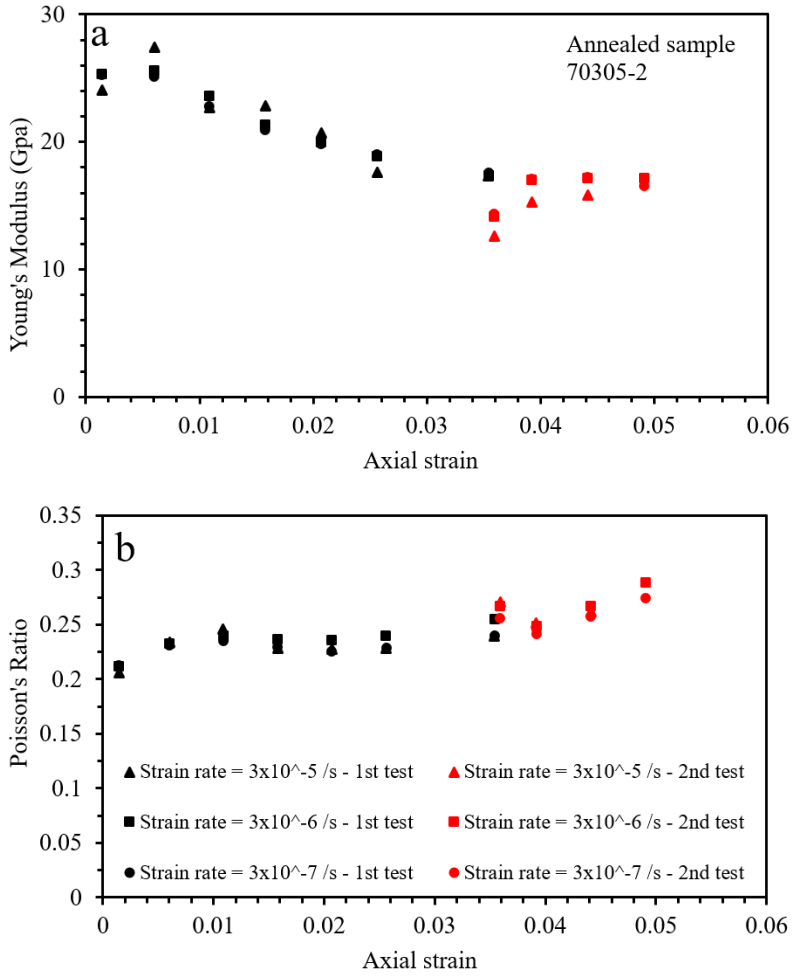

Figure 3.7 Plots of Young's modulus and Poisson's ratio (b) as a function of axial strain for annealed sample 70305-2. Young's moduli and Poisson's ratios were calculated for the loading segments of small-load stress cycles in the differential stress range between 2.5 and 5.5 MPa.

3.3.1.4. The Effect of Holds for Elastic Properties

As shown by the data of Young's modulus and Poisson's ratio, imposing a hold led to a recovery from the degraded values produced during permanent flow to nearly the original values prior to permanent deformation. The recovery occurs very rapidly in consolidated samples; experiments show the Young's moduli recovered to 96% of the

original values in less than 22 hours. The rapid recovery did not require confining pressure or differential stress.

Elastic properties of annealed samples do not recover after a hold at zero pressure for 66 hours because of the presence of the unloading cracks (Figure 3.7); however, recovery of elastic properties does occur once unloading cracks are closed at 1 MPa confining pressure (Figure 3.8). Compared to consolidated samples, recovery in annealed samples is much slower even if the sample is under pressure and stress. After ~27 hours under confining pressure, Young's modulus recovers to only 66% to 71% of the original value. With additional ~90 hours under both pressure and differential stress (during stress relaxation test), Young's modulus recovers to 89% of the original value.

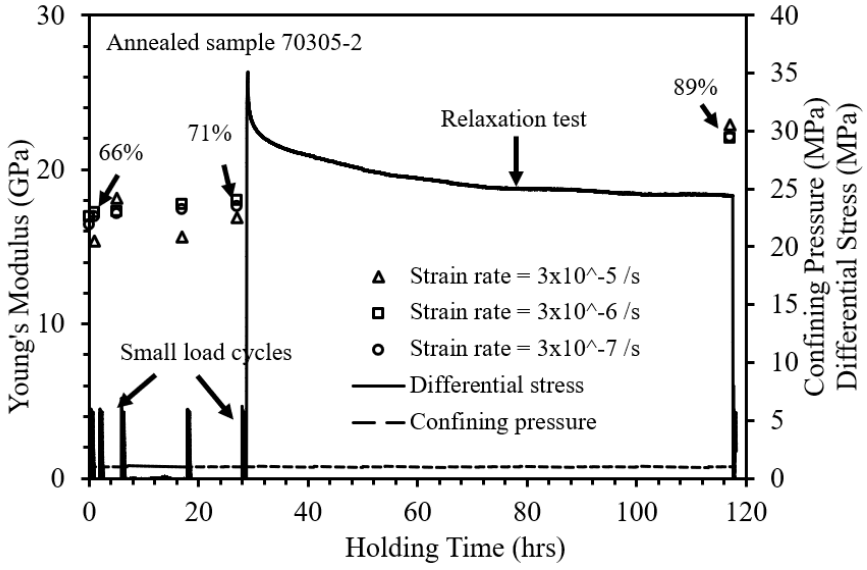

Figure 3.8 Plots of Young's modulus as a function of hold time for annealed sample 70305-2. The hold time is relative to the end of the last (4th) small-load cycles of the second-round test in Figure 3.3. Percentage numbers are relative to the original Young's modulus (i.e., at zero axial strain).

3.3.1.5. Stress Relaxation Behavior

The stress relaxation started at flow stress and stopped when strain rate reached 1×10^{-9} s^{-1} or below. When plotting strain rate versus stress in logarithmic scales, different microprocesses may be identified by different slopes. These slopes correspond to the stress exponents of rheologic flow laws and have characteristic values for micromechanisms such as dislocation glide and diffusion (e.g., Zhang et al., 2007). The stress relaxation behavior of consolidated samples reveals two deformation regimes: high stress exponent regime at high strain rates and low stress exponent regime at low strain rates (Figure 3.9). The stress exponents of these two deformation regimes are 8.8 and 0.9, respectively. The transition between these two regimes is gradual, characterized by an inflection point at a strain rate of ~2 x 10^{-8} s^{-1}.

The stress relaxation behavior of annealed samples shows only high stress exponent deformation regime from strain rates of 5×10^{-6} s^{-1} to as low as 4×10^{-10} s^{-1} (Figure 3.9). Very limited stress drop occurred during stress relaxation test which was manifested as a high stress exponent of 25.4.

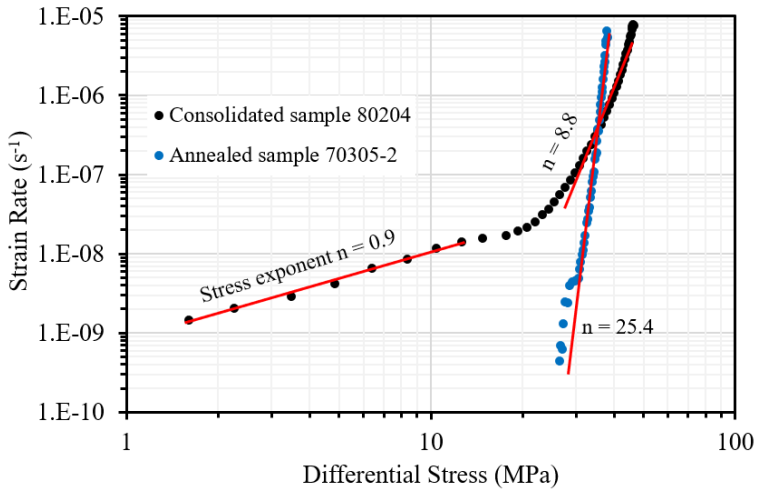

Figure 3.9 Plots of strain rate versus differential stress derived from stress relaxation tests for consolidated and annealed samples (80204 and 70305-2, respectively). Stress exponents are determined for deformation regimes by linear fitting to data shown by the red lines.

3.3.2. Microstructures

3.3.2.1. Starting Material

The as-received reagent-grade granular salt consists of cubic-shaped grains with fairly sharp corners and show very little evidence of dislocation structures after etching (Figure 3.10a). Individual grains often contain fluid inclusions that appear as dark pits in the petrographic image. Fluid inclusions exhibit cubic, tubular or irregular shapes, and may be isolated or arranged in linear arrays. Their sizes vary from tens of microns to less than one micron.

After consolidation, the initially cubic grains have more rounded corners due to intracrystalline plastic deformation (Figure 3.10b). Grain contacts appear fully closed and are often straight or only slightly curved. Porosity occurs at places where three or more grains come together. The dominant grain substructures are the well-developed,

dense, linear etch features, termed slip lines. The wavy slip lines are indications of dislocation glide controlled by cross slip of screw dislocations (Senseny et al., 1992; Spiers & Carter, 1996). The slip lines are generally oriented at similar orientations in individual grains reflecting crystallographic orientation. At grain contacts where deformation is most intense, slip lines of two major orientations intersect each other due to activation of different slip systems. In some of the most highly strained areas, high dislocation density led to development of recrystallized grains. The recrystallized grains, characterized by straight boundaries and dislocation-feature-free interiors, are usually small and uncommon (less than 4.8% of total grains). These recrystallized grains formed at the expense of the highly deformed grains. Minor intragranular cracks often intersect fluid inclusions or develop along fluid inclusion arrays, likely reflecting stress concentration by inclusions. Less than 6.4% of all grains show intergranular cracks, which indicates limited influence of brittle deformation during consolidation. Grain boundaries are well bonded with presence of dense and irregular-shaped fluid inclusions (Figure 3.11a, b). These grain boundary fluid inclusions typically measure less than ten-micron long.

For the annealed samples, annealing completely changed the microstructure and produced strain-free grains in polygonal shapes (Figure 3.10c). All grain contacts are fully closed and pores are not observed at the optical microscopic scale. Annealing reduced the fluid inclusion density and removed most of the larger inclusions in grain interiors. Compared to the consolidated samples, annealing produced a smaller average grain size (0.241 mm) and much wider range of grain sizes (0.025-0.833 mm). No

microcracks are observed in annealed samples. Grain boundaries are well bonded and display dense and nearly equal-dimension fluid inclusions that measure less than a few microns in diameter (Figure 3.11c, d).

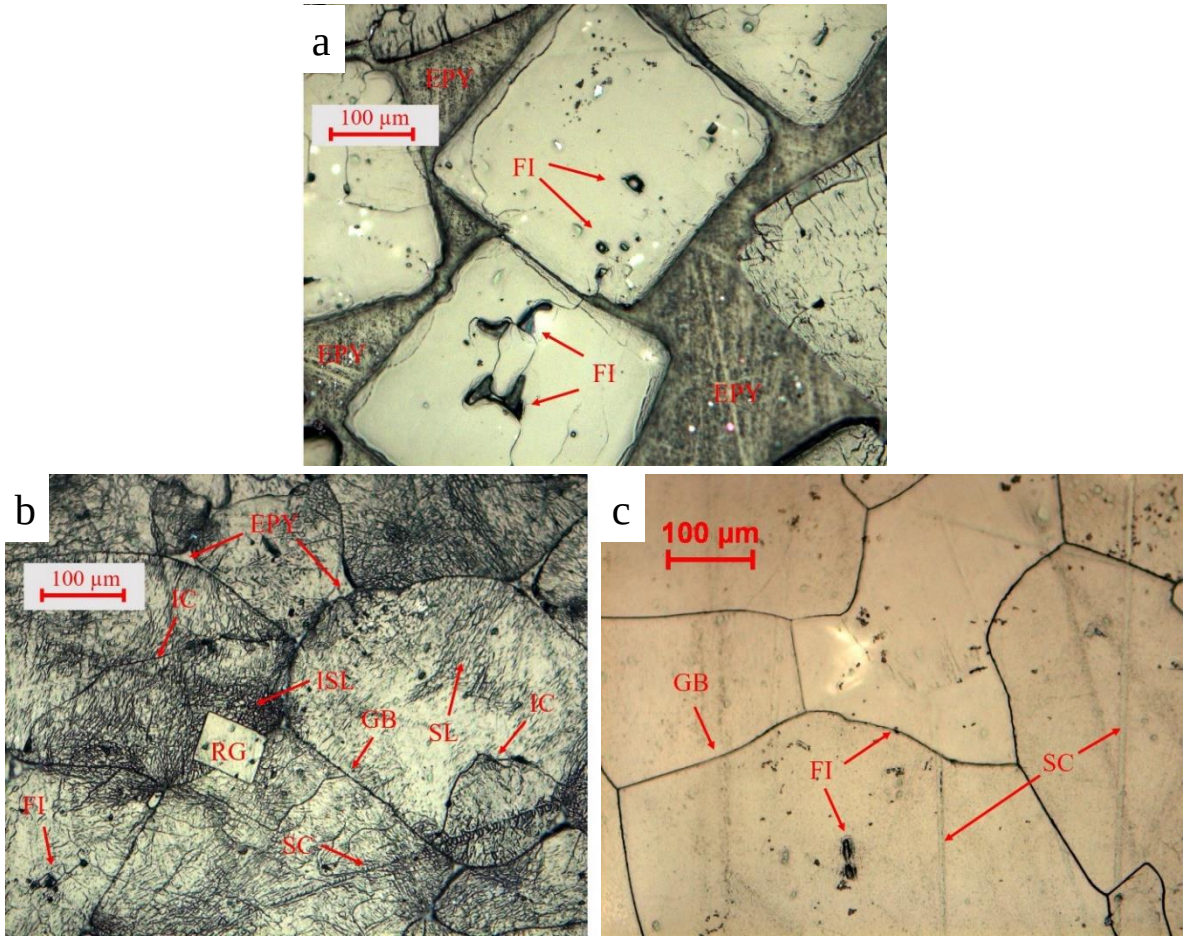

Figure 3.10 Reflected-light micrographs of (a) reagent-grade granular salt sample 60209R, (b) undeformed consolidated sample 70516, and (c) undeformed annealed sample 61030. Polished surface was chemically etched. GB – grain boundary, EPY – epoxy (pore), RG – recrystallized grain, SL – slip lines, IC – intragranular cracks, ISL – intersected slip lines, FI – fluid inclusions intersected the polished surface, SC – scratch resulted from polishing.

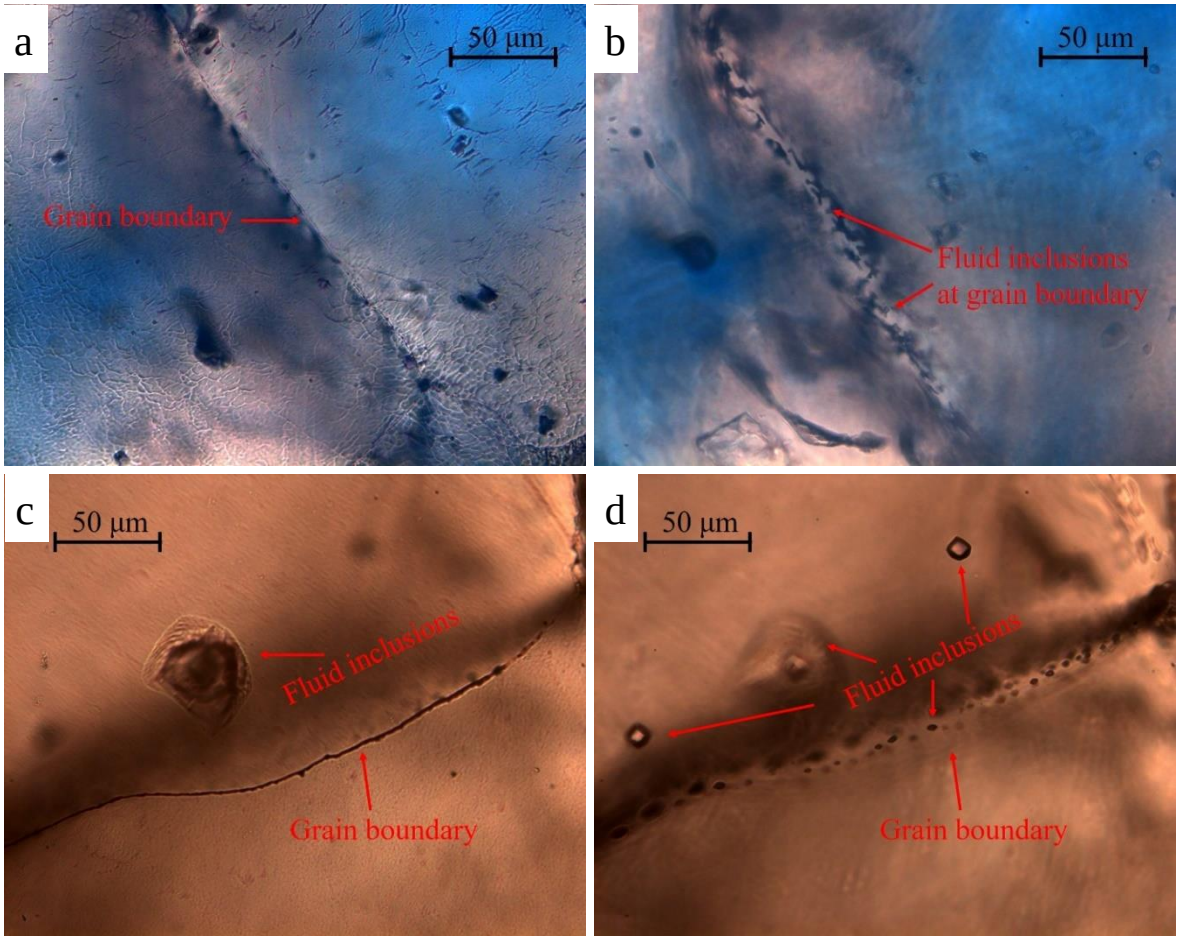

Figure 3.11 Transmitted-light micrographs of (a) and (b) undeformed consolidated sample 70516, (c) and (d) undeformed annealed sample 61030. (a) and (c) are focused on the polished surface, (b) and (d) are focused below the polished surfaces of (a) and (c) to reveal grain boundary structures.

3.3.2.2. Deformed Samples

Triaxial compression of consolidated samples led to an increase in the density of slip lines, characterized by an overall darker appearance in photomicrographs (compare Figure 3.10b with 3.12a, b, and c). Two sets of recrystallized grains are observed: one set shows no sign of dislocation substructure; and the other set displays wavy slip lines with similar characteristics as those of original grains after consolidation (Figure 3.12a). The majority of these recrystallized grains appear in euhedral shapes and reside either at grain boundaries or within grains that is close to fluid inclusions. The total density of recrystallized grains is low, ranging from 3% to 7%. Particle analysis was performed on triaxially-deformed consolidated-samples with 0%, 2.77%, and 7.31% axial strain to evaluate grain flattening by intracrystalline plasticity. The halite grains were best fitted to ellipses of the same area. Then the ratio of minor to major axis was calculated to represent the degree of flattening. These ratios are 0.671, 0.650, and 0.639, respectively. The only slight decrease of the flattening ratio with increasing axial strain indicates grain flattening was insignificant during triaxial deformation of the consolidated samples.

The most obvious deformation feature in the triaxial deformed samples are grain boundary opening-mode cracks, which can be easily identified as the grain boundaries on two sides of the opening match exactly suggesting they were previously in contact (Figure 3.12b, c). These grain boundary opening-mode cracks distribute uniformly across sample and preferentially orient parallel or sub-parallel to differential load axis (Figure 2.14c). They tend to link by connecting to the same pores. The density, aperture, and linking of these microcracks increase with increasing inelastic strain (Section 2.3.2,

Ding et al., 2017). Intragranular cracking was minor and often associated with fluid inclusions. Some of the fluid inclusions in grain interior, shown as dark pits in micrograph, show greater opening than generally observed in consolidated samples suggesting cracking caused by differential loading (Figure 3.12b). In the consolidated sample deformed to an axial strain of 7.31%, only 7.6% of total grains contain intragranular cracks, which is slightly higher than the background intragranular cracks observed at zero axial strain (6.4%). Among these intragranular cracks, 81% of them are associated with fluid inclusions.

Under transmitted-light, high-density and irregular-shaped fluid inclusions are observed at closed grain boundaries of deformed samples (Figure 3.13a, b). These fluid inclusions appear in all closed grain boundaries. The morphology of these fluid inclusions is similar to that of undeformed sample (compare Figure 3.11a, b with 3.13a, b).

Triaxial deformation of the annealed samples produced wavy slip lines in the initially strain-free halite grains (Figure 3.12d). These slip lines are mostly concentrated at grain contacts and their density is much lower than that in consolidated samples. Newly recrystallized grains are not observed in the deformed annealed sample. Grain-shape analysis shows similar ratio of minor to major axis (~0.652) for undeformed sample and sample deformed to 4.87% axial strain. Comparing with consolidated sample, halite grains in annealed sample are more irregular-shaped with wider grain size range, which could lead to higher uncertainty in the ratio of minor to major axis. But it can still serve to suggest that grain flattening in annealed sample is insignificant.

Grain boundary opening is also evident in the deformed annealed samples (Figure 3.14). Two types of grain boundary openings are identified: some openings oriented at low angle to load axis preferentially open, few of which linked in the direction of differential load, their characteristics are similar to those of grain boundary opening-mode cracks observed in deformed consolidated samples; and others oriented at various angles to load axis and linked in the direction perpendicular to load axis. The former was produced during triaxial deformation while the latter during unloading of the sample at the end of the experiment. Intragranular cracking is also minor in deformed annealed samples. In the sample deformed to 4.87% axial strain, 7.7% of total grains contain intragranular cracks.

Under transmitted-light, high-density and spherical or tubular-shaped fluid inclusions are observed at closed grain boundaries of deformed annealed samples (Figure 3.13c, d). These fluid inclusions appear in all closed grain boundaries. Comparing with the undeformed sample, grain boundary fluid inclusions in annealed sample are less equant with more tubular shapes (compare Figure 3.11c, d with 3.13c, d).

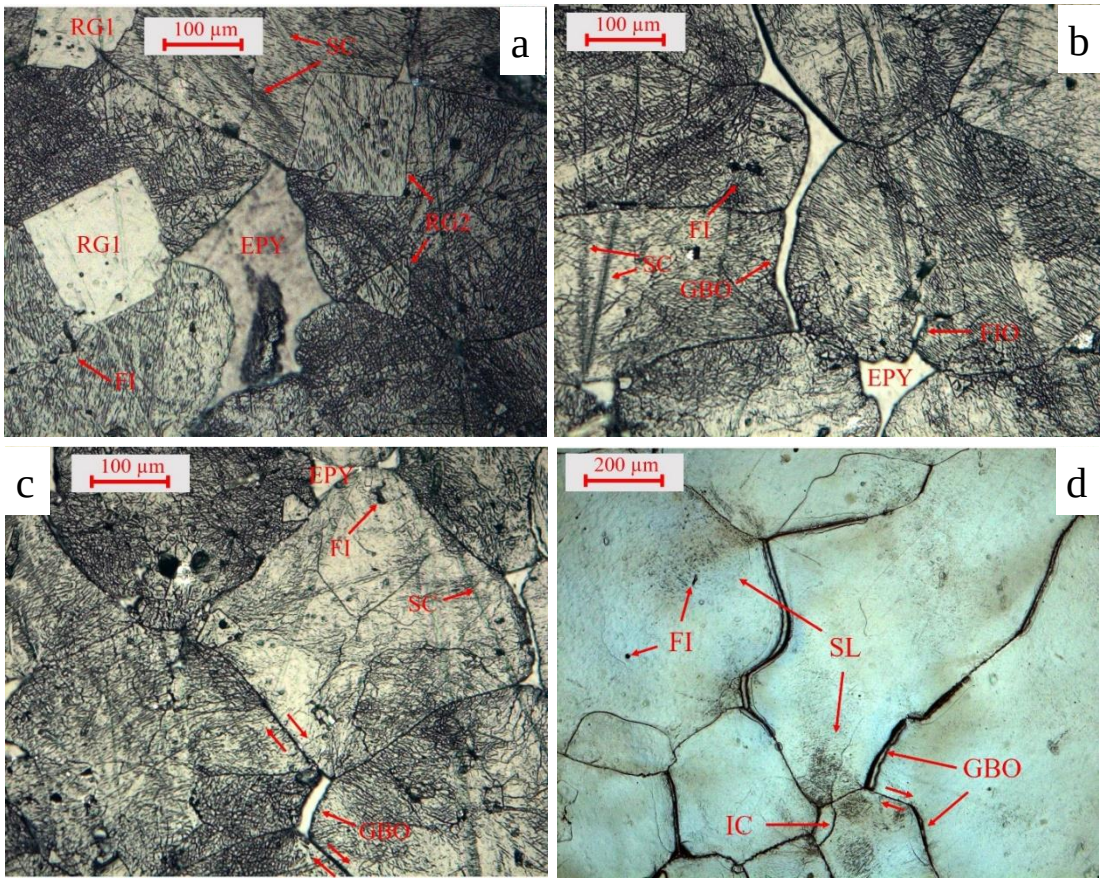

Figure 3.12 Reflected-light micrographs of (a) consolidated sample 61003 deformed to 2.77% axial strain, (b) and (c) consolidated sample 61123 deformed to 7.31% axial strain, and (d) annealed sample 070304 deformed to 4.87% axial strain. Two types of recrystallized euhedral grains are shown in (a): RG1 – recrystallized grains free of dislocation, RG2 – recrystallized grains containing slip lines. Paired arrows show inferred shear motion. GBO – grain boundary opening, EPY – epoxy (pore), SL – slip lines, IC – intragranular cracks, FI – fluid inclusions intersected the polished surface, SC – scratch resulted from polishing.

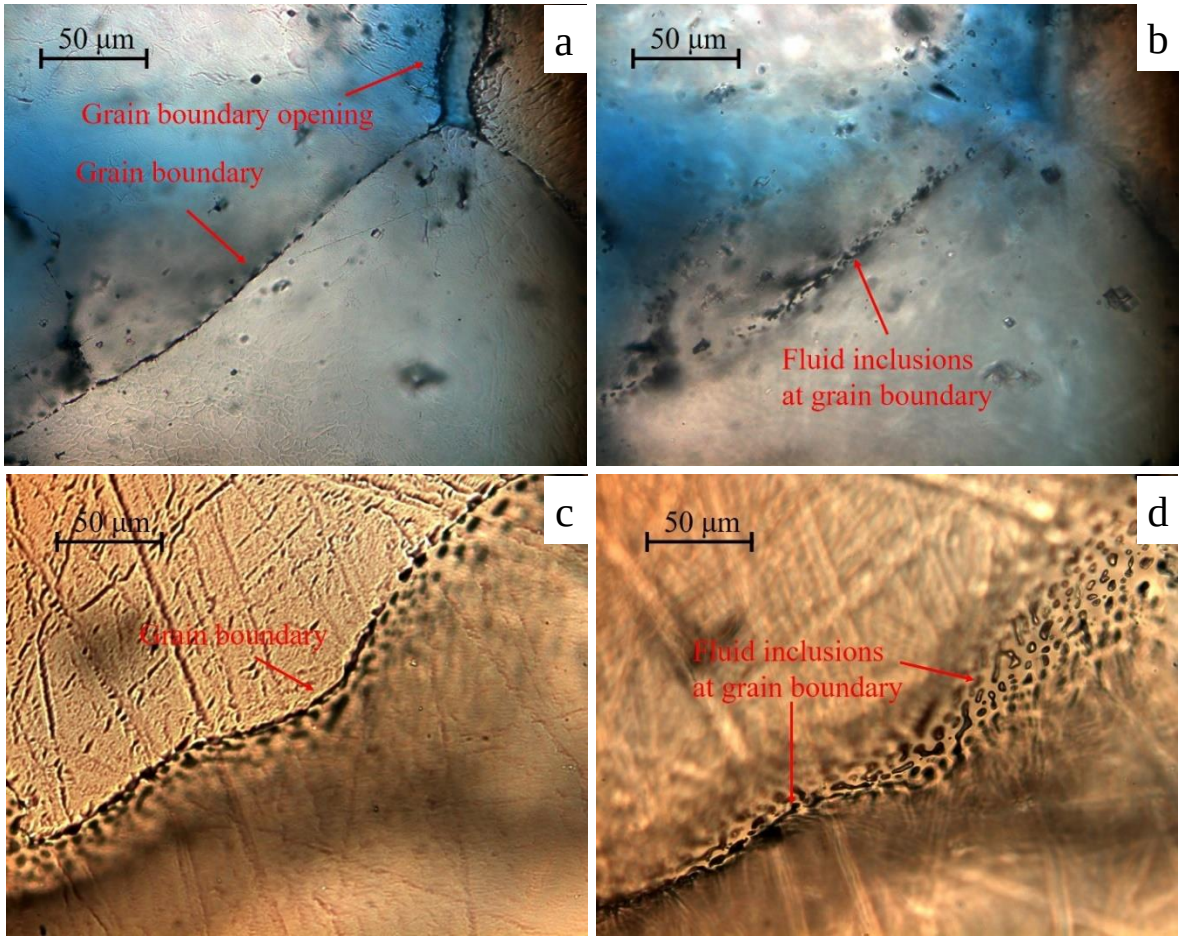

Figure 3.13 Transmitted-light micrographs of (a) and (b) consolidated sample 61123 deformed to 7.31% axial strain, (c) and (d) annealed sample 70304 deformed to 4.87% axial strain. (a) and (c) are focused on the polished surface, (b) and (d) are focused below the polished surfaces of (a) and (c) to reveal grain boundary structures. Load axis is vertical.

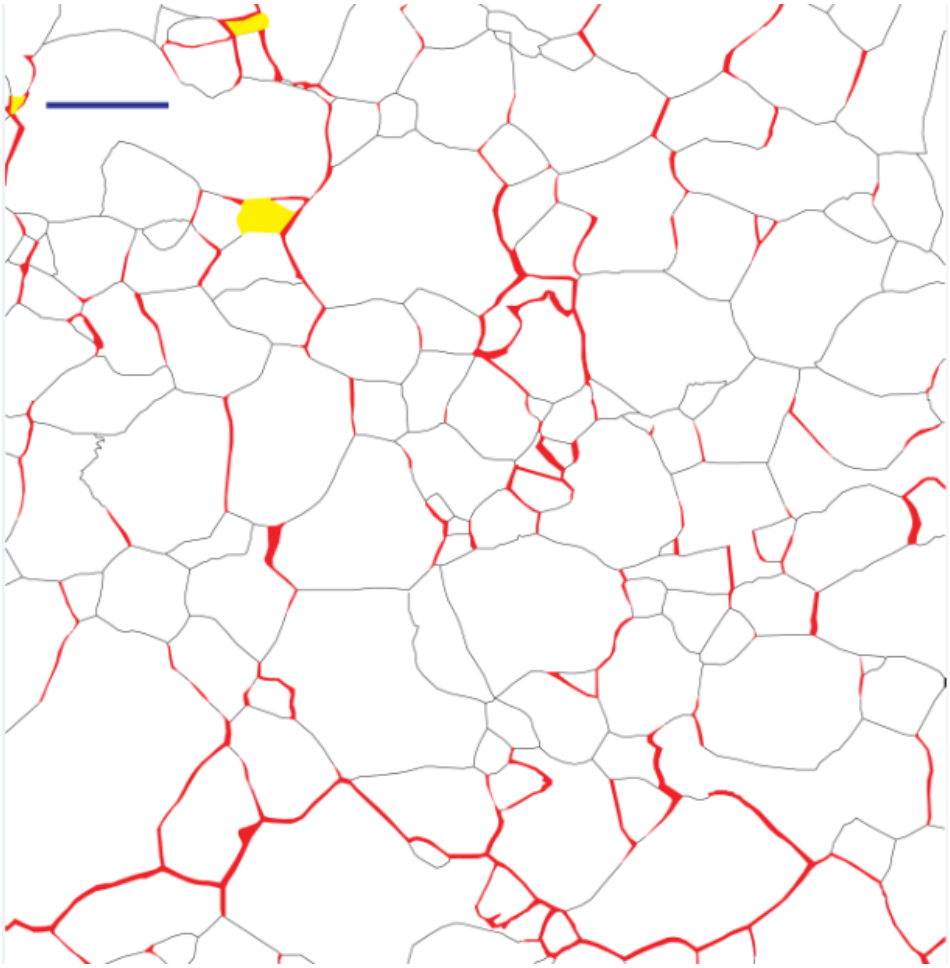

Figure 3.14 Stitched micrograph of annealed sample 70304 deformed to 4.87% axial strain. Halite grains (white) and pores (black) were manually traced. Missing grains (yellow) were caused by polishing. Scale bar (blue) represents 0.5 mm. Images were taken at sample center. Load axis is vertical. Note two sets of grain boundary openings: one set preferentially aligned to load axis (vertical direction) and distributed across the micrograph; the other set connected in the direction perpendicular to load axis (horizontal direction) and localized at the bottom of the micrograph.

3.4. Discussion

3.4.1. Deformation Mechanisms

In consolidated samples, intracrystalline plasticity was an active deformation mechanism during the cyclic triaxial compression tests. First, the density of wavy slip lines after triaxial deformation is increased beyond that seen in the grains deformed by consolidation only. Second, wavy slip lines are observed in the recrystallized grains formed at the end of consolidation, but are absent from the recrystallized grains formed at the end of triaxial deformation, also demonstrating dislocation motion during triaxial deformation. At room temperature, low confining pressure, and relatively fast strain rates, dislocation glide is the dominant intracrystalline plastic process in halite as recovery mechanisms are insufficient (Carter & Hansen, 1983; Senseny et al., 1992; Peach & Spiers, 1996). However, two lines of evidence indicate dislocation glide is a subordinate mechanism. During triaxial deformation, the stress-strain behavior showed nearly constant stress flow, but a characteristic behavior of deformation by dislocation glide is strain hardening. In addition, there is insignificant grain flattening or change in grain shape, even for samples deformed up to 7.31% axial strain which indicates little intracrystalline strain.

Brittle mechanisms of breaking and opening grain boundaries are significant during triaxial deformation of the consolidated samples. The opening-mode grain boundary cracking occurs at all stages of axial shortening and is recorded by increase in crack density and aperture with increased axial strain (Figure 2.11c). Moreover, opening cracks produce the porosity that explains the observed dilatancy throughout triaxial

deformation (Figure 3.2). Based on the geometry and distribution of those grain boundary openings, shear motion can be inferred in adjacent closed grain boundaries (Figure 3.12c). Here, we refer to the shear motion along grain boundaries with the descriptive term, grain boundary sliding, i.e. the mechanism of sliding is not implied. The wide-spread opening of grain boundaries is accommodated by grain boundary sliding at closed grain boundaries, which allows for only limited intragranular cracking and grain flattening. These suggest that grain boundaries are weak planes and susceptible to brittle deformation at test conditions. Sample fabrication through consolidation produced high dislocation density in halite grains. As the grains of consolidated samples were effectively hardened, subsequent triaxial deformation at low confining pressure and room temperature promoted brittle processes along grain boundaries. Bonding at grain boundaries was progressively damaged and broken with increasing inelastic deformation. Halite grains of broken boundaries rearrange through sliding and opening at as a primary way to accommodate the axial shortening. That is, the linked operation of grain boundary opening and sliding is the dominant deformation mechanism during triaxial deformation of the consolidated samples.

For the annealed samples, intracrystalline plasticity was an import deformation mechanism during the cyclic triaxial compression test. Annealing reduced dislocation density and produced samples of strain-free grains (Figure 3.10c). The triaxial deformation led to dislocation motion evidenced by the formation of wavy slip lines (Figure 3.12d). While consolidated sample flowed at nearly constant stress, annealed sample showed pronounced work hardening in the stress-strain curve (Figure 3.3), which

is consistent with significant dislocation glide. When dislocations move along the glide plane, they are often pinned by obstacles in crystal lattice, which increases resistance to further dislocation movement (Evans & Kohlstedt, 1995). Macroscopically, higher stress is required to continue dislocation movement which is often manifested as work hardening (Carter & Hansen, 1983; Senseny et al., 1992). Pronounced work hardening during triaxial deformation of the annealed sample suggests dislocation glide contributed more to the total deformation than in consolidated sample. However, insignificant grain flattening and low density of slip lines in the sample deformed to 4.87% axial strain indicate dislocation glide is unlikely the dominant deformation mechanism.

Brittle deformation in annealed samples also is important during the cyclic triaxial compression test. Pervasive grain boundary opening (Figure 3.14) and increase in sample volume (Figure 3.3) were also observed in annealed samples. While grain-scale plastic deformation by dislocation glide may have accommodated grain boundary opening, there are also evidence that grain boundary sliding facilitated the opening (Figure 3.12d). Minor intragranular cracking was observed in deformed annealed samples. Similar as the consolidated sample, these observations suggest grain boundaries are weak planes and susceptible to sliding and opening at the test conditions. Additionally, unloading-induced grain boundary cracking occurred in annealed sample evidenced by stress-strain response (Figure 3.5c) and microstructural observation (Figure 3.14). The unloading process may also have affected those load-axis oriented grain boundary openings. But considering the well-preserved preferential orientation, this effect is probably limited.

In annealed samples, strain partitioning between intracrystalline plastic and brittle processes changes with axial strain during the cyclic triaxial compression tests. With increasing inelastic strain, the slope of stress-strain curve decreases while the slope of volumetric strain-axial strain plot increases (Figure 3.3). This indicates that the hardening rate decreased while dilatancy rate increased. In the early stage of deformation, dislocation glide was easy in strain-free grains. With increasing dislocation density, further glide required higher stress which enhanced grain boundary sliding and opening at room temperature and low confinement. For the sample with a total axial strain of 4.87%, we estimate grain boundary sliding and opening is more dominant deformation mechanism than dislocation glide based on the observation of pronounced grain boundary cracking in microstructure, insignificant grain flattening and low density of slip lines. Using similar synthetic salt-rock sample and test conditions, grain boundary cracking and intracrystalline plasticity were also observed by (Peach & Spiers, 1996) and (Bourcier et al., 2013). While (Peach & Spiers, 1996) focused on the effect of microcracking on the transport properties of salt-rock, (Bourcier et al., 2013) quantified strain partitioning between grain boundary sliding and intracrystalline plasticity using surface markers and digital image correlation. Their study suggests grain boundary sliding accounts for more than 50% of total strain in fine-grained sample (grain size 0.03-0.08 mm), and intracrystalline plasticity accounts for more than 80% in coarse-grained sample (grain size 0.25-0.5 mm). Given that our sample has a wider grain size range (0.025-0.833 mm) and their fined- and coarse-grained samples were deformed to a

smaller total strain of ~3%, our interpretation of dominant deformation mechanism is in good agreement with their findings.

Both consolidated and annealed sample deformed in the semibrittle flow field with a combined and linked operation of brittle and crystal-plastic mechanisms: grain boundary cracking (i.e., grain boundary sliding and opening), intragranular cracking, and dislocation glide. While intragranular cracking is minor in both types of samples, the relative importance of the other two mechanisms are possibly quite different. In consolidated samples, grain boundary cracking is the dominant deformation mechanism for all axial strains achieved. In annealed samples, strain partitioning between grain boundary cracking and dislocation glide is dependent on total inelastic strain; grain boundary cracking is enhanced with increasing strain relative to dislocation glide because of work-hardening associated with glide. In fact, the consolidated sample may be viewed as the final state of the annealed sample deformed at rates and temperatures where recovery processes are relatively slow and unimportant. When dislocation density in annealed sample becomes high enough after sufficient inelastic deformation, dislocation glide would be largely inhibited while grain boundary cracking and sliding becomes dominant, which is a state of deformation processes in the consolidated samples during semibrittle flow.

3.4.2. Accommodation Mechanisms for Grain Boundary Sliding

In brittle field, grain boundaries may slide past each other by frictional processes (Sibson, 1986). For plastic deformation, grain boundary sliding can be accommodated by intracrystalline plasticity or diffusion (Raj & Ashby, 1971). At room temperature, low

confinement, and high strain rates, salt-rock predominantly deforms by friction (Chester, 1988; Shimamoto, 1986). Therefore, friction is proposed as the primary accommodation mechanism for grain boundary sliding during the semibrittle flow that achieves permanent strain in the large-load cycles. Microstructural observation of deformed consolidated samples reveals that sliding grain boundaries have an average orientation of 50.4° relative to differential load axis. For a flow strength (differential stress) of 40 MPa and a confining pressure of 1 MPa, normal and shear stresses acting on sliding grain boundaries are estimated to be 24.8 MPa and 19.6 MPa, respectively, based on the following equations (Chester, 1988):

$$\sigma_n = P_c + \Delta\sigma \, sin^2\theta \qquad \text{Equation 3.1}$$

$$\tau = \frac{1}{2} \, \Delta\sigma \, sin2\theta \qquad \text{Equation 3.2}$$

where σ_n and τ are normal and shear stresses acting on sliding grain boundaries, Pc is confining pressure, $\Delta\sigma$ is differential stress, and θ is average orientation of sliding grain boundaries with respect to differential load axis. In friction experiments on halite gouge, this stress condition activates frictional sliding by cataclastic faulting (Chester, 1988, 1989; Shimamoto, 1986). In annealed samples, the average orientation of sliding grain boundaries is 53.4° relative to differential load axis, similar to that of consolidated samples. Applying the same analysis, the stress condition of sliding grain boundaries also favors brittle friction.

Our consolidated samples contained a water content of ~300 ppm (weight $H_2O/10^6$ NaCl) (Table 3.2). For fine-grained salt-rocks (0.08-2 mm), this water content is sufficient to invoke fluid-assisted grain boundary processes such as grain boundary

migration recrystallization and solution-transfer creep (Spiers & Carter, 1996; Watanabe & Peach, 2002; Ter Heege et al., 2005). This is consistent with the stress relaxation behavior at low strain rates with a stress exponent of nearly one (Figure 3.9). Therefore, it is likely that grain boundary sliding was accommodated by fluid-assisted diffusion at low strain rates once bonds were broken and fluids could be distributed along the sliding boundaries. The fluid-assisted diffusional process is likely highly local and serves as an effective accommodation mechanism for grain boundary sliding (Raj & Ashby, 1971). Some small load cycles were conducted at a strain rate of 3×10^{-7} s^{-1}, close to the transitional strain rate ($\sim2\times10^{-8}$ s^{-1}) in the stress relaxation behavior. Fluid-assisted diffusion could be an important accommodation mechanism for grain boundary sliding in addition to frictional process. The water content of our annealed samples was ~5 ppm (weight $H_2O/10^6$ NaCl) (Table 3.2) and comparable with the "dry samples" of (Watanabe & Peach, 2002), which deform in the absence of fluid-assisted grain boundary processes. Therefore, grain boundary sliding accommodated by fluid-assisted diffusion was negligible in annealed sample. This interpretation is supported by the stress relaxation behavior. Differential stress during relaxation test was effectively maintained down to very low strain rate, resulting in a high stress exponent of 25.4 (Figure 3.9). Friction in halite at very dry conditions is found to have a pronounced decrease in rate-dependence of strength (Bos & Spiers, 2002) and therefore leads to a high stress exponent. The deformation regime with a stress exponent of one was not observed in annealed sample suggesting the absence of fluid-assisted grain boundary processes.

The rate-dependence of grain boundary sliding is clearly different for consolidated and annealed samples as shown by the stress relaxation tests (Figure 3.9). In both samples, stress relaxation tests started from the stress levels of semibrittle flow where frictional sliding of grain boundaries was operative. At high strain rates, the stress exponent of wet consolidated samples is much lower than that of dry annealed samples. This suggests that the solution-transfer processes are likely also important in frictional grain boundary sliding of wet consolidated samples, leading to a more pronounced rate-dependence. At low strain rates, the rate-dependence in wet consolidated samples is dominated by solution-transfer creep at grain boundaries (Bos & Spiers, 2002; Pennock et al., 2006), which is absent in dry annealed samples.

3.4.3. Grain Boundary Behavior and Elasticity

The changes in the elastic properties by triaxial deformation of both consolidated and annealed samples displayed in the small-load cycles are either caused by changes in pore space, grain interior or at grain boundaries. The observation that elastic properties recovered significantly after sufficiently long holds at confinement of 1 MPa or less suggests elastic behavior was not controlled by intragranular deformation or the porosity. Before and after hold, no appreciable change was observed in grain interior such as the density and distribution of dislocation and intragranular cracks and pores. However, there was an important change at grain boundaries, specifically healing and rebonding of grain boundaries damaged during the semibrittle flow.

In deformed samples, grain boundaries can be classified into two groups based on whether they open under differential load. Grain boundaries that open and create new

porosity are preferentially aligned to load axis (Figure 3.15). Grain boundaries that remain closed can be further divided into two subgroups based on whether sliding can occur. Those oriented at moderate angles to load axis are capable of sliding during differential loading, while those oriented at very high or very low angles are not. The changes in elastic properties are found to be well correlated with the quality of bonding of the closed grain boundaries oriented appropriately for sliding and linked to boundaries oriented for opening.

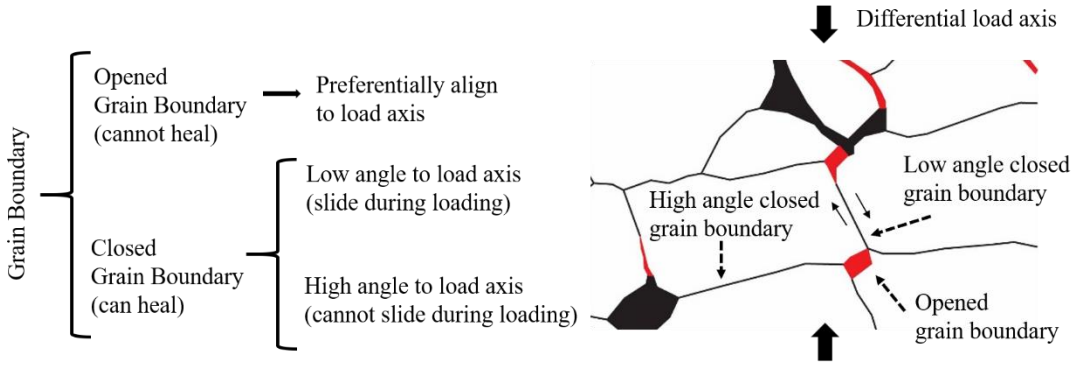

Figure 3.15 Left: classification of grain boundaries in deformed samples. Right: microstructural examples of different grain boundaries in deformed samples. Halite grains – white, pores – black, opening-mode microcracks – red, shear motion – paired arrows.

For both consolidated and annealed samples, Young's modulus and Poisson's ratio measured during small-load cycles decreased and increased, respectively, with increasing inelastic deformation by semibrittle flow. Both elastic properties recovered to nearly original values (i.e., at zero axial strain) after the sample was allowed to heal. Healing of closed grain boundaries in dry annealed samples was much slower even under load than in wet consolidated samples, suggesting healing is a fluid-assisted

process. Microstructural observation of healed boundaries that had slid (evinced by linkage to opened boundaries) showed dense arrays of small fluid inclusions characteristic of crack-healing (Figure 3.13a, b and 21; Roedder, 1984). Opened grain boundaries remained open and do not show evidence of rebonding (Figure 3.12b, c). Healed boundaries are restrengthened, so they do not slip at low loads. With resumed differential loading to invoke semibrittle flow (large-load cycles), the appropriately oriented boundaries are rebroken and frictional sliding ensues. With continued semibrittle flow, more boundaries are activated leading to progressive degradation of elastic properties (Figure 3.6 and 7). Collectively, these observations indicate that the changes in elastic properties are largely controlled by the microprocesses of sliding on the closed, inclined grain boundaries.

For consolidated sample, elastic properties exhibited rate-dependent behavior: lower strain rate led to lower values and greater hysteresis. The rate-dependence increased with increasing inelastic axial strain almost disappeared upon healing (Figure 3.6). These are caused by the fluid-assisted diffusional processes in sliding grain boundaries. In the small-load cycles, more pronounced diffusion at low strain rates leads to lower sliding resistance and therefore more sliding to reach similar stress level. In a stress-strain plot, this is expressed as lower stiffness (more stress is relaxed) and higher hysteresis (more work is done) (Figure 3.4). Increasing semibrittle flow at large-load cycles activated more sliding grain boundaries, which in turn led to more pronounced hysteresis, rate-dependence, and anelasticity in small-load cycles. The sliding of grain boundaries upon imposing small loads and reverse sliding during unloading cause axial

strain to be fully recoverable, despite underlying inelastic micromechanisms (Lawn & Marshall, 1998). These phenomena were absent in annealed samples due to insufficient water at grain boundaries.

3.4.4. Implications

In salt caverns, similar conditions of low temperature and confining pressure may be encountered at cavern walls (Bérest, 2013). In excavated salt caverns, halite grains at walls may increase in dislocation density due to construction related deformation, whereas in solution mined caverns dislocation density in halite grains at walls should be as low as in non-disturbed natural salt (Fokker, 1995). In gas storage caverns operated to satisfy the seasonal or emergency needs, the cyclic loading associated with changes in gas volume may be analogous to our experiments (Bérest, 2013). Our study suggests that inelastic deformation around salt cavern walls leads to development of grain boundary microcracking. Linking of preferentially opened grain boundaries with shear slipping boundaries can produce linked arrays that, with stress cycling, could cause instability of cavern wall such as spalling and block fall. When modeling the behavior of salt caverns, the effects of grain boundary behavior on elastic properties should be considered as they may lead to either pronounced degradation or recovery of elastic properties. Additionally, as water is almost always present in natural salt rocks (Roedder, 1984), elastic deformation may be dependent on loading rate with pronounced hysteresis at low strain rates. For gas caverns, avoidance of large stress cycling could minimize breakage and activation of frictional sliding with dilatancy from associated opening boundaries, and employing holds to allow cracked grain boundary healing could help preserve the

integrity of cavern walls. These phenomena will affect the mechanical behavior and sealing capability of salt caverns.

The brittle-ductile transition in the lithosphere is characterized by semibrittle deformation with a mixed mode of brittle frictional, crystal-plastic, and diffusional processes (e.g., Brace & Kohlstedt, 1980; Kirby, 1980; Kohlstedt et al., 1995). In seismogenic zones of the crust, the brittle-ductile transition corresponds to the depth limit of shallow crustal seismicity and experiences pronounced stress cycling (Brace & Kohlstedt, 1980; Sibson, 1983). In deep crust, there are also evidences of elevated pore pressure which is thought to enhance brittle deformation despite high stress and temperature conditions (Beeler et al., 2016). During inter-seismic period, the upper part of brittle-ductile transition deforms dominantly by brittle friction and accumulate stress, whereas the lower part deforms viscously in steady state (Sibson, 1986). Viewing salt as rock analogue material, the consolidated samples may represent the shallower brittle frictional rock end member of the semibrittle regime, and the annealed samples may represent the deeper viscously creeping rock end member. Earthquakes rupture downward into the semibrittle zone, effectively creating large displacement and concentrated increase in stress and strain rates (Strehlau, 1986), which may be qualitatively analogous to the large-load cycles employed in this study. Our results indicate that the pronounced stress cycling by earthquakes may cause the healed or recrystallized rocks to yield and undergo semibrittle flow, activating grain boundaries and distributing water. Post-seismic deformation may involve time-dependent grain boundary sliding that effectively relax increased stress. As stress is reduced, rocks may

eventually heal at grain boundaries at shallow depths or transition back to steady state creep with recrystallization before next stress cycle. This is a rather simplified analogy to natural rock deformation by ignoring many factors such as rock composition and heterogeneity. However, it serves to illustrate that at semibrittle conditions grain boundary processes maybe important in controlling rheological behavior of rock.

3.5. Conclusions

We conducted cyclic triaxial compression and stress relaxation tests on two types of synthetic salt-rocks with contrasting grain structures at room temperature and a confining pressure of 1 MPa. The analyses of mechanical data and characterization of microstructures lead to the following conclusions:

1. The porous, work-hardened consolidated samples deform by semibrittle flow, which involves predominant grain boundary sliding and opening accompanied by minor intragranular cracking and dislocation glide. The near-zero porosity, fully annealed samples deform predominantly by dislocation glide and grain boundary sliding and opening accompanied by minor intragranular cracking. The contribution to total strain from grain boundary sliding and opening increases with increasing strain, as dislocation glide requires increasing higher stress for continued dislocation motion (work-hardening effect).
2. Grain boundary sliding in consolidated sample is predominantly a frictional process at high strain rates. At low strain rates, fluid-assisted diffusion becomes more important in accommodating sliding at grain boundaries. The less pronounced grain

boundary sliding in annealed sample is also primarily accommodated by friction. Fluid-assisted diffusion is insignificant because of low water content in sample.

3. Young's modulus and Poisson's ratio are largely controlled by the behavior of closed grain boundaries that slide. Debonding and sliding at grain boundaries during semibrittle flow at high stress lead to degradation of elastic properties. Sufficient rebonding of damaged closed grain boundaries recovers degraded elastic properties to nearly undamaged values. At low strain rates, sufficient fluid at grain boundaries enhances fluid-assisted diffusional accommodation for grain boundary sliding, which causes elastic properties and hysteresis to be strain-rate dependent.

4. EXPERIMENTAL TEST OF THE EFFECTIVE STRESS LAW FOR SEMIBRITTLE FLOW IN SYNTHETIC SALT-ROCK

4.1. Introduction

It is important to consider effective stress when describing the mechanical behavior of rock (Beeler et al., 2016; Bishop & Skinner, 1977; Brace & Martin, 1968; Handin et al., 1963; Kohlstedt et al., 1995; Noda & Takahashi, 2016; Terzaghi, 1923). When brittle, frictional behavior dominates, the effective stress is determined as the difference between the externally applied stress and the pore fluid pressure, according to Terzaghi's effective stress law (Terzaghi, 1923). The physical basis of the Terzaghi's effective stress law is often interpreted based on the force balance at grain contacts, which assumes that the effective stress is controlled by the true area of grain contact that is sufficiently tight to restrict pore fluid from permeating into the contact. At low pressure and temperature, the true area of grain contact is vanishingly small and therefore pore pressure efficiently pushes against the externally applied stress. This interpretation is supported by both experimental and theoretical work (Beeler et al., 2016; Brace & Martin, 1968; Handin et al., 1963; Skempton, 1960). On the other hand, at higher stress and temperature conditions, rock deformation becomes more distributed and is achieved by a combination of brittle and crystal-plastic mechanisms, and the true area of grain contact can increase significantly from crystal-plastic deformation. Under these circumstances, it is not clear if the effective stress is controlled by the true area of

grain contact. In general, current laboratory data are insufficient to describe the effective stress states when true area of grain contact is large (Beeler et al., 2016).

Determination of the effective stress for conditions promoting large true area of grain contact is necessary for many rock mechanics problems. For example, salt-rock has been used as host rock for energy storage and waste disposal across the world. At salt cavern walls, the temperature and pressure conditions often activate significant crystal-plastic deformation in addition to microcracking (Bérest, 2013; Peach & Spiers, 1996; Urai et al., 2008). Consequently, stability analyses of salt-rock storage should utilize an effective stress relationship applicable for mixed-mode of brittle and crystal-plastic deformation. The effective stress law also is important in earthquake mechanics analyses. The highest strengths expected in the lithosphere are found in the brittle-plastic transition where some mineral phases respond to applied loads by fracturing and frictional sliding, while other phases deform by crystal plasticity and other high temperature deformation mechanisms (Brace & Kohlstedt, 1980; Sibson, 1983). An effective stress law for mixed-mode of brittle and plastic deformation is required to determine stress states that are critical for the understanding of earthquake nucleation at the base of the seismogenic zone, propagation of ruptures downward into the ductile crust, deep episodic tremor and slip, and post-seismic creep.

In this section, we report an experimental test of proposed effective stress laws that predict strength and volumetric strain during inelastic deformation. We choose halite as our testing material because it has low yield strength and deforms easily through crystal-plasticity, even at room temperature and laboratory rates (Carter &

Heard, 1970). This property allows us to test the effective stress relationship for conditions that true area of grain contact is a large fraction of the apparent area due to intracrystalline-plastic deformation. We conducted both triaxial compression and isostatic consolidation tests on synthetic salt-rock samples with load-paths designed to amply the change of effective stress states caused by a non-unity effective stress coefficient. In triaxial compression tests, confining and pore pressures are cycled while keeping their difference constant. In isostatic consolidation tests, volumetric strain is measured at varying pore pressures. Microstructures of key samples before and after mechanical tests are examined using reflected-light microscopy to determine deformation mechanisms.

4.2. Background

Mechanical behavior of rock materials (e.g., shear failure in intact rock and preexisting fracture, volumetric strain) are a function of externally applied stress and pore fluid pressure:

$$\sigma_s(or\ \varepsilon_v\ \dots) = f\big(\sigma_{ij}, Pp, T \dots\big), \qquad \text{Equation 4.1}$$

where σ_s is shear strength, ε_v is volumetric strain, σ_{ij} is external stress, Pp is pore fluid pressure, T is temperature, and f is function. The effects of external stress and pore fluid pressure are often grouped together and represented by the effective stress (e.g., Skempton, 1960):

$$\sigma_{ij}^{e} = g\big(\sigma_{ij}, Pp\big), \qquad \text{Equation 4.2}$$

where σ_{ij}^{e} is effective stress, g is function. The functional format of the effective stress relationship may be different for different mechanical behavior and can be generalized according to the following equation:

$$\sigma_{ij}^{e} = \sigma_{ij} - \delta_{ij}\alpha Pp, \qquad \text{Equation 4.3}$$

where α is effective stress coefficient and $0 \leq \alpha \leq 1$, δ_{ij} is Kronecker delta (e.g., Skempton, 1960; Nur and Byerlee, 1971). In the following, we simplify the equations by using σ for σ_{ij} and σ^{e} for σ_{ij}^{e}.

Terzaghi (1923) first introduced the concept of effective stress from his soil mechanics experiments by

$$\sigma^{e} = \sigma - Pp, \qquad \text{Equation 4.4}$$

which indicates that the effective stress coefficient is equal to unity. Following Terzaghi's (1923) work, several different forms of the effective stress law have been proposed. Based on the contact-scale force balance, the effective stress relationship for shear strength can be derived as (e.g., Skempton, 1960; Bishop and Skinner, 1977, Beeler et al., 2016)

$$\sigma^{e} = \sigma - \left(1 - \frac{A_s}{A}\right) Pp, \qquad \text{Equation 4.5}$$

where A_s is true grain contact area, specifically, it refers to the grain contact area that is tight enough to restrict pore fluid from permeating into the contact, A is total (or apparent) area of interest. For granular material that follows Coulomb's failure criterion, Skempton (1960) derived the effective stress relationship:

$$\sigma^{e} = \sigma - \left(1 - \frac{A_s}{A}\frac{tan\psi}{tan\phi'}\right) Pp, \qquad \text{Equation 4.6}$$

where ψ is angle of intrinsic friction of the grains comprising of the rock, ϕ' is angle of intrinsic friction of the rock. For volumetric strain, the effective stress can be also determined from compressibility (e.g., Skempton, 1960; Nur & Byerlee, 1971):

$$\sigma^e = \sigma - \left(1 - \frac{C_s}{C}\right) Pp, \qquad \text{Equation 4.7}$$

where C_s is compressibility of the solids comprising of the rock, C is compressibility of the rock. For frictional sliding, Beeler et al. (2016) extended Equation 4.5 by incorporating material yield strength:

$$\sigma^e = \begin{cases} \frac{\sigma - Pp}{\left(1 - \frac{Pp}{\chi \sigma_y}\right)} & if\ \chi\sigma_y > \sigma \\ \sigma & if\ \chi\sigma_y \leq \sigma \end{cases},$$

$$\chi = \frac{\cos\left(tan^{-1}\mu\right)}{2\mu}, \qquad \text{Equation 4.8}$$

and σ_y is grain yield strength, μ is the coefficient of friction.

To apply any of these effective stress laws, an apparent and important premise is that pore fluid pressure needs to be transmitted fully throughout the rock body, so that externally measured pore pressure reflects the pore fluid pressure within the rock. This could present problems for experiments using low-porosity rocks. Handin et al. (1963) noted in their experiments that low-porosity marble and limestone showed pronounced deviation from Terzaghi's effective stress law. Brace and Martin (1968) systematically investigated the role of loading rate, rock permeability, and pore fluid viscosity on effective stress and demonstrated that dilatancy hardening occurred when fluid transmission and equilibration within pores did not keep pace with deformation.

Terzaghi's effective stress relationship (Equation 4.4) may be considered as a special case of Equations 4.5-4.8 when the true contact area is vanishingly small in soil and porous rock at low mean stress and low temperature (Dieterich & Kilgore, 1994, 1996). For the case of vanishingly small true contact area, pore fluid pressure almost fully opposes the external stress and therefore α is nearly one. Although Terzaghi's effective stress relationship provides sufficient accuracy for most engineering purposes in brittle, frictional rock masses, the exact expression for the effective stress coefficient has been a subject of debate.

Hubbert & Rubey (1959) argued that the effective stress coefficient is always equal to one through analytical treatment of the effective stress state. They argued that pore pressure does not terminate at grain contacts and is continuous throughout the entire space occupied by the solid and fluid. Laubscher (1960) disagreed with Hubbert and Rubey (1959) view by pointing out that the principle used in their derivation is not applicable to porous rock underground.

Skempton (1960) compared experimental data relating the volumetric strain and shear strength to the ratio of true contact area to total area. For volumetric strain, Skempton (1960) used experimental data from Laughton (1955) triaxial consolidation of lead shot. The true area of the grain contacts was estimated from microscopic observation of particles after loading. For shear strength, Skempton (1960) used both the jacketed and unjacketed triaxial test data on Marble and Solenhofen limestone for the estimation of the ratio of true contact area to total area. In both cases, Skempton (1960)

analysis suggested that both Terzaghi's effective stress formulation and Equation 4.6 and 4.7 fit experimental data reasonably well; Equation 4.5 does not fit the data.

Bishop and Skinner (1977) re-wrote Equation 4.3 as:

$$\sigma^e = (\sigma - Pp) + (1 - \alpha)Pp, \qquad \text{Equation 4.9}$$

and designed experiments to investigate the effect of the second term on the right side of Equation 4.9. In their experiments, the difference between confining pressure and pore pressure was kept small, but the absolute magnitude of pore pressure used was varied between small and large values. When the variation of pore pressure is large enough, then the second term on the right side of Equation 4.9 leads to first-order change in effective stress even if the true contact area is small. The shear strength of granular samples was monitored to track any variation in strength as pore pressure was varied. Even with high-precision measurements and a pronounced increase in contact area, no observable change in shear strength was obtained, which suggests that the effective stress coefficient is equal to one. Notably, the experiments by Bishop and Skinner (1977) do not support the effective stress formulation of Skempton (1960) (Equation 4.6).

Using available data in the literature and their development of the effective stress relationship (Equation 4.8), Beeler et al. (2016) constructed a strength profile of the Earth's lithosphere incorporating a decreasing effective stress coefficient with depth. In this model, the transitional field of semibrittle deformation was omitted and a sharp peak in strength occurs at the brittle-plastic transition. However, Noda and Takahashi (2016) demonstrated through their triaxial shear experiments on halite gouge that the transition is rather smooth and the effective stress coefficient is always equal to one.

Nearly one hundred years have passed since Terzaghi's classic work in 1923. Our understanding of the physical basis and exact form of the effective stress law is still limited due to insufficient experimental data (Beeler et al., 2016). How the effective stress coefficient is affected by the true area of grain contact remains unclear and continues to be a debatable subject. Consequently, there still is a strong need for additional experiments to further elucidate this rather important topic in rock mechanics.

4.3. Methods

4.3.1. Sample Preparation

Synthetic salt-rock samples were fabricated using high-purity (99 wt.%), reagent-grade granular salt. The granular salt was sieved to separate grains 0.3-0.355 mm diameter, which were used to produce cylindrical, porous-granular salt-rock samples by uniaxial consolidation following the methods of Section 2.2.2 and 2.2.3 (Ding et al., 2016). We used same consolidation conditions for all samples except for the maximum axial stress applied; two stress magnitudes were employed to produce samples with two different porosities (Table 4.1). Fabricated samples of 5.4±0.4% porosity were used for triaxial compression tests and those of 19.4±0.6% porosity were used for isostatic consolidation tests. Herein, the two types of samples are referred to as low- and high-porosity samples.

Table 4.1 Fabrication conditions for two types of synthetic salt-rock samples used in this study

	Low-porosity sample	High-porosity sample
Consolidation loading rate (mm/s)	0.34	0.34
Consolidation temperature (°C)	150	150
Consolidation maximum axial stress (MPa)	75	25
Bulk porosity (%)	5.4±0.4	19.4±0.6
Test used	triaxial compression	isostatic consolidation

In triaxial compression, the low-porosity samples deform at a nearly constant differential stress at a confining pressure of 1 MPa and room temperature. Mechanical data and microstructural observations indicate the dominant deformation mechanisms at these conditions are grain boundary opening and sliding accompanied by minor intracrystalline plasticity and intragranular cracking. Sliding along grain boundaries is dominantly frictional at normal laboratory rates of strain, but at low strain rates is achieved by fluid-assisted diffusion resulting in a viscous response (Section 3.4). The constant flow strength, mixed mode deformation mechanisms, and low yield stress of halite provide an opportunity to test the effective stress law for large true area of grain contact.

We chose to use high-porosity samples of ~19.4% porosity in our consolidation tests for two reasons: 1) the starting porosity is high enough to allow sufficient pore volume reduction and testing effective stress using stepping tests on a single sample; 2) the starting porosity is low enough that samples do not disaggregate during handling,

and can be conveniently instrumented in our triaxial apparatus without damage during the sample preparation process.

The mechanical behavior of salt is strongly influenced by water (e.g., Watanabe and Peach, 2002), so all samples used in this study were prepared, stored and sectioned in a controlled low-humidity environment (RH < 17%) to maintain similar water content (Section 2.2.2, Ding et al., 2016). The low-humidity environment is especially critical for preparing high-quality petrographic sections of salt samples.

4.3.2. Mechanical Experiments

Two types of mechanical tests were used to investigate the effective stress law for the two different sample porosities (Table 4.2). Triaxial compression tests on the low-porosity samples involved cyclic loading through yield and flow with changes in both confining and pore pressures to document the flow strength for different absolute stress. Three-dimensional consolidation by isostatic stressing of high-porosity samples involved varying pore pressures to evaluate how effective stress influences volumetric strain.

Table 4.2 Samples and experiments

Sample No.	Initial Porosity (%)	Test performed	Confining pressure (MPa)	Pore pressure (MPa)	Pore fluid
70516[a]	5.50	n/a	n/a	n/a	none
61123	5.38	triaxial compression	1	0	none
80711	5.42	triaxial compression	2-5	1	silicone oil
80725[a]	5.32	triaxial compression	2-121	1-120	silicone oil
80809[a]	5.25	triaxial compression	2-36	1-35	argon gas
60421[a]	19.33	n/a	n/a	n/a	none
80831[a]	19.63	consolidation	1.5-140	0.5-30.5	silicone oil
81124	19.22	consolidation	31.5-140.5	30.5	silicone oil

[a]Samples were prepared for petrographic sections to study microstructures.

4.3.2.1. Triaxial Compression Experiments

According to Equation 4.9, the role of the effective stress coefficient in affecting the effective stress state can be amplified by cycling both confining and pore pressures while maintaining a constant and low magnitude difference (Bishop and Skinner,1977). Applying this concept, we designed a load path for triaxial compression tests that involves cycling both confining and pore pressures (Figure 4.1, Table 4.3). In previous triaxial compression tests on low-porosity samples at dry, room temperature, and drained conditions (Section 3.2.3), a confining pressure of 1 MPa was used. Therefore, in the present tests a difference between confining and pore pressures was maintained at 1 MPa. Experiments were started at low absolute confining and pore pressures and samples were shortened to approximately 3% axial strain to establish constant flow strength. Then the sample was fully unloaded (differential stress reduced to zero) after which confining and pore pressures were increased progressively while maintaining a constant difference of 1 MPa. Upon reaching target pressures, differential loading was resumed until new flow strength was well established. Then, the sample was again fully unloaded to allow pressures to be progressively reduced back to the starting values in the first load cycle. Differential loading was again resumed until new steady-state flow strength was reached. The flow strength at these three cycles were compared to infer if there was change in flow strength, and thus of effective stress, due to non-unity effective stress coefficient. Conducting cyclic triaxial compression tests on the same sample eliminates uncertainty in absolute flow strength caused by sample variation and thus

allows a more accurate test of the effective stress law. All tests were performed at room temperature and an axial strain rate of 3×10^{-6} s^{-1}.

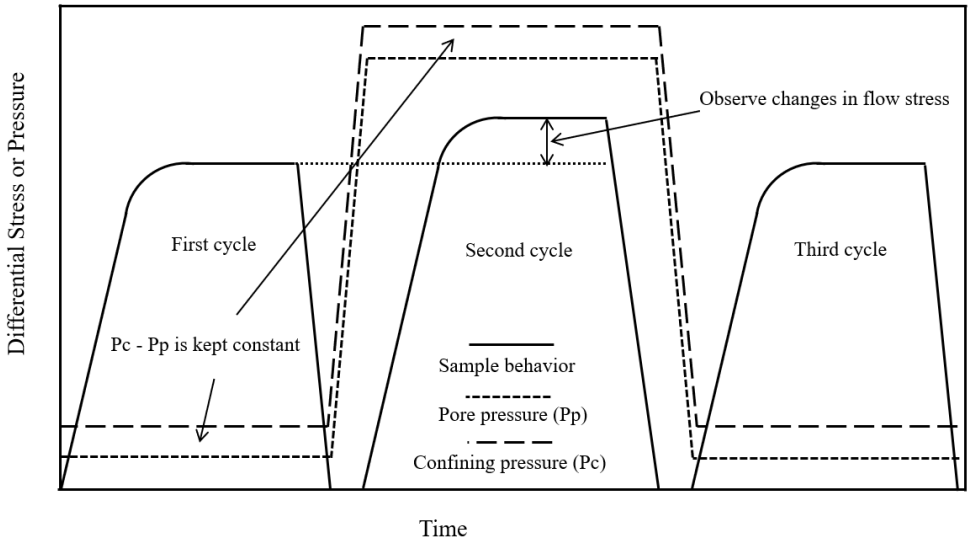

Figure 4.1 Schematic of load paths used in triaxial compression tests. Confining pressure (Pc) and pore pressure (Pp) were cycled while maintaining their difference constant.

Table 4.3 Confining and pore pressures used in triaxial compression tests

	First and Third Cycles			Second Cycle		
Pore Fluid	Pc (MPa)	Pp (MPa)	Pc-Pp (MPa)	Pc (MPa)	Pp (MPa)	Pc-Pp (MPa)
Silicone oil	2	1	1	121	120	1
Argon gas	2	1	36	35	2	1

Both liquid and gas phases were used as pore fluids to investigate if the pore medium would affect effective stress. For the liquid, pure silicone oil with a viscosity of 5 centistrokes was used. With silicone oil, confining and pore pressures could be varied by more than two orders of magnitude (Table 4.3). For the gas, argon of 99.998% purity with a water content of 3 ppm was used; the water content is much lower than that in our

sample (~300 ppm, weight $H_2O/10^6$ NaCl, Section 3.2.2) so that the change in the water content of the samples is negligible. For tests with argon gas, the confining and pore pressures could be varied by about 1.4 orders of magnitude (Table 4.3). The maximum pore pressure was limited by the bottle pressure containing the gas.

All samples were jacketed with heat-shrinkable polyolefin (Figure 4.2) to isolate pore fluid and confining fluid. A steel spacer is placed between the sample and load piston that connects to pore pressure system. The spacer is machined with evenly distributed flow channels and holes to enhance pore fluid access to the sample. We placed very thin (50 μm) Teflon sheets at the two sample ends to reduce friction with the piston and spacer, which promotes more uniform deformation along the axis of the sample and therefore reduces sample barreling.

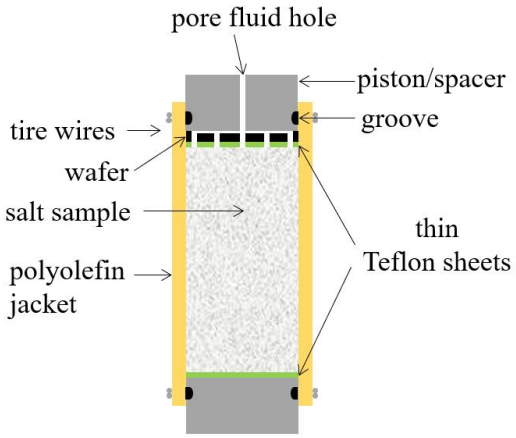

Figure 4.2 Schematic of sample assembly used in both triaxial compression and isostatic consolidation tests.

For triaxial tests using silicone oil as the pore fluid medium, samples were saturated in silicone oil under vacuum for more than 12 hours. During sample instrumentation, special care was taken to minimize fluid loss from sample. The pore pressure line was filled with silicone oil to minimize air bubbles in the pore pressure system. Once installed in the triaxial apparatus, samples were confined by the starting confining pressure of 2 MPa and starting pore pressure of 1 MPa. These pressures were allowed to reach full equilibrium before differential loading. For triaxial tests using argon gas as the pore fluid medium, samples were placed in the triaxial apparatus and then injected with gas to achieve the same starting confining and pore pressures and fully stabilized pressures.

The triaxial apparatus has an internal force gauge to measure the differential load, which is unaffected by friction between loading piston and sealing stack. The zero-point offset of the force gauge depends on confining pressure, so confining pressures were changed only when the sample was fully unloaded, i.e., zero differential load. Therefore, the change of zero-point offset was directly measured during pressure changes such that the absolute differential stress could be measured directly. Change of sample length by deformation was measured using a DCDT mounted external to the vessel, so a correction for elastic distortion of the apparatus was applied to measurements to determine the axial strain of the sample at constant confining pressures. When confining pressure was changed during a test, the triaxial rig deforms elastically in response, which was also directly measured during the stage that the sample was fully

unloaded from differential load, and an additional correction was made to account for this effect.

4.3.2.2. Isostatic Consolidation Experiments

Isostatic consolidation tests on high-porosity samples at room temperature were conducted in our triaxial apparatus using a constant pore-pressure and a varying pore-pressure load-path. For the constant pore-pressure load-path, the confining pressure was increased stepwise while keeping pore pressure constant at 30.5 MPa (Figure 4.3, Table 4.4). For the varying pore-pressure load-path, confining pressure was increased stepwise and pore pressure was alternatively increased and then decreased to nearly zero (0.5 MPa) (Figure 4.4a, Table 4.5). The varying pore-pressure load-path involves both increasing and decreasing pore pressure, so special care was taken to ensure measurements of volume change were not affected by the changes in pore pressure. When pore pressure was increased, confining pressure was increased at the same rate such that their difference was kept unchanged from the previous consolidation step. Once pore pressure reached the target value, confining pressure was further increased to the final value (Figure 4.4b). When pore pressure was decreased, confining pressure was decreased at the same rate such that their difference was kept unchanged from the previous consolidation step. Once pore pressure reached the target value, confining pressure was increased back to the previous value (Figure 4.4c). Changing both confining and pore pressures took less than 10 minutes. Compared to total times of 12 hours for the consolidation test, the pressure adjustments are expected to affect only the instantaneous consolidation that mostly involves elastic strain. Keeping the difference

between confining and pore pressures constant during the change helps minimize elastic compaction (Nur and Byerlee, 1977). The varying pore-pressure load-path allows measurements of consolidation on the same sample at different pore pressures. In consolidation steps at very low pore pressure (i.e., 0.5 MPa), the difference between confining and pressures is approximated as true effective stress. Volumetric strains measured at these low pore pressures are considered with known effective stresses and compared with measurements at elevated pore pressures.

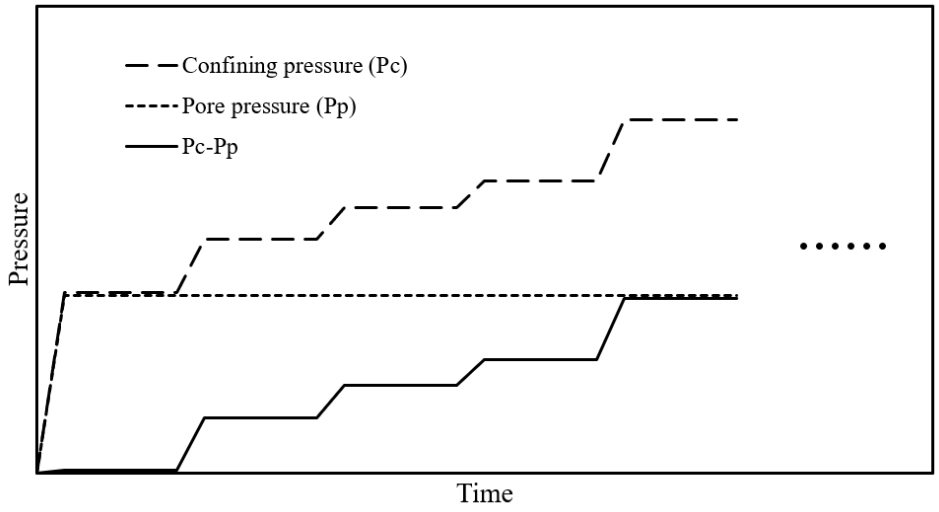

Figure 4.3 Schematic of constant pore-pressure load-path used in isostatic consolidation tests.

Table 4.4 Confining and pore pressures used in constant pore-pressure consolidation test

Consolidation Step	Confining Pressure (Pc) (MPa)	Pore Pressure (Pp) (MPa)	Pc - Pp (MPa)
0	31.5	30.5	1
1	40	30.5	9.5
2	45.5	30.5	15
3	50	30.5	19.5
4	60.5	30.5	30
5	70	30.5	39.5
6	90.5	30.5	60
7	110	30.5	79.5
8	140.5	30.5	110

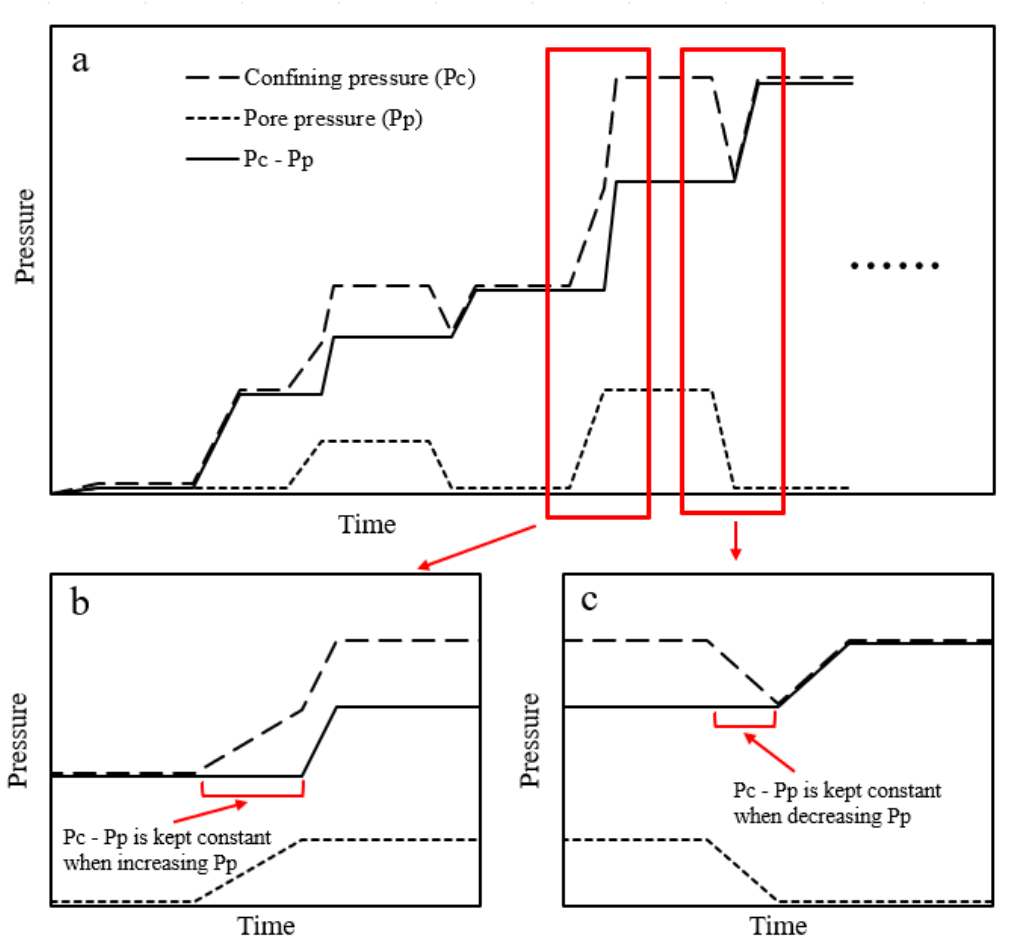

Figure 4.4 Schematic of (a) varying pore-pressure load-path used in isostatic consolidation tests, (b) and (c) details of confining pressure (Pc) and pore pressure (Pp) adjustments. Pc – Pp is kept constant while changing Pp.

Table 4.5 Confining and pore pressures used in varying pore-pressure consolidation test

Consolidation Step	Confining Pressure (Pc) (MPa)	Pore Pressure (Pp) (MPa)	Pc - Pp (MPa)
0	1.5	0.5	1
1	10	0.5	9.5
2	20	5	15
3	20	0.5	19.5
4	40	10	30
5	40	0.5	39.5
6	80	20	60
7	80	0.5	79.5
8	140	30	110
9	140	0.5	139.5

High-porosity samples of the consolidation tests were jacketed the same way as in the triaxial compression tests (Figure 4.2). Changes of pore volume during consolidation were measured through monitoring changes of pore fluid volume; therefore, we restricted pore fluid to the same silicone oil used in triaxial compression tests. We used a syringe pump to apply pore pressure and measure volume change. Volume resolution is 1.825 nanoliter, and over time pore pressure varies by only ±0.01 MPa.

High-porosity samples were prepared, saturated, and installed the same way as low-porosity samples of triaxial compression tests. Before starting consolidation, confining pressure was first increased to 1 MPa. Then both confining and pore pressures were increased while keeping 1 MPa difference until the starting pore pressure was reached. Once samples were fully equilibrated with confining and pore pressures, confining pressure was raised to start the first consolidation step.

To make accurate measurements of pore volume change, it is necessary to use pressure systems with excellent sealing. We made efforts to ensure proper sealing of both confining and pore pressure systems used in consolidation tests. Using a steel sample with the same instrumentation as synthetic salt-rock samples, the leaking rate of our pore pressure system was determined as 7×10^{-5} mL/hour at a constant pore pressure of 30.5 MPa (Figure 4.5). Applying this leaking rate to correct pore volume measurements leads to less than 0.5% change of volumetric strain for all consolidation steps.

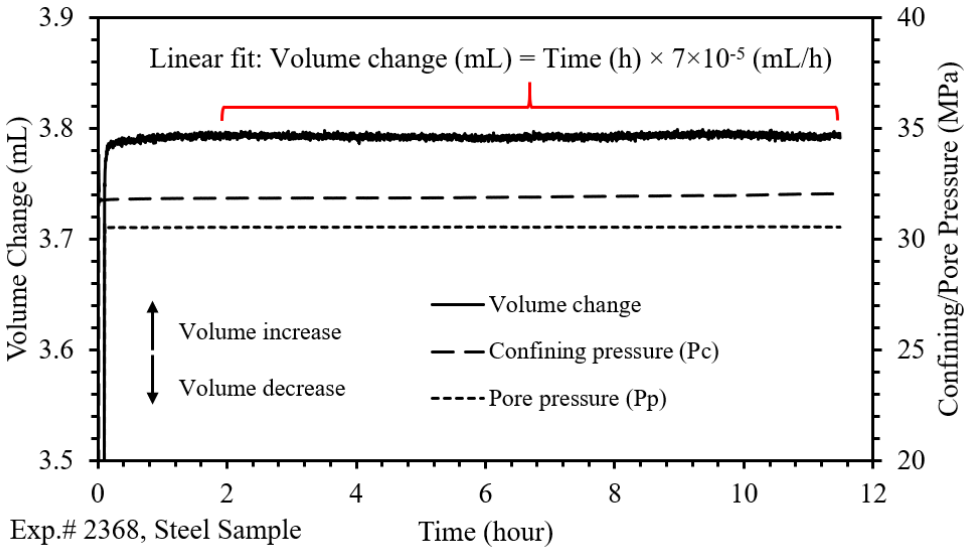

Figure 4.5 Leaking rate of pore pressure system used in isostatic consolidation tests. Steel sample was instrumented the same way as synthetic salt-rock sample. Leaking rate is determined over 9.5 hours.

All consolidation steps were stopped when the rate of change of pore fluid volume decreased to approximately 5×10^{-3} mL/hour, which typically took 0.5 to 12 hours depending on the consolidation stage. At the lowest consolidation rate, hourly

change of volume is below 1% of total volume change. As change of pore fluid volume is approximately a logarithmic function of time, it would take more than a week to reach the pore-pressure system leak rate. By using the same stopping criterion for all consolidation steps, the consolidation behavior can be compared across different stages and samples.

4.3.3. Microstructural Characterization

We studied microstructures of undeformed and key deformed synthetic salt-rocks samples using reflected-light microscopy to determine deformation mechanisms controlled by the effective stress law (Table 4.2). The sectioning and etching procedures followed those used in Section 2.2.5.

4.4. Results

4.4.1. Mechanical Behavior

4.4.1.1. Triaxial Compression Experiments

Triaxial compression tests at a confining pressure of 1 MPa and no pore fluid pressure show that the low-porosity samples deform in a ductile manner after yielding with only a slight increase in flow strength with strain (Figure 2.10). The flow strength is not affected by multiple full loading and unloading cycles. In each cycle, flow strength follows the trend of the previous cycle. Triaxial compression tests involving confining pressure stepping demonstrate that a step increase in effective stress by 1 MPa leads to an increase in flow strength that is clearly identified in the stress-strain curves (Figure 4.6). However, with a step in confining pressure back to previous values, flow strength does not fully recover to original values. The mechanical response of the sample to steps

in confining pressure (Figure 2.10 and 4.6) provides an excellent basis to evaluate effective stress law using the load path detailed in the Method section. If the effective stress increases during cycling confining and pore pressure while maintaining differential pressure constant, we expect to observe a clear increase of flow strength from the stress-strain curve. Otherwise, we can conclude that the effective stress coefficient is one or very close to one.

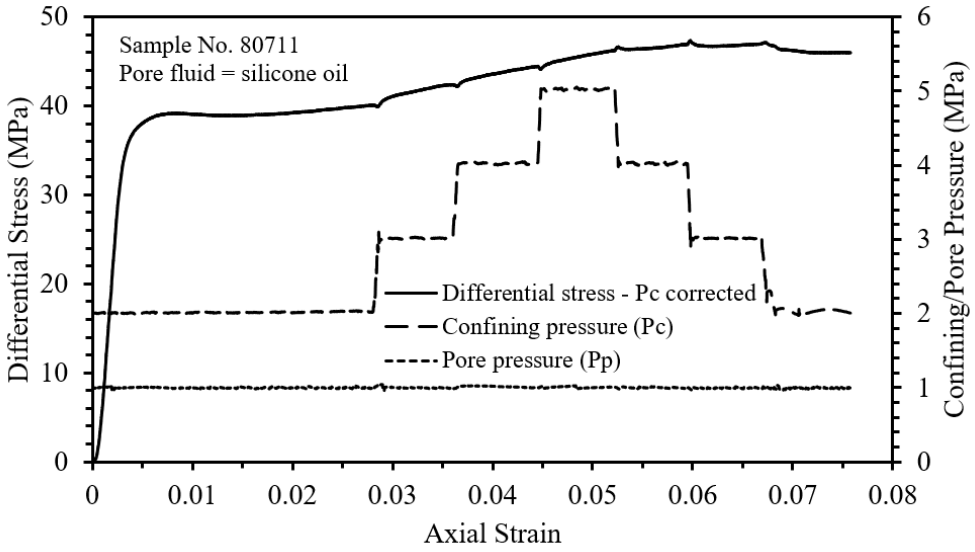

Figure 4.6 Differential stress versus axial strain for triaxial compression test using silicone oil as pore fluid. Pore pressure was constant at 1 MPa. Confining pressure was stepwise increased from 2 to 5 MPa and decreased back to 2 MPa. Differential stress was corrected for change of force gauge zero-point offset caused by confining pressure change.

The raw data for triaxial compression tests that cycle confining and pore pressure with silicone oil as pore fluid are illustrated in Figure 4.7. After confining and pore pressures are increased, the stress-strain curve is shifted. As described in the Method section, this is due to a change of the force-gauge zero-point offset and elastic distortion

of the loading column, both of which are caused by confining pressure changes. Once an appropriate correction is applied, the stress-strain curves represent true sample behavior (Figure 4.8). Comparing the first and second load cycles, the flow strength does not indicate a change even after increasing pore pressure by more than 2 orders of magnitude. After reducing pressures back to the starting values, the flow strength during the third cycle is slightly lower than the previous two cycles. The same mechanical behavior is observed in the triaxial compression test using argon gas as pore fluid (Figure 4.9 and 4.10), in which pore pressure is increased by about 1.4 orders of magnitude. At the test pressure range, the observed phenomenon is independent of pore fluid medium.

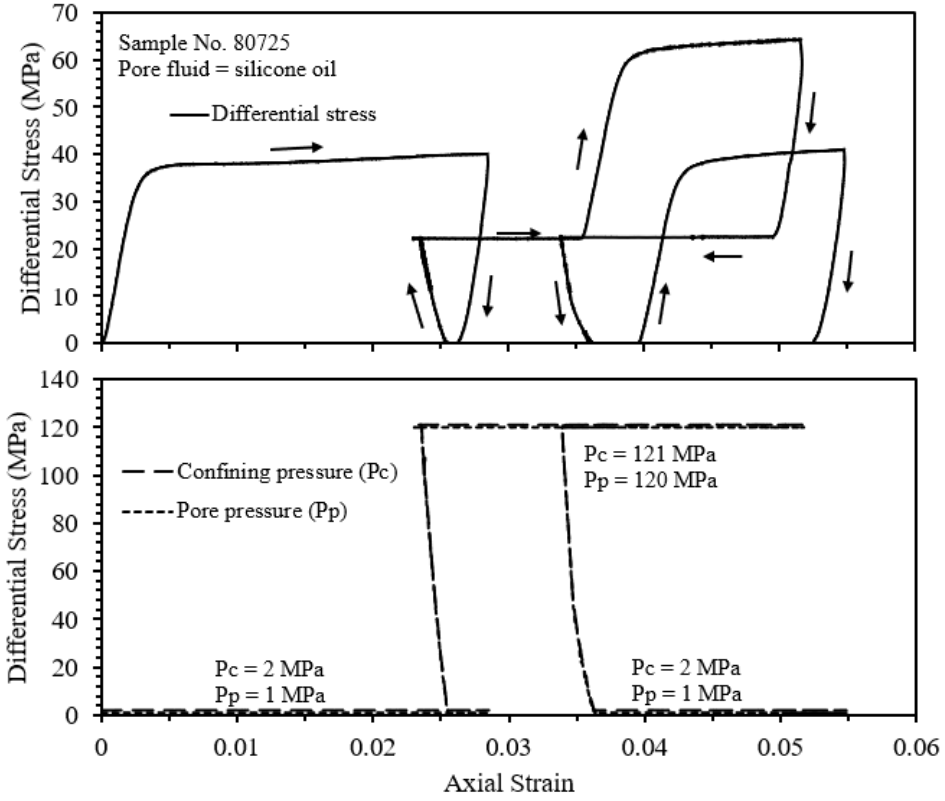

Figure 4.7 Top: raw data of differential stress versus axial strain for triaxial compression test using silicone oil as pore fluid; Bottom: confining pressure (Pc) and pore pressure (Pp) versus axial strain during test. Arrows show load path.

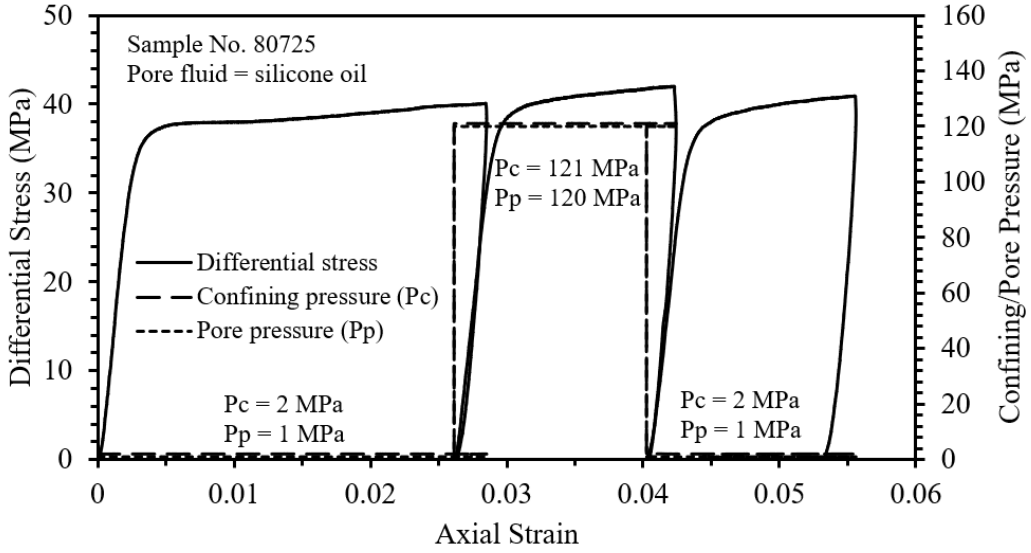

Figure 4.8 Differential stress versus axial strain for triaxial compression test using silicone oil as pore fluid after correction for change of force gauge zero-point offset and elastic distortion of loading rig both of which are caused by confining pressure change.

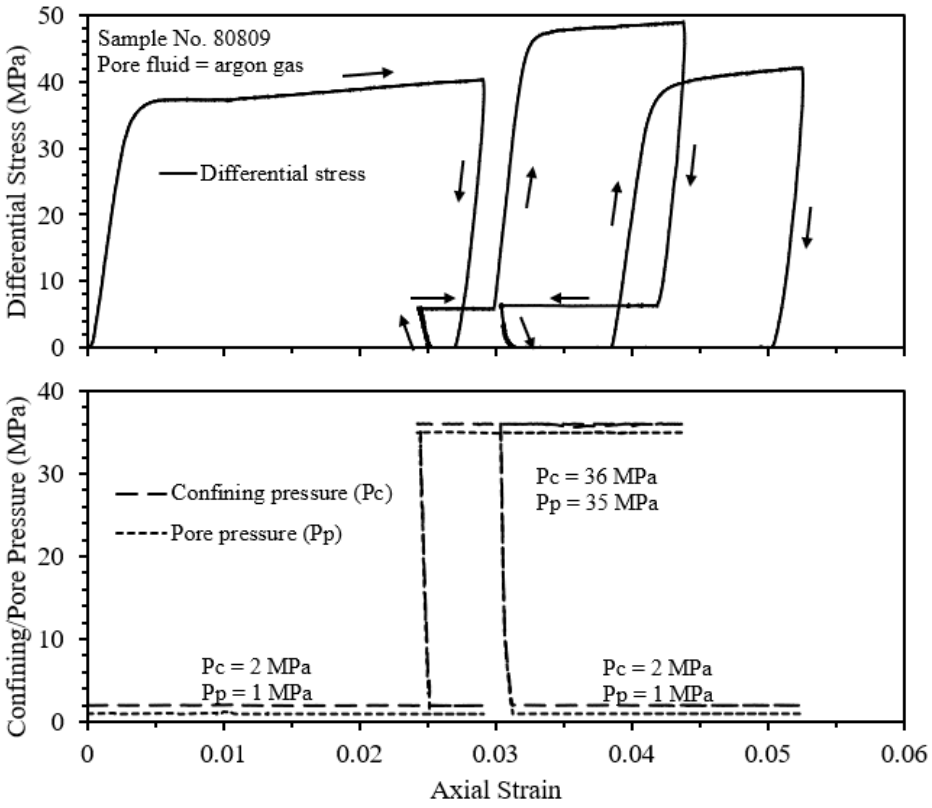

Figure 4.9 Top: raw data of differential stress versus axial strain for triaxial compression test using argon gas as pore fluid; Bottom: confining pressure (Pc) and pore pressure (Pp) versus axial strain during test. Arrows show load path.

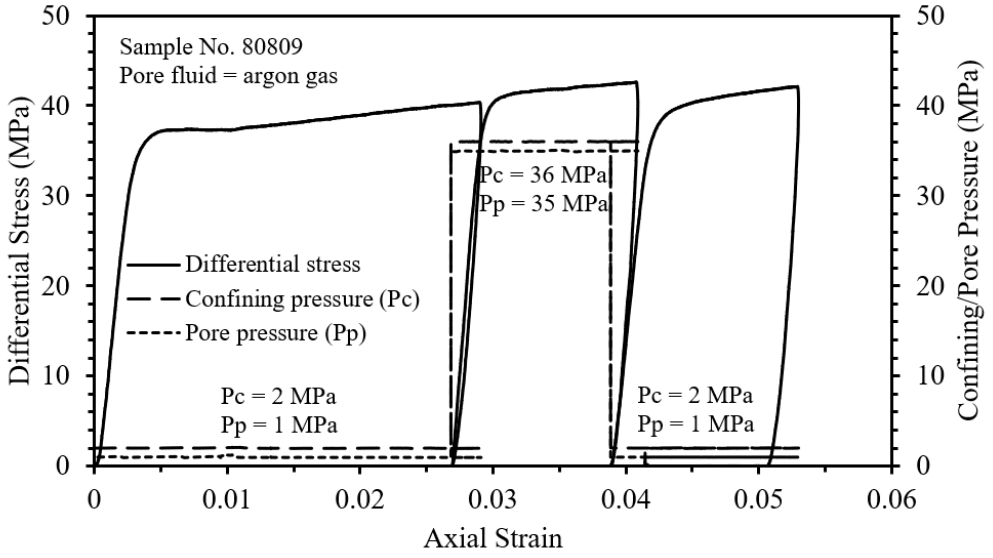

Figure 4.10 Differential stress versus axial strain for triaxial compression test using argon gas as pore fluid after correction for change of force gauge zero-point offset and elastic distortion of loading rig both of which are caused by confining pressure change.

4.4.1.2. Isostatic Consolidation Experiments

The raw data of pore volume change during consolidation are shown for constant pore-pressure (Figure 4.11) and varying pore-pressure (Figure 4.12) load-paths. Each consolidation step consists of an instantaneous strain response that directly correlates with pressure increase, followed by diminishing strain-rate with time at constant pressure. In constant pore-pressure tests, pore volume monotonically decreased. In varying pore-pressure tests, pore volume involved both an increase and decrease in the instantaneous phase; the increase and extended decrease in pore volume is associated with pore pressure changes. Consolidation at low- and high- pressure steps took less time than at intermediate-pressure steps. The time-dependent phase took as long as ~12 hours to reach the target (stopping) consolidation rate.

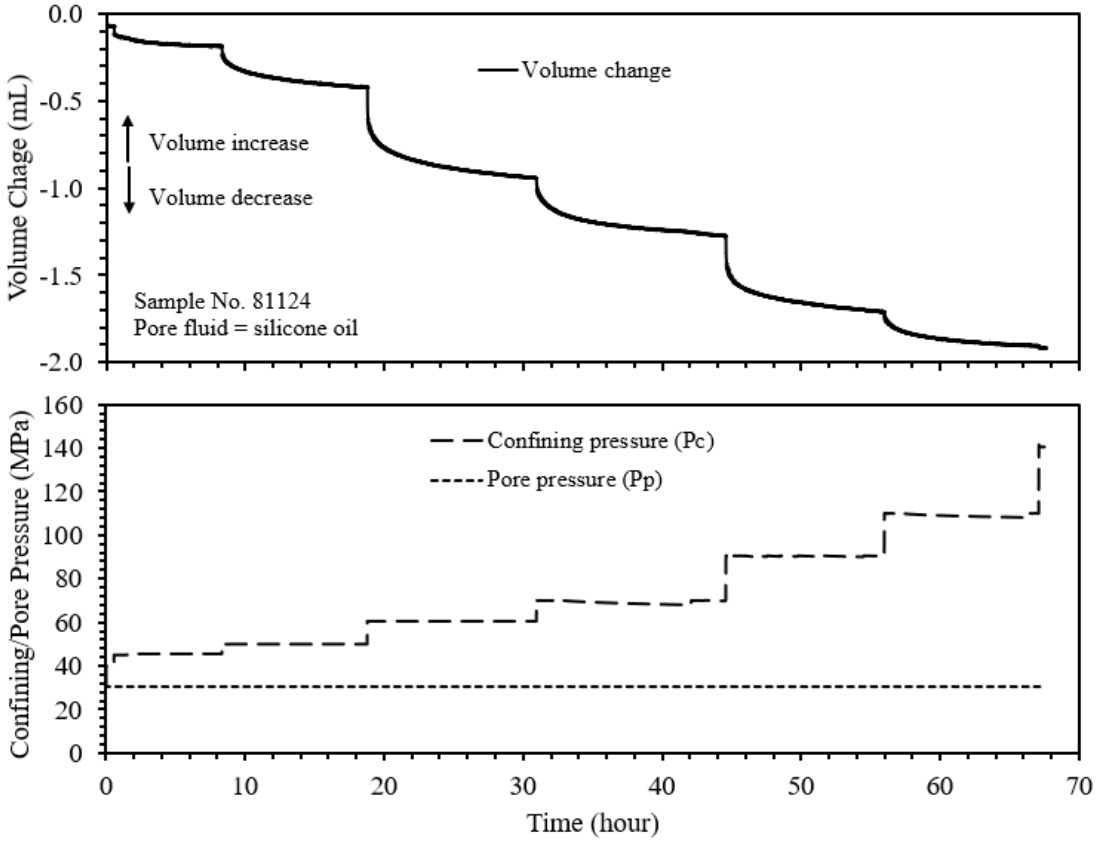

Figure 4.11 Top: raw data of pore volume change versus time for constant pore-pressure consolidation test; Bottom: confining pressure (Pc) and pore pressure (Pp) versus time during test.

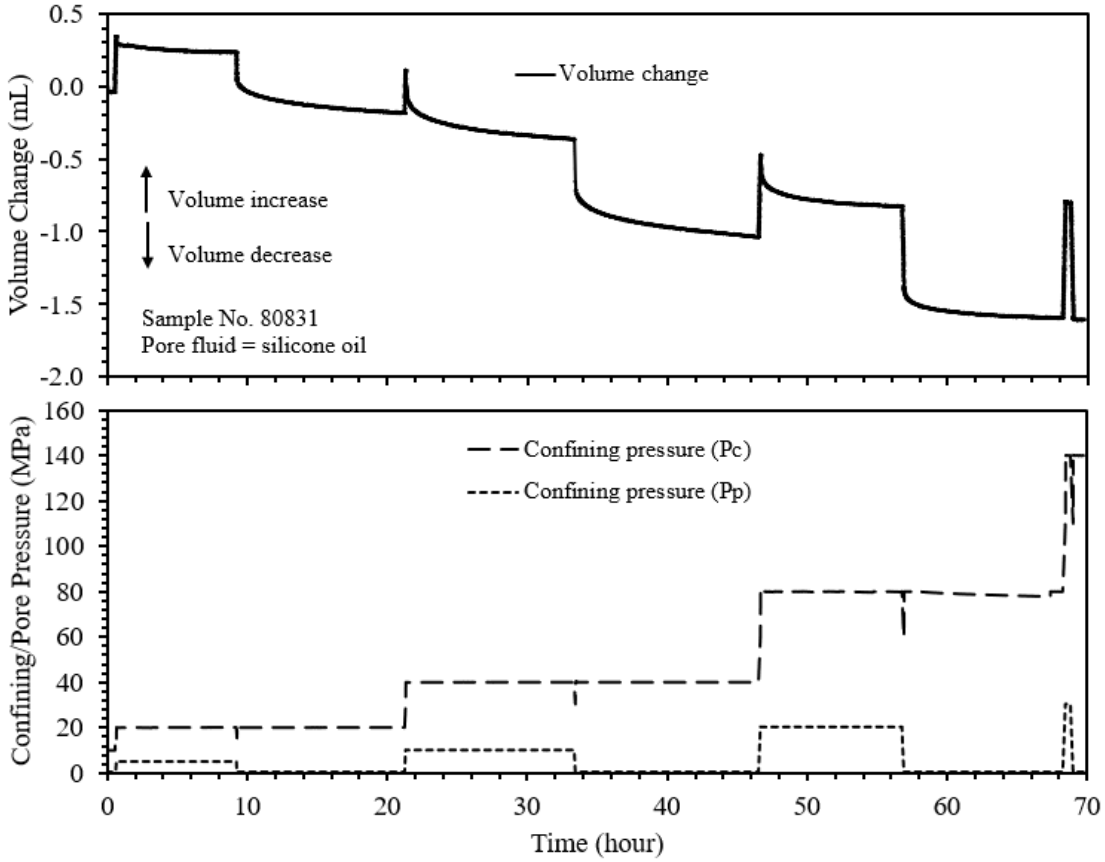

Figure 4.12 Top: raw data of pore volume change versus time for varying pore-pressure consolidation test; Bottom: confining pressure (Pc) and pore pressure (Pp) versus time during test.

After correcting for system leaking and pore pressure changes, the consolidation behavior may be represented in terms of volumetric strain as a function of the difference between confining and pore pressures for both of the consolidation load-paths (Figure 4.13). The volumetric strains for the two different load-paths are highly similar and do not present any systematic variation. Volumetric strains measured in the varying pore-pressure load-path, regardless of pore pressure applied, well match those of constant pore-pressure load-path at a higher pore pressure of 30.5 MPa. Volumetric strains measured at lowest pore pressure of 0.5 MPa can be regarded as known effective stress

because applied confining pressure is much greater than 0.5 MPa, and therefore this test can provide a reference for comparison. High consistency in volumetric strain for all pore pressures indicates that the effective stress for consolidation can be determined as the difference between confining and pore pressures with sufficient accuracy for the pressure range tested in this study.

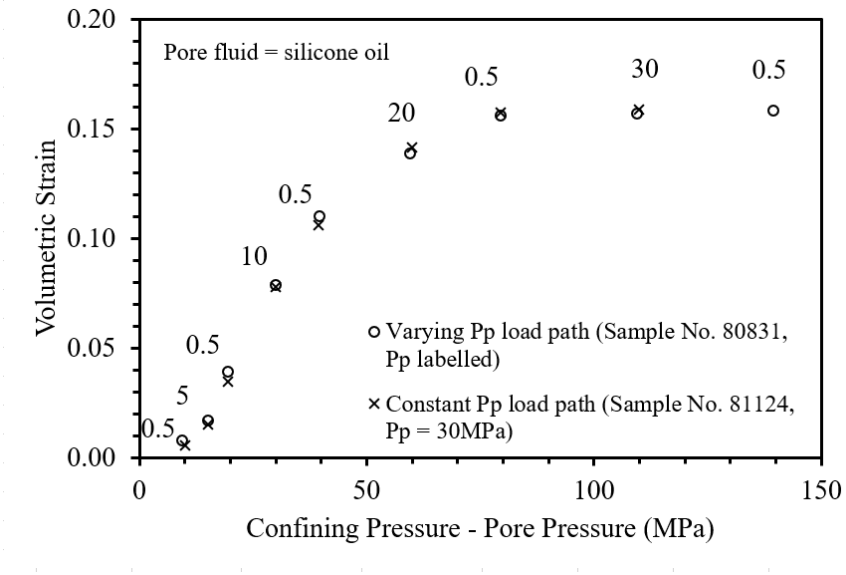

Figure 4.13 Volumetric strain versus confining pressure minus pore pressure for isostatic consolidation tests. Data of varying pore-pressure load-path are shown as hollow circles and labelled with pore pressure values. Data of constant pore-pressure load-path are shown as crosses. Volumetric strain was corrected for pore pressure system leaking and pore pressure change.

4.4.2. Microstructures

4.4.2.1. Triaxial Compression Experiments

The as-received reagent-grade granular salt is cubic-shaped, free of dislocation, and contains fluid inclusions (Figure 2.9a). The fabrication process led to many changes in salt grain structures. In low-porosity samples, initially cubic grains are rounded at the

corners due to crystal-plastic deformation (Figure 3.10b). The dominant grain substructures are the well-developed, dense, linear etch-features termed as slip lines. The wavy slip lines are indications of dislocation glide controlled by cross slip of screw dislocations (Senseny et al., 1992; Spiers & Carter, 1996). In some highly strained areas, the high dislocation density leads to development of recrystallized grains, which are characterized by straight boundaries and dislocation-feature-free interiors. The recrystallized grains are usually small and uncommon, and grew by grain boundary migration at the expense of the highly-deformed grains. Stress concentration at fluid inclusions caused minor intragranular cracking. Additional details concerning the microstructure of the low-porosity samples is provided in Section 3.3.2.

The microstructures of deformed, low-porosity samples, saturated with silicone oil and argon gas, share common features (Figure 4.14a, b). Many grain boundaries at low angles to differential load axis exhibit clear openings. These grain boundary openings can be easily identified because the geometry of the boundaries on the two sides of the opening match exactly, and thus previously in tight contact. To accommodate opening of grain boundaries, sliding along adjacent closed grain boundaries can be inferred on the basis of geometry and kinematics. Linked grain boundary cracking to produce opening and sliding is pervasive in the triaxially deformed samples, but absent in the starting material. Intragranular cracking is minor and often associated with fluid inclusions. Some recrystallized grains show signs of slip lines, but the density of slip lines is much lower than that of the original grains. All of the microstructural features in the deformed samples also are observed in low-porosity

samples deformed without pressure cycling (i.e., without the second cycle in Figure 4.1) described in Section 3.3.2. However, a clear difference is that the samples deformed with pressure cycling in this study show regions of larger and more abundant grain boundary opening (Figure 4.14c). The ratio of opened to total grain boundaries in these regions is more than twice as much as in other regions.

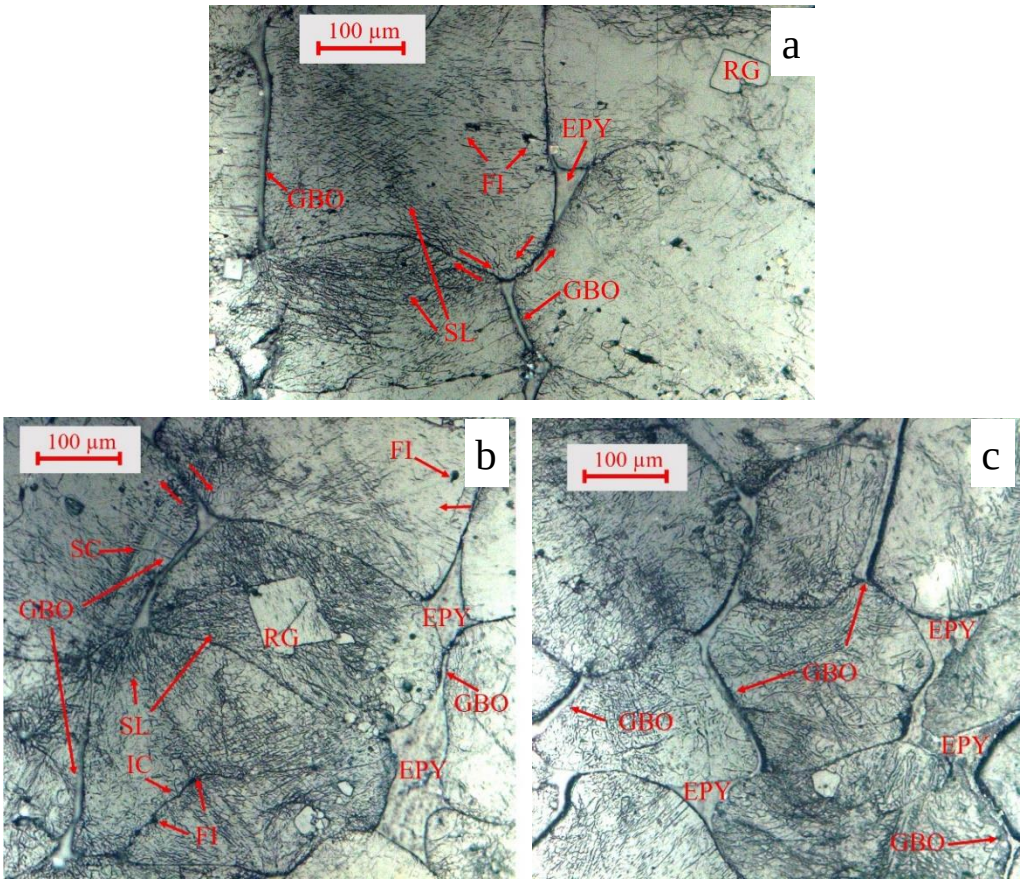

Figure 4.14 Reflected-light micrographs of (a) low-porosity sample 80725, (b) and (c) low-porosity sample 80809. Both samples were deformed in triaxial compression test. Differential load axis is vertical. Pore fluid is silicone oil for (a) and argon gas for (b) and (c). Note in (b) recrystallized grain (RG) shows low-density slip lines. (c) shows a region of abnormally high frequency of grain boundary opening. Paired arrows show inferred shear motion. EPY – epoxy (pore), FI – fluid inclusions intersected the polished surface, RG – recrystallized grain, SL – slip lines, GBO – grain boundary opening, IC – intragranular cracks, SC – scratch resulted from polishing.

4.4.2.2. Isostatic Consolidation Experiments

The microstructures of low-porosity samples before consolidation contain features that are similar to those of high-porosity sample: fluid inclusions, curved grain contacts, and wavy slip lines (Figure 4.15a). Apparent differences exist as well. In high-porosity samples, the densities of slip lines and intragranular cracks are much lower, and recrystallized grains are absent.

The microstructures of consolidated samples are completely changed from that of the starting material. Two types of grains are observed (Figure 4.15b). The first type shows slip lines observed in the starting material, representing intracrystalline-plastic deformed, original grains. The second type is characterized by straight grain boundaries, by rectangular or triangular euhedral shapes, and completely slip-line-free, representing newly recrystallized grains. The euhedral, new grains are much more abundant and often grew into the plastically deformed grains. Nearly all pore space is destroyed. Recrystallized grains still contain fluid inclusions.

The observed recrystallized microstructure reflects processes operated during consolidation. Visual inspection of samples right after consolidation tests reveals that they clearly changed from being opaque before consolidation to being translucent after consolidation. The change of salt sample transparency is closely correlated with defect density. Preparation of petrographic sections take 2-3 days during which recrystallization should nearly cease. We used the same process to make sections for our low-porosity samples and observed less than 4.8% recrystallized grains, which are often very small

(Figure 3.10b), even though low-porosity samples have much higher dislocation density than consolidated high-porosity samples.

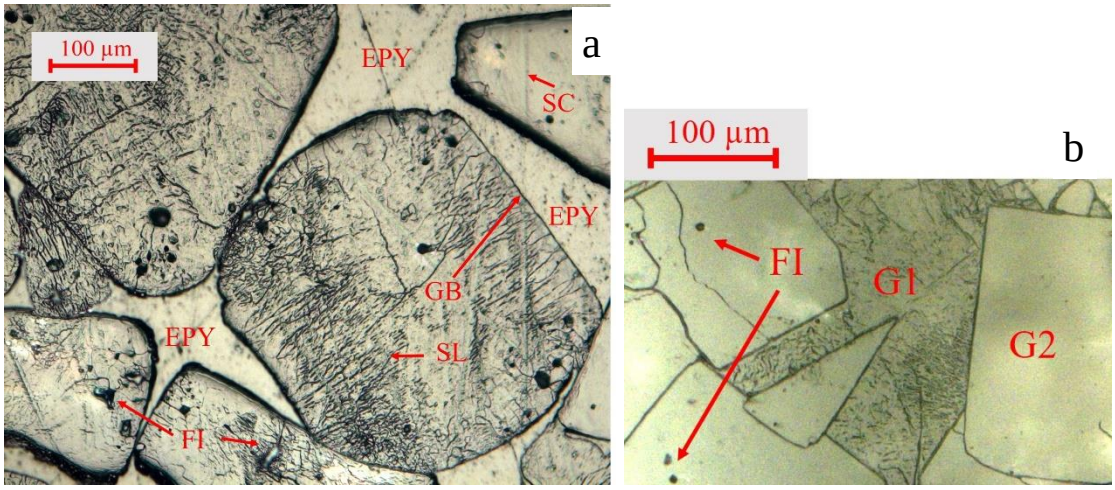

Figure 4.15 Reflected-light micrographs of (a) high-porosity sample 60421, (b) high-porosity sample 80831 deformed in a varying pore-pressure consolidation test. Pore fluid was silicone oil. G1 – grain type 1, deformed grains containing low-density slip lines, G2 – grain type 2, recrystallized, dislocation-free, and euhedral new grains, GB – grain boundary, EPY – epoxy (pore), SL – slip lines, FI – fluid inclusions intersected the polished surface, SC – scratch resulted from polishing.

4.5. Discussion

4.5.1. Deformation Mechanisms

4.5.1.1. Triaxial Compression Experiments

The mechanical behavior and microstructures of the low-porosity samples deformed herein are highly consistent with those observed in Chapter 3 involving only dry samples that were triaxially deformed at constant confining pressure of 1 MPa. This suggests that same deformation mechanisms operate in all the samples tested at an effective confining pressure of 1 MPa, a strain rate of 3×10^{-6} s^{-1}, and room temperature:

dominant grain boundary opening and sliding accompanied by minor intragranular cracking and dislocation glide. The grain boundary sliding is interpreted as dominantly a frictional process at a strain rate of 3×10^{-6} s^{-1} (Section 3.4). The cycling of confining and pore pressures while maintaining their difference at 1 MPa did not alter the deformation mechanisms. However, pressure cycling employed in the triaxial tests herein, specifically the drop in pressure prior to the third cycle, produced regions within the samples of more pervasive opened grain (Figure 4.14c), which was directly observed in the samples and can explain a flow strength in the third cycle that is slightly lower than that of previous two cycles. The cause of the opening is uncertain, but could represent a result of elastic expansion of halite grains during pressure decrease, or trapped highly-pressured pore fluids that popped grain boundaries during the reduction in confining pressure. At test pressure range, pore fluid phase did not affect the mechanical behavior and micromechanisms.

4.5.1.2. Isostatic Consolidation Experiments

Mechanical behavior during the consolidation tests show instantaneous and time-dependent change of pore volume over time. The instantaneous consolidation is caused by elastic and minor brittle deformation both of which are time-independent. The time-dependent phase is interpreted as achieved by coupled crystal-plasticity and recrystallization. The observation of both deformed and dislocation-free halite grains suggests crystal-plasticity and recrystallization may operate in a coupled way to reduce pore space. Pressure increase leads to dislocation motions that increase its density. Halite grains of high dislocation density recrystallize to reduce internal energy.

Recrystallization produces dislocation-free grains that are prone to crystal-plastic deformation that builds up dislocation.

Samples used in this study contain a water content of ~300 ppm (weight $H_2O/10^6$ NaCl) (Section 3.2.2). For fine-grained salt-rock (0.08-2 mm), this water content is sufficient to invoke fluid-assisted grain boundary processes, notably grain boundary migration recrystallization and solution-transfer creep (Spiers & Carter, 1996; Ter Heege et al., 2005; Watanabe & Peach, 2002). Since recrystallization of fully dry halite requires temperature higher than 400 °C (Franssen, 1993), it appears that the recrystallization observed here is achieved by fluid-assisted grain boundary migration. This interpretation is also supported by the observation that recrystallized grains often appear at grain boundaries or interior adjacent to fluid inclusions in which brine resides. Pennock et al. (2007) reported highly similar microstructures of halite aggregates in their consolidation and stress relaxation experiments at room temperature and interpreted same recrystallization process. Recrystallization through fluid-assisted grain boundary migration in halite is well documented with direct observations of brine-filled grain boundaries (Schenk & Urai, 2003; Schenk et al., 2006). We used silicone oil as pore fluid for our consolidation tests which may restrict movement of brines from fluid inclusions to grain boundaries, and thus inhibit solution-transfer creep (e.g., pressure solution). We did not observe any microstructural evidence for solution-transfer creep, and it is unlikely to contribute significantly to deformation during a short-term (i.e., ~3 day) test.

4.5.2. Effective Stress Coefficient

4.5.2.1. Triaxial Compression Experiments

Our low-porosity samples have a starting porosity of ~5.4% and were fully saturated before testing. Triaxial compression at low confining pressure and room temperature led to grain boundary opening and therefore an increase in porosity during deformation (Section 3.4). The external measurements of pore pressure should reflect true pore pressure in the sample during deformation, or at least fairly close to. If pore pressure in sample was much lower than external measurements, then differential confining pressure would be much higher than 1 MPa. This should have led to an apparent increase in flow strength.

The stress-strain response shows no apparent increase in flow strength after increasing confining and pore pressures. This observation applies to tests using silicone oil and to argon gas as pore fluids. Pressure stepping test shows the flow strength is at least sensitive to 1 MPa increase in effective pressure (Figure 4.6). In triaxial compression test with silicone oil, pore pressure was increased by 119 MPa (Figure 4.8). Using Equation 4.9, the effective stress coefficient can be estimated to be greater than 0.992. It is therefore inferred that the effective stress coefficient is very close to one or equals one at test conditions. This suggests Terzaghi's effective stress law holds for deformation mechanisms encountered in triaxial compression experiments. While intracrystalline process of dislocation glide is pressure-insensitive, brittle processes of grain boundary cracking depend on effective pressure. Dominant grain boundary sliding and opening are the primary mechanisms for accommodating axial shortening during

triaxial deformation. As grain boundary sliding involves mostly frictional processes at test conditions, pore fluid pressure is likely transmitted along those sliding boundaries such that the Terzaghi's effective stress law is followed and flow strength is unaffected by pressure cycling.

Halite has low yield strength even at room temperature (Carter & Heard, 1970), so our experiments provide an opportunity to evaluate the physical basis for effective stress law based on contact-scale micromechanics. Several studies proposed that effective stress coefficient can be determined through analysis of contact-scale force balance by assuming true area of contact is a result of plastic yielding at contacting grain boundaries (Beeler et al., 2016; Scholz, 2002; Skempton, 1960). In our triaxial experiments, true area of grain contact is inferred to be large. Grain boundaries oriented nearly normal to differential load axis are closed and do not slide during semibrittle flow (Figure 4.14a, b). Nominal normal stress (excluding the effects of pore pressure) acting on them could be as high as 161 MPa for those perpendicular to load axis when confining pressure was raised to 121 MPa. At room temperature, the highest yield stress of halite crystals measured by Carter and Heard (1970) at a strain rate of $1.1\text{-}2.3\times10^{-4}$ /sec is about 80 MPa at 10% axial strain. A higher applied normal stress than material yield strength implies that those closed grain boundaries are likely in true contact with no communication with pore pressure, based on contact-scale force balance considering plastic yielding (e.g., Beeler et al., 2016). On the other hand, opening grain boundaries are clearly not in contact and sliding grain boundaries have very low true grain contact area during frictional sliding. Although opening and sliding grain boundaries are

abundant, those high-normal-stress grain boundaries account for no less than 26% of total grain area estimated by measuring grain boundary lengths in microstructures. Their presence should cause the ratio of true to total contact area significantly deviate from one in triaxial deformation. Absence of clear change in flow strength indicates that effective stress coefficient is not controlled by true area of grain contact. Instead, the nature of deformation mechanism should be taken into account for effective stress analysis. In our triaxial experiments, those closed, high-normal-stress grain contacts deform primarily by dislocation processes that are independent on effective pressure.

The experimental method used in this study is similar to that used by Bishop and Skinner (1977). They tested cohesionless granular aggregates and applied lower pressures with a highest confining pressure of 27.58 MPa. Among all material tested, i.e., silt, sand, marble, and lead shot, Bishop and Skinner (1977) found that an effective stress coefficient of one describes shear strength of granular flow with sufficient accuracy, therefore, Terzaghi's effective stress law is valid. In their study, lead shot presents most similarities to salt used in this study since they both deform easily through crystal-plasticity at room temperature. Again, no discernable difference in flow strength was observed during pressure cycling, even though true area of grain contact is estimated to be large enough for causing a deviation of effective stress coefficient from one. It is likely that, similar to our triaxial experiments, the large true area of grain contact in lead shots forms primarily by dislocation processes and therefore is independent on effective stress.

4.5.2.2. Isostatic Consolidation Experiments

The consolidation behavior of varying and constant pore-pressure tests shows high agreement for all pore pressures applied when plotting volumetric strain as a function of the difference between confining and pore pressures. This suggests the difference between confining and pore pressures is an accurate reflection of effective consolidation stress at test conditions. In the form effective stress law, it is equivalent to an effective stress coefficient of one or very close to one. If the effective stress coefficient was sufficiently less than one, consolidation behavior at different pore pressures would exhibit clear separation at intermediate pressure steps when plotting the difference between confining and pore pressures in the x-axis (Figure 4.16).

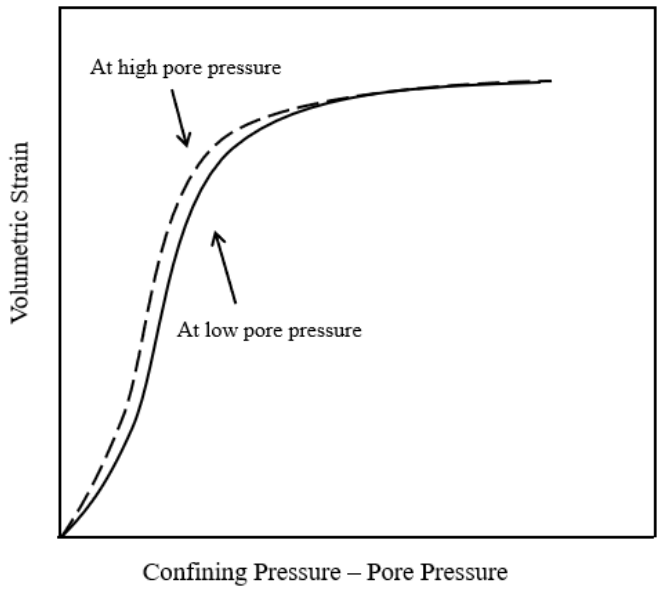

Figure 4.16 Hypothetical consolidation behavior plotted as volumetric strain versus the difference between confining and pore pressures assuming the effective stress coefficient is sufficiently less than one.

An effective stress coefficient of effectively one for consolidation may be explained by the stress states in a consolidating salt aggregate. In the instantaneous consolidation phase, deformation primarily involves elastic and brittle processes that can be well described by an effective stress coefficient of one (Skempton, 1960; Nur & Byerlee, 1971). In the time-dependent phase, microstructure points to a coupled crystal-plastic deformation and recrystallization. Crystal-plastic deformation involving movements of dislocations requires application of differential stress that may be caused by the different stress states at solid grain-to-grain contacts and at grain interior adjacent to pore pressure. Recrystallization recycles grains of high density of defects and allows crystal-plasticity to operate until sufficient grain contacts are created such that differential stress is too low to drive further dislocation movements. As dislocation processes and recrystallization are insensitive to effective pressure, pore volume reduction is primarily driven by the differential pressure between confining and pore pressures, manifesting an effective stress coefficient of one. Consolidation reduced sample porosity from 19% to below 4%. Comparing microstructures before and after consolidation (Figure 4.15a vs. b), there is little doubt that true area of contact has increased dramatically during consolidation. Furthermore, this indicates that the effective stress coefficient is not dictated by true area of contact and an effective stress law for consolidation in the form of Equation 4.5 is unlikely.

Skempton (1960) analyzed consolidation data of lead shot from Laughton (1955) and demonstrated that both Terzaghi's expression and Equation 4.7 well describe consolidation behavior of lead shot. An effective stress coefficient of one for lead shot is

consistent with Equation 4.7, since the compressibility of lead shots is much smaller than that of lead shot aggregates. Consolidation in lead shot aggregates is achieved primarily through elastic and crystal-plastic deformation. This is similar to the consolidation of salt grains in this study except that recrystallization was involved in consolidation of salt grains. As recrystallization does not produce deformation (Urai et al., 1986), consolidation mechanisms are similar in lead shot and salt. Therefore, an effective stress coefficient of one for both lead shot and salt is consistent. Our salt consolidation data is also in good agreement of Equation 4.7. Using the two data points before the level off stage of consolidation in Figure 4.13, bulk compressibility is determined as 8×10^{-4} MPa^{-1}. For a halite compressibility of 4.2×10^{-4} MPa^{-1} (Robertson et al., 1958), this yields an effective stress coefficient of 0.95 that is very close to one.

4.5.3. Implications

Our experimental study reveals that an effective stress coefficient of one gives sufficient accuracy for describing flow strength involving primarily grain boundary sliding and opening as well as consolidation through coupled crystal-plasticity and recrystallization. This may provide a basis for understanding the mechanical behavior for engineered salt structures and salt tectonics. Analyses of salt structure integrity and stability require knowledge of effective stress states in order to apply rheological models (e.g., Fokker, 1995; Minkley et al., 2015). This holds true for the understanding of evolving salt formations at geological time scales as well (e.g., Davison et al., 1996; Nikolinakou et al., 2014).

Considering salt as an analogue to other rock-forming material, our findings suggest we may safely apply Terzaghi's effective stress law in lower crust when similar deformations are involved. At brittle-plastic transition, it is possible to encounter similar deformation mechanisms such as grain boundary sliding and opening, especially when pore pressure is elevated (Evans et al., 2013; Paterson & Wong, 2005). In areas where stress states are close to isostatic and temperature is high enough, pore space can be reduced through coupled crystal-plasticity and recrystallization. In these scenarios, the effective stress coefficient is effectively one. Our results provide a basis for analyses of mechanical behavior involving pore fluid pressure at similar deformation processes.

4.6. Conclusions

We conducted triaxial compression and isostatic consolidation experiments on two types of synthetic salt-rocks at room temperature to investigate the effective stress relationship controlling flow strength and volumetric strain. Our mechanical and microstructural data lead to the following conclusions:

1. For semibrittle flow of salt-rocks through primarily grain boundary sliding and opening, flow strength is controlled by an effective stress relation with an effective stress coefficient of one or nearly one. The effective stress state is not controlled by true area of grain contact involving plastic yielding.
2. For isostatic consolidation of salt-rocks involving coupled crystal-plasticity and fluid-assisted grain boundary migration recrystallization, volumetric strain is also controlled by an effective stress relation with an effective stress coefficient of one or

nearly one. The effective consolidation stress is not controlled by true area of grain contact either.

5. SUMMARY

Deformation experiments on granular salt and synthetic salt-rocks are integrated with microstructural observations to reveal grain scale processes responsible for consolidation, grain boundary deformation, anelasticity, and to test the effective stress relationship for semibrittle materials. Uniaxial consolidation of granular salt at temperatures of 100°C to 200°C and grain sizes of 1 mm to 2 mm is primarily achieved by intracrystalline plastic deformation. Among grain type, grain size, temperature, and load path, consolidation behavior is mostly affected by temperature. At room temperature and low confinement, grain boundary microcracking is the dominant brittle deformation mechanism in work-hardened synthetic salt-rocks during stress cycling. Opening-mode grain boundary cracks develop preferentially in the loading direction and tend to link with increasing inelastic deformation, which could be an important mechanism for spalling at salt cavern walls

Semibrittle flow was observed in both work-hardened and annealed synthetic salt-rocks at a confining pressure of 1 MPa, strain rate of 3×10^{-6} s^{-1}, and room temperature. Deformation occurs by grain boundary sliding and opening, intragranular cracking, and dislocation glide. Grain boundary sliding is pronounced in both sample types and predominantly a frictional process at strain rates higher than 3×10^{-6} s^{-1}. In wet samples, fluid-assisted diffusion facilitates sliding along grain boundaries at low strain rates and at low differential stresses.

During semi-brittle flow at high stress, debonding and frictional sliding at grain boundaries can change the elastic properties (i.e., Young's modulus and Poisson's ratio). In addition, grain boundary sliding with fluid-assisted diffusion produces time-dependent elasticity (i.e., anelasticity) and hysteresis. At very low differential loads, slipped, closed boundaries heal by rebonding over time periods of hours, to nearly recover original elastic properties.

During semibrittle flow of work-hardened synthetic salt-rocks, flow strength remains constant for changes in pore fluid pressure of more than two orders of magnitude while differential pressure is kept constant. Based on the rearranged general-form of the effective stress relationship $\sigma^e = (\sigma - Pp) + (1 - \alpha)Pp$, this implies that the effective stress coefficient, α, is one or very close to one. Volumetric strains measured during isostatic consolidation of work-hardened synthetic salt-rocks by combined dislocation glide and fluid-assisted grain-boundary migration recrystallization are independent of pore pressure if differential pressure is held constant. Thus consolidation behavior also is well described by an effective stress relation with α being one or nearly one. Analysis of grain contact area for both sliding boundaries and boundaries in contact by intracrystalline plastic yielding indicates that α is independent of the true area of grain contact.

REFERENCES

Baar, C. A. (1977). *Applied salt-rock mechanics 1: The in-situ behavior of salt rocks*. Amsterdam: Elsevier.

Beeler, N. M., Hirth, G., Thomas, A., & Bürgmann, R. (2016). Effective stress, friction, and deep crustal faulting. *Journal of Geophysical Research: Solid Earth*, *121*(2), 1040–1059. https://doi.org/10.1002/2015JB012115

Bérest, P. (2013). *The mechanical behavior of salt and salt caverns*. Paper presented at ISRM International Symposium - EUROCK 2013, International Society for Rock Mechanics and Rock Engineering, Wroclaw, Poland.

Bishop, A. W. & Skinner, A. E. (1977). The influence of high pore-water pressure on the strength of cohesionless soils. *Philosophical Transactions of the Royal Society A, 284*(1318), 91–130. https://doi.org/10.1098/rsta.1977.0001

Bos, B. & Spiers, C. J. (2002). Fluid-assisted healing processes in gouge-bearing faults: Insights from experiments on a rock analogue system. *Pure and Applied Geophysics*, *159*(11–12), 2537–2566. https://doi.org/10.1007/s00024-002-8747-2

Bourcier, M., Bornert, M., Dimanov, A., Héripré, E., & Raphanel, J. L. (2013). Multiscale experimental investigation of crystal plasticity and grain boundary sliding in synthetic halite using digital image correlation. *Journal of Geophysical Research: Solid Earth*, *118*, 511–526. https://doi.org/10.1002/jgrb.50065

Brace, W. F. & Kohlstedt, D. L. (1980). Limits on lithospheric stress imposed by laboratory experiments. *Journal of Geophysical Research: Solid Earth, 85*(B11),

6248–6252. https://doi.org/10.1029/JB085iB11p06248

Brace, W. F. & Martin, R. J. (1968). A test of the law of effective stress for crystalline rocks of low porosity. *International Journal of Rock Mechanics and Mining Sciences & Geomechanics*, *5*(5), 415–426. https://doi.org/10.1016/0148-9062(68)90045-4

Brace, W. F., Paulding, B. W., & Scholz, C. (1966). Dilatancy in the fracture of crystalline rocks. *Journal of Geophysical Research*, *71*(16), 3939–3953. https://doi.org/10.1029/JZ071i016p03939

Brouard, B., Bérest, P., Djizanne, H., & Frangi, A. (2012). Mechanical stability of a salt cavern submitted to high-frequency cycles. *Proceedings of the Conference on the Mechanical Behavior of Salt VII*, 381–390.

Carter & Hansen, F. D. (1983). Creep of rocksalt. *Tectonophysics*, *92*(4), 275–333. https://doi.org/10.1016/0040-1951(83)90200-7

Carter & Heard, H. C. (1970). Temperature and rate dependent deformation of halite. *American Journal of Science*, *269*(3), 193–249. https://doi.org/10.2475/ajs.269.3.193

Carter, N. L., Horseman, S. T., Russell, J. E., & Handin, J. (1993). Rheology of rocksalt. *Journal of Structural Geology*, *15*(9–10), 1257–1271. https://doi.org/10.1016/0191-8141(93)90168-A

Carter, N. L. & Kirby, S. H. (1978). Transient creep and semibrittle behavior of crystalline rocks. *Pure and Applied Geophysics*, *116*(4–5), 807–839. https://doi.org/https://doi.org/10.1007/BF00876540

Chester, F. M. (1988). The brittle-ductile transition in a deformation-mechanism map for halite. *Tectonophysics*, *154*(1–2), 125–136. https://doi.org/10.1016/0040-1951(88)90230-2

Chester, F. M. (1989). Dynamic recrystallization in semi-brittle faults. *Journal of Structural Geology*, *11*(7), 847–858. https://doi.org/10.1016/0191-8141(89)90102-8

Cole, R. (2002). *The long term effects of high pressure natural gas storage on salt caverns*. Paper presented at Solution Mining Research Institute Spring Meeting, Banff, Alberta, Canada.

Davison, I., Alsop, I., & Blundell, D. (1996). Salt tectonics: Some aspects of deformation mechanics. *Geological Society, London, Special Publications*, *100*(1), 1–10. https://doi.org/10.1144/GSL.SP.1996.100.01.01

Dieterich, J. H. & Kilgore, B. D. (1994). Direct observation of frictional contacts: New insights for state-dependent properties. *Pure and Applied Geophysics*, *143*(1–3), 283–302. https://doi.org/10.1007/BF00874332

Dieterich, J. H. & Kilgore, B. D. (1996). Imaging surface contacts: Power law contact distributions and contact stresses in quartz, calcite, glass and acrylic plastic. *Tectonophysics*, *256*(1–4), 219–239. https://doi.org/10.1016/0040-1951(95)00165-4

Ding, J., Chester, F. M., & Chester, J. S. (2017). *Microcrack network development in salt-rock during cyclic loading at low confining pressure*. Paper presented at 51st U.S. Rock Mechanics/Geomechanics Symposium, American Rock Mechanics Association, San Francisco, CA.

Ding, J., Chester, F. M., Chester, J. S., Zhu, C., & Arson, C. (2016). *Mechanical*

behavior and microstructure development in consolidation of nominally dry granular salt. Paper presented at 50th U.S. Rock Mechanics/Geomechanics Symposium, American Rock Mechanics Association, Houston, TX.

Evans, B., Fredrich, J. T., & Wong, T. (2013). The brittle-ductile transition in rocks: Recent experimental and theoretical progress. In Duba, A. G., Durham, W. B., Handin, J. W., Wang, H. F. (Eds.), *The brittle-ductile transition in rocks, Geophysical Monograph Series* (Vol. 56, pp. 1–20). Washington, DC: American Geophysical Union. https://doi.org/10.1029/GM056p0001

Evans, B. & Kohlstedt, D. L. (1995). Rheology of rocks. In Ahrens, T. J. (Eds.), *Rock physics and phase relations: A handbook of physical constants, AGU Reference Shelf* (Vol. 3, pp. 148–165). Washington, DC: American Geophysical Union. https://doi.org/10.1029/RF003p0148

Fokker, P. A. (1995). *The behaviour of salt and salt caverns*, (Doctoral dissertation). Retrieved from TUDelft Institutional Repository. (http://repository.tudelft.nl/view/ir/uuid:6847f8e4-3b09-4787-be02-bcce9f0eed06). Delft, Netherlands: Delft University of Technology

Franssen, R. C. M. W. (1993). *Rheology of synthetic rocksalt: With emphasis on the influence of deformation history and geometry on the flow behaviour*, (Doctoral dissertation). Retrieved from Utrecht University Repository. (https://dspace.library.uu.nl/handle/1874/268390). Utrecht, Netherlands: Utrecht University

Fredrich, J. T., Evans, B., & Wong, T. (1989). Micromechanics of the brittle to plastic

transition in Carrara marble. *Journal of Geophysical Research: Solid Earth*, *94*(B4), 4129–4145. https://doi.org/10.1029/JB094iB04p04129

French, M. E., Chester, F. M., & Chester, J. S. (2015). Micromechanisms of creep in clay-rich gouge from the Central Deforming Zone of the San Andreas Fault. *Journal of Geophysical Research: Solid Earth*, *120*(2), 827–849. https://doi.org/10.1002/2014JB011496

Ghahremani, F. (1980). Effect of grain boundary sliding on anelasticity of polycrystals. *International Journal of Solids and Structures*, *16*(9), 825–845. https://doi.org/10.1016/0020-7683(80)90052-9

Hadizadeh, J. & Tullis, J. (1992). Cataclastic flow and semi-brittle deformation of anorthosite. *Journal of Structural Geology*, *14*(1), 57–63. https://doi.org/10.1016/0191-8141(92)90144-L

Handin, J., Hager Jr, R. V, Friedman, M., & Feather, J. N. (1963). Experimental deformation of sedimentary rocks under confining pressure: Pore pressure tests. *AAPG Bulletin*, *47*(5), 717–755. https://doi.org/10.1306/BC743A87-16BE-11D7-8645000102C1865D

Hirth, G. & Tullis, J. (1994). The brittle-plastic transition in experimentally deformed quartz aggregates. *Journal of Geophysical Research: Solid Earth*, *99*(B6), 11731–11747. https://doi.org/10.1029/93JB02873

Hubbert, M. K. & Rubey, W. W. (1959). Role of fluid pressure in mechanics of overthrust faulting: I. Mechanics of fluid-filled porous solids and its application to overthrust faulting. *Bulletin of the Geological Society of America, 70*(2), 115–166.

Hwang, C. L., Wang, M. L., & Miao, S. (1993). Proposed healing and consolidation mechanisms of rock salt revealed by ESEM. *Microscopy Research and Technique*, *25*(5–6), 456–464. https://doi.org/10.1002/jemt.1070250517

Kirby, S. H. (1980). Tectonic stresses in the lithosphere: Constraints provided by the experimental deformation of rocks. *Journal of Geophysical Research: Solid Earth*, *85*(B11), 6353–6363. https://doi.org/10.1029/JB085iB11p06353

Kirby, S. H. & Kronenberg, A. K. (1984). Deformation of clinopyroxenite: Evidence for a transition in flow mechanisms and semibrittle behavior. *Journal of Geophysical Research: Solid Earth*, *89*(B5), 3177–3192. https://doi.org/10.1029/JB089iB05p03177

Knipe, R. J. (1989). Deformation mechanisms - Recognition from natural tectonites. *Journal of Structural Geology*, *11*(1–2), 127–146. https://doi.org/10.1016/0191-8141(89)90039-4

Kohlstedt, D. L., Evans, B., & Mackwell, S. J. (1995). Strength of the lithosphere: Constraints imposed by laboratory experiments. *Journal of Geophysical Research: Solid Earth*, *100*(B9), 17587–17602. https://doi.org/10.1029/95JB01460

Laubscher, H. P. (1960). Role of fluid pressure in mechanics of overthrust faulting: Discussion. *Geological Society of America Bulletin*, *71*(5), 611–616.

Laughton, A. S. (1955). *The compaction of ocean sediments*, (Doctoral dissertation). Cambridge, United Kingdom: University of Cambridge

Lawn, B. R. & Marshall, D. B. (1998). Nonlinear stress-strain curves for solids containing closed cracks with friction. *Journal of the Mechanics and Physics of*

Solids, *46*(1), 85–113. https://doi.org/10.1016/S0022-5096(97)00036-7

Marti, S., Stünitz, H., Heilbronner, R., Plümper, O., & Drury, M. (2017). Experimental investigation of the brittle-viscous transition in mafic rocks – Interplay between fracturing, reaction, and viscous deformation. *Journal of Structural Geology*, *105*, 62–79. https://doi.org/10.1016/j.jsg.2017.10.011

Minkley, W., Knauth, M., Fabig, T., & Farag, N. (2015). Stability and integrity of salt caverns under consideration of hydro-mechanical loading. *Proceedings of the Conference on the Mechanical Behavior of Salt VIII*, 217–228.

Munson, D. E., Ehgartner, B., Bauer, S., Rautman, C., & Myers, R. (2004). *Analysis of a salt fall in Big Hill Cavern 103, and a preliminary concept of salt dome structure*. Paper presented at Solution Mining Research Institute Spring Meeting, Wichita, KS.

Nikolinakou, M. A., Hudec, M. R., & Flemings, P. B. (2014). Comparison of evolutionary and static modeling of stresses around a salt diapir. *Marine and Petroleum Geology*, *57*, 537–545. https://doi.org/10.1016/j.marpetgeo.2014.07.002

Noda, H. & Takahashi, M. (2016). The effective stress law at a brittle-plastic transition with a halite gouge layer. *Geophysical Research Letters*, *43*(5), 1966–1972. https://doi.org/10.1002/2015GL067544

Nur, A. & Byerlee, J. (1971). An exact effective stress law for elastic deformation of rock with fluids. *Journal of Geophysical Research*, *76*(26), 6414–6419. https://doi.org/10.1029/JB076i026p06414

Paterson, M. S. & Wong, T. (2005). *Experimental rock deformation-the brittle field*.

Berlin, Germany: Springer-Verlag Berlin Heidelberg.

Peach, C. J. & Spiers, C. J. (1996). Influence of crystal plastic deformation on dilatancy and permeability development in synthetic salt rock. *Tectonophysics*, *256*(1–4), 101–128. https://doi.org/10.1016/0040-1951(95)00170-0

Pennock, G. M., Drury, M. R., Peach, C. J., & Spiers, C. J. (2006). The influence of water on deformation microstructures and textures in synthetic NaCl measured using EBSD. *Journal of Structural Geology*, *28*(4), 588–601. https://doi.org/10.1016/j.jsg.2006.01.014

Pennock, G. M., Zhang, X., Peach, C. J., & Spiers, C. J. (2007). Microstructural study of reconsolidated salt. *Proceedings of the Conference on the Mechanical Behavior of Salt VI – Understanding of THMC Processes in Salt*, 231–236.

Raj, R. & Ashby, M. F. (1971). On grain boundary sliding and diffusional creep. *Metallurgical Transactions*, *2*(4), 1113–1127. https://doi.org/10.1007/BF02664244

Reber, J. E., Lavier, L. L., & Hayman, N. W. (2015). Experimental demonstration of a semi-brittle origin for crustal strain transients. *Nature Geoscience*, *8*, 712. https://doi.org/10.1038/ngeo2496

Reber, J. E. & Pec, M. (2018). Comparison of brittle- and viscous creep in quartzites: Implications for semi-brittle flow of rocks. *Journal of Structural Geology*, *113*, 90–99. https://doi.org/10.1016/j.jsg.2018.05.022

Robertson, E. C., Robie, R. A., & Books, K. G. (1958). Physical properties of salt, anhydrite, and gypsum. In *Trace Elements Memorandum Report 1048*. Denver, CO: United States Department of the Interior Geological Survey.

Roedder, E. (1984). The fluids in salt. *American Mineralogist*, *69*(5–6), 413–439.

Rokahr, R., Staudtmeister, K., Zander-Schiebenhöfer, D., & Johansen, J. I. (2007). *In-situ test with a gas storage cavern as a basis for optimization*. Paper presented at Solution Mining Research Institute Spring Meeting, Basel, Switzerland.

Rutter, E. H., Atkinson, B. K., & Mainprice, D. H. (1978). On the use of the stress relaxation testing method in studies of the mechanical behaviour of geological materials. *Geophysical Journal of the Royal Astronomical Society*, *55*(1), 155–170. https://doi.org/10.1111/j.1365-246X.1978.tb04754.x

Salzer, K., Popp, T., & Böhnel, H. (2007). Mechanical and permeability properties of highly pre-compacted granular salt bricks. *Proceedings of the Conference on the Mechanical Behavior of Salt – Understanding of THMC Processes in Salt*, 239–248.

Schenk, O. & Urai, J. L. (2003). Microstructural evolution and grain boundary structure during static recrystallization in synthetic polycrystals of sodium chloride containing saturated brine. *Contributions to Mineralogy and Petrology*, *146*(6), 671–682. https://doi.org/10.1007/s00410-003-0522-6

Schenk, O., Urai, J. L., & Piazolo, S. (2006). Structure of grain boundaries in wet, synthetic polycrystalline, statically recrystallizing halite - Evidence from cryo-SEM observations. *Geofluids*, *6*(1), 93–104. https://doi.org/10.1111/j.1468-8123.2006.00134.x

Scholz, C. H. (2002). *The mechanics of earthquakes and faulting*. Cambridge, United Kingdom: Cambridge University Press.

Senseny, P. E., Hansen, F. D., Russell, J. E., Carter, N. L., & Handin, J. W. (1992). Mechanical behavior of rock salt - Phenomenology and micromechanisms. *International Journal of Rock Mechanics and Mining Sciences*, *29*(4), 363–378. https://doi.org/Doi 10.1016/0148-9062(92)90513-Y

Shimamoto, T. (1986). Transition between frictional slip and ductile flow for halite shear zones at room temperature. *Science*, *231*(4739), 711–714. https://doi.org/10.1126/science.231.4739.711

Sibson, R. H. (1977). Fault rocks and fault mechanisms. *Journal of the Geological Society*, *133*(3), 191–213. https://doi.org/10.1144/gsjgs.133.3.0191

Sibson, R. H. (1983). Continental fault structure and the shallow earthquake source. *Journal of the Geological Society*, *140*(5), 741–767. https://doi.org/10.1144/gsjgs.140.5.0741

Sibson, R. H. (1986). Earthquakes and rock deformation in crustal fault zones. *Annual Review of Earth and Planetary Sciences*, *14*, 149–175. https://doi.org/10.1146/annurev.ea.14.050186.001053

Skempton, A. W. (1960). Effective stress in soils, concrete and rocks. *Proceedings of the Conference on Pore Pressure and Suction in Soils*, 4–16. https://doi.org/10.1680/sposm.02050.0014

Sobolik, S. R. & Lord, A. S. (2015). Operation, maintenance, and monitoring of large-diameter caverns in oil storage facilities in domal salt. *Proceedings of the Conference on the Mechanical Behavior of Salt VIII*, 229–242.

Spiers, C. J. & Carter, N. L. (1996). Micorophysics of rocksalt flow in nature.

Proceedings of the Conference on the Mechanical Behavior of Salt IV, 115–128.

Spiers, C. J., Urai, J. L., Lister, G. S., Boland, J. N., & Zwart, H. J. (1986). The influence of fluid-rock interaction on the rheology of salt rock. In *Nuclear Science and Technology*. Luxembourg: Commission of the European Communities.

Strehlau, J. (1986). A discussion of the depth extent of rupture in large continental earthquakes. In Das, S., Boatwright, J., Scholz, C. H. (Eds.), *Earthquake Source Mechanics, Geophysical Monograph Series* (Vol. 37, pp. 131–146). Washington, DC: American Geophysical Union. https://doi.org/10.1029/GM037p0131

Ter Heege, J. H., De Bresser, J. H. P., & Spiers, C. J. (2005). Rheological behaviour of synthetic rocksalt: The interplay between water, dynamic recrystallization and deformation mechanisms. *Journal of Structural Geology*, *27*(6), 948–963. https://doi.org/10.1016/j.jsg.2005.04.008

Terzaghi, K. Van (1923). Die Berechnung der Durchlassigkeits-Ziffer des Tones aus dem Verlauf der hydrodynamischen Spannungserscheinungen. *Sitz. Akad. Wissen. Wien Math-naturw., Kl. Abt. I*, 125–138.

Thompson, W. K. (1965). Infra-red spectroscopic studies of aqueous systems. Part 1.—Molar extinction coefficients of water, deuterium oxide, deuterium hydrogen oxide, aqueous sodium chloride and carbon disulphide. *Transactions of the Faraday Society*, *61*, 2635–2640. https://doi.org/10.1039/TF9656102635

Tullis, J. A. (1979). High temperature deformation of rocks and minerals. *Reviews of Geophysics*, *17*(6), 1137–1154. https://doi.org/10.1029/RG017i006p01137

Urai, J. L., Means, W. D., & Lister, G. S. (1986). Dynamic recrystallization of minerals.

Mineral and rock deformation: Laboratory studies, Geophysical Monograph Series (Vol. 36, pp. 161–199). Washington, DC: American Geophysical Union. https://doi.org/10.1029/GM036p0161

Urai, J. L., Schléder, Z., Spiers, C. J., & Kukla, P. A. (2008). Flow and transport properties of salt rocks. In Littke, R., Gajewski, D., Nelskamp, S., Bayer, U. (Eds.), *Dynamics of complex intracontinental basins: The central European basin system* (pp. 277–290). Berlin, Germany: Springer-Verlag Berlin Heidelberg.

Urai, J. L., Spiers, C. J., Zwart, H. J., & Lister, G. S. (1986). Weakening of rock salt by water during long-term creep. *Nature*, *324*, 554–557. https://doi.org/10.1038/324554a0

Van den Kerkhof, A. M. & Hein, U. F. (2001). Fluid inclusion petrography. *Lithos*, *55*(1–4), 27–47. https://doi.org/10.1016/S0024-4937(00)00037-2

Watanabe, T. & Peach, C. J. (2002). Electrical impedance measurement of plastically deforming halite rocks at 125°C and 50 MPa. *Journal of Geophysical Research: Solid Earth*, *107*(B1), ECV 2-1-ECV 2-12. https://doi.org/10.1029/2001JB000204

Zener, C. (1941). Theory of the elasticity of polycrystals with viscous grain boundaries. *Physical Review*, *60*(12), 906. https://doi.org/10.1103/PhysRev.60.906

Zhang, X., Grupa, J., Spiers, C. J., & Peach, C. J. (2007). Stress relaxation experiments on compacted granular salt. *Proceedings of the Conference on the Mechanical Behavior of Salt VI – Understanding of THMC Processes in Salt*, 159–166.

Zhu, C. & Arson, C. (2015). A model of damage and healing coupling halite thermo-mechanical behavior to microstructure evolution. *Geotechnical and Geological*

Engineering, *33*(2), 389–410. https://doi.org/10.1007/s10706-014-9797-9

Zhu, C. & Arson, C. (2015). Fabric-based modeling of thermo-mechanical damage and healing around salt caverns. *Proceedings of the Conference on the Mechanical Behavior of Salt VIII*, 243–254.